

MASSIVE STAR CLUSTER FORMATION AND DESTRUCTION IN LUMINOUS INFRARED GALAXIES IN GOALS

S. T. LINDEN¹, A. S. EVANS^{1,2}, J. RICH³, K. LARSON³, L. ARMUS³, T. DÍAZ-SANTOS⁴, G. C. PRIVON⁵, J. HOWELL³, H. INAMI⁶, D.-C. KIM², L.-H. CHIEN⁷, T. VAVILKIN⁸, J. M. MAZZARELLA⁹, J. A. SURACE¹⁰, S. MANNING¹¹, A. ABDULLAH¹², A. BLAKE¹², A. YARBER¹², T. LAMBERT¹³

Draft version November 10, 2021

ABSTRACT

We present the results of a *Hubble Space Telescope* ACS/HRC FUV, ACS/WFC optical study into the cluster populations of a sample of 22 Luminous Infrared Galaxies in the Great Observatories All-Sky LIRG Survey. Through integrated broadband photometry we have derived ages and masses for a total of 484 star clusters contained within these systems. This allows us to examine the properties of star clusters found in the extreme environments of LIRGs relative to lower luminosity star-forming galaxies in the local Universe. We find that by adopting a Bruzual & Charlot simple stellar population (SSP) model and Salpeter initial mass function, the age distribution of clusters declines as $dN/d\tau = \tau^{-0.9+/-0.3}$, consistent with the age distribution derived for the Antennae Galaxies, and interpreted as evidence for rapid cluster disruption occurring in the strong tidal fields of merging galaxies. The large number of $10^6 M_{\odot}$ young clusters identified in the sample also suggests that LIRGs are capable of producing more high-mass clusters than what is observed to date in any lower luminosity star-forming galaxy in the local Universe. The observed cluster mass distribution of $dN/dM = M^{-1.95+/-0.11}$ is consistent with the canonical -2 power law used to describe the underlying initial cluster mass function (ICMF) for a wide range of galactic environments. We interpret this as evidence against mass-dependent cluster disruption, which would flatten the observed CMF relative to the underlying ICMF distribution.

Subject headings: galaxies: active - galaxies: individual (NGC 3256, NGC 3690, NGC 1614) - galaxies: interactions - infrared: galaxies

1. INTRODUCTION

Galaxies with high infrared (IR) luminosities, e.g., luminous infrared galaxies (LIRGs: $L_{\text{IR}}[8 - 1000\mu\text{m}] > 10^{11.0} L_{\odot}$), are rare in the local Universe, yet they are a cosmologically important class of objects because they dominate the infrared luminosity density at redshifts $z = 1 - 2$ (Magnelli et al. 2013). Their high bolometric luminosities emanate from energetic star-formation (SF) regions, and sometimes active galactic

nuclei (AGN), which are primarily triggered by interactions and mergers of gas-rich galaxies (e.g., Sanders & Mirabel, 1996). Further, the complex structure of these dynamically evolving systems and the presence of both dust-obscured and un-obscured activity necessitates the need for high-resolution observations that sample as much of the electromagnetic spectrum as possible to best identify and reconstruct the distribution and luminosity of star-formation and AGN-related phenomena, and to probe the connection between merger stage and the observed activity. Understandably, the ultraviolet (UV) properties of these very IR-luminous galaxies have received far less scrutiny. However, the small fraction of the UV radiation from super star clusters, AGN, and diffuse stellar emission that escapes can nonetheless make LIRGs powerful sources of UV radiation (e.g., Evans et al. 2008; Armus et al. 2009; Howell et al. 2010; Inami et al. 2010).

Of interest for the present study of LIRGs are the luminous star clusters (SCs), which track basic information regarding the formation and fate of star formation in a variety of different environments. The *Hubble Space Telescope* (HST) has been instrumental in the detection of numerous star clusters ($\gtrsim 1000$) in gas-rich mergers (e.g. NGC 3256: Zepf et al. 1999; NGC 4038/9: Whitmore & Schweizer 1995, Whitmore et al. 1999) and recent merger remnants (e.g. NGC 3921: Schweizer et al. 1996; NGC 7252: Miller et al. 1997, Schweizer & Seitzer 1998; NGC 3610: Whitmore et al. 1997). The presence of young ($\lesssim 10$ Myr) and intermediate age (100 - 500 Myr) star cluster populations in late stage mergers such

¹ Astronomy Department, University of Virginia, 530 McCormick Road, Charlottesville, VA 22904 USA: stl7ey@virginia.edu

² National Radio Astronomy Observatory, 520 Edgemont Road, Charlottesville, VA 22903 USA

³ Infrared Processing and Analysis Center, California Institute of Technology, MS 100-22, Pasadena, CA 91125 USA

⁴ Núcleo de Astronomía de la Facultad de Ingeniería, Universidad Diego Portales, Av. Ejército Libertador 441, Santiago, Chile

⁵ Instituto de Astrofísica, Facultad de Física, Pontificia Universidad Católica de Chile, Casilla 306, Santiago 22, Chile

⁶ Centre de Recherche Astrophysique de Lyon (CRAL), Observatoire de Lyon, 9 avenue Charles André, 69230 Saint-Genis-Laval France

⁷ Space Telescope Science Institute, 3700 San Martin Drive, Baltimore, MD 21218, USA

⁸ Department of Physics & Astronomy, Stony Brook University, Stony Brook, NY, 11794-3800 USA

⁹ Spitzer Science Center, Pasadena, CA 91125 USA

¹⁰ Eureka Scientific, Inc. 2452 Delmer Street Suite 100 Oakland, CA 94602-3017 USA

¹¹ Department of Astronomy, The University of Texas at Austin, 2515 Speedway Boulevard Stop C1400, Austin, TX 78712, USA

¹² Department of Physics and Astronomy, Howard university, 2355 6th St. NW, Washington, DC 20059

¹³ Department of Astronomy, University of Maryland, College Park, MD 20742

as the Antennae galaxies (NGC 4038/4039; Whitmore et al. 1999), Arp 220 (Wilson et al. 2006), the Mice galaxies (NGC 4676 A/B; Chien et al. 2007) is consistent with the description of these galaxies as experiencing powerful starbursts triggered by the interaction and merger of pairs of gas-rich galaxies. However, optical studies of other late stage mergers such as NGC 6240 (Pasquali, de Grijs & Gallagher 2003) and NGC 7673 (Homeier, Gallagher & Pasquali 2002) reveal only young star clusters, indicating that older star clusters, which would have formed earlier on in the merger, are either undetected or rare. In contrast, the lack of young star clusters in the tidal tails of NGC 520 and NGC 2623 (Mullia et al. 2015) relative to what is observed for NGC 3256 (Trancho et al. 2007) suggests that the remaining reservoirs of predominantly neutral hydrogen (HI) gas in the tails cannot always form new clusters.

Many studies have been devoted to understanding the long-term stability of the youngest clusters in mergers (e.g. Fall et al. 2009; Whitmore et al. 2007). It appears that only those which survive the disruption processes and are still dense and gravitationally bound are likely to become the globular clusters (GCs) we observe today (Zhang & Fall 1999). The relative contributions from various cluster disruption mechanisms such as infant mortality (Fall et al. 2005; Chandar et al. 2010a), two-body relaxation (Fall et al. 2009), and tidal shocks (Gnedin & Ostriker 1997) as a function of galactic environment continues to be the subject of much work. Infant mortality or rapid disruption, is caused by mass-loss during the early gas expulsion phase of cluster evolution and is expected to work on timescales of ≤ 10 Myr. In contrast, disruption from large scale shocks is expected to be important over roughly 10^8 yr timescales, and two body relaxation will cause disruption on even longer timescales (on the order of a Hubble time). Ultimately, the manner in which these young massive clusters (YMCs) evolve is crucial to connecting them to present day globular clusters. If YMCs are indeed local analogues to present-day GCs, then by understanding their formation and evolution, it is possible to gain insight into the formation of the earliest most massive clusters in the Universe (Kruijssen 2014).

In addition to understanding the fate of clusters, it is important to understand to what degree their environment affects where and how they form, as well as what their collective properties are – e.g., the distribution of massive clusters (Initial Cluster Mass Function: ICMF) and the efficiency with which bound star clusters form (Larsen & Richtler 2000; Bastian 2008). Although the low mass end of the ICMF appears to be universal (de Grijs et al. 2003; Fall & Chandar 2012), the formation conditions of the highest-mass clusters are still subject to debate.

One idea is that the formation mechanism of the most massive clusters is independent of environment (Whitmore et al. 2007; Chandar et al. 2015), and thus the total number and maximum cluster mass scale linearly with the star formation rate of the galaxy (Hunter et al. 2003; Whitmore et al. 2010; Vavilkin et al. 2016). Alternatively, the formation of the most massive clusters may require special physical conditions, such as high ambient pressure or enhanced gas densities. Kruijssen et al. (2012) predicts that the formation of bound stellar clus-

ters takes place in the highest-density peaks of the ISM. Therefore, YMCs should form more efficiently at high gas pressures (and hence gas surface densities), because these conditions lead to higher density peaks. This leads to a non-linear scaling of the maximum cluster observed and the star formation rate surface density (Σ_{SFR}) of the galaxy.

To really quantify the role of galactic environment in shaping massive cluster formation and destruction, we need to study the properties of star clusters in a statistically larger sample of Luminous Infrared Galaxies which represent the most extreme star-forming systems observed in the local Universe. The Great Observatories All-Sky LIRG Survey (GOALS), is a multi-wavelength imaging and spectroscopic study of a complete flux density-limited ($S_{60\mu\text{m}} > 5.24$ Jy) sample of the 202 LIRGs in the *IRAS* Revised Bright Galaxy Sample (RBGS; Sanders et al. 2003, GOALS; Armus et al. 2009). The proximity, size, and completeness of the sample, combined with broad wavelength coverage, makes GOALS the definitive sample for studying star clusters in local, luminous star forming galaxies. The present study makes use of HST UV and optical images from GOALS to estimate the cluster age distribution, the cluster mass function, and the cluster formation efficiency in a sample of 22 LIRGs.

The paper is organized as follows: In §2, the sample selection is summarized. In §3, the observations and data reduction are described, as well as our method for identifying clusters. In §4, the manner in which the cluster ages are estimated is described. In §5, the age distribution, the mass function and the cluster efficiency are discussed within the context of lower luminosity star-forming galaxies. Section 6 is a summary of the results.

Throughout this paper, we adopt a WMAP Cosmology of $H_0 = 70$ km s $^{-1}$ Mpc $^{-1}$, $\Omega_{\text{matter}} = 0.28$, and $\Omega_{\Lambda} = 0.72$ (e.g., see Armus et al. 2009).

2. SAMPLE SELECTION

Within GOALS, there are HST B- and I-band observations of all 88 LIRGs with $L_{\text{IR}} \geq 10^{11.4} L_{\odot}$. Of those, we select the 22 LIRGs observed to have greater than 100 B-band luminous clusters ($m_{\text{B}} \sim 21 - 23$ mag) within the central $30 \times 30''$ of the galaxy (i.e, a limit imposed by our far-UV imaging field of view – see below). In total we observed 9131 B-band luminous star clusters from galaxies in the sample.

3. OBSERVATIONS, DATA REDUCTION, AND CLUSTER SELECTION

The HST B- (F435W) and I- (F814W) band images were obtained with the Wide Field Camera (WFC) on the Advanced Camera for Surveys (ACS) during the period 2005 August to 2007 January (PI: A. Evans; PID 10592). In all but a few cases, the wide field-of-view of the WFC ($202'' \times 202''$) enabled the full extent of each LIRG to be observed. Each galaxy was observed in both filters per orbit, with two and three dithered exposures in ACCUM mode in the F814W filter and F435W filters, respectively. The approximate integration times for each filter were 21 minutes in F435W and 12 minutes in F814W. The ACS data were reduced with the Multidrizzle software included in *IRAF/STSDAS* provided by STScI, to identify and reject cosmic rays and bad

TABLE 1
 PROPERTIES OF THE 27 GOALS GALAXIES IN THE SAMPLE

Name	RA	Dec	Log(LIR)	D(Mpc)	SFR ^a	IR/UV ^a	f_{ν} (FUV) ^a	MS ^b	A_v ^c
NGC 0017	00:11:06.5000	-12:06:26.00	11.49	83	55.25	31.2	1.53e-14	5	3.0
Arp 256S	00:18:50.9000	-10:22:37.00	11.45	110	48.63	7.6	1.42e-14	3	1.7
Arp 256N	00:18:50.0430	-10:21:43.62	10.36	110	3.95	7.6	1.24e-14	3	1.7
NGC 0695	01:51:14.2000	+22:34:57.00	11.68	130	84.64	37.1	2.50e-16	0	2.8
UGC 02369	02:54:01.8000	+14:58:25.00	11.60	132	50.11	39.81	-	2	2.3
NGC 1614	04:33:59.8000	-08:34:44.00	11.60	67	51.28	15.13	-	5	4.0
2MASX J06094582-2140234	06:09:45.8000	-21:40:24.00	11.60	165	-	-	-	3	1.0
2MASX J08370182-4954302	08:37:01.8000	-49:54:30.00	11.60	115	-	-	-	3	3.7
NGC 2623	08:38:24.1000	+25:45:17.00	11.60	84	69.19	95.6	5.44e-15	5	1.5
UGC 04881	09:15:55.1000	+44:19:55.00	11.74	178	97.13	52.3	2.52e-15	2	1.9
IC 2545	10:06:04.5810	-33:53:05.55	11.70	150	-	-	-	4	4.0
NGC 3256	10:27:51.3000	-43:54:14.00	11.64	38	76.46	71.6	3.10e-14	5	3.7
Arp 148	11:03:53.2000	+40:50:57.00	11.60	160	-	-	-	2	2.1
NGC 3690E	11:28:33.4470	+58:33:46.08	11.41	45.2	45.19	29.4	3.59e-14	3	3.4
NGC 3690W	11:28:30.3390	+58:33:39.48	11.77	45.2	101.44	29.4	8.32e-14	3	3.9
NGC 5257E	13:39:57.6830	+00:49:49.80	11.32	99	36.06	9.1	2.84e-14	2	2.6
NGC 5257W	13:39:52.9530	+00:50:23.10	11.31	99	35.66	9.1	1.10e-14	2	1.8
NGC 5331S	13:52:16.2140	+02:06:03.28	11.54	139	60.78	32.7	1.32e-15	3	3.6
NGC 5331N	13:52:16.3810	+02:06:29.88	11.02	139	18.10	32.7	3.89e-15	3	1.8
UGC 09618NED02	14:57:00.8000	+24:37:04.00	11.70	150	65.56	10.47	-	1	2.4
IC 4687N	18:13:39.7490	-57:43:29.20	11.32	77	38.51	35.3	4.11e-15	2	2.8
IC 4687S	18:13:40.4750	-57:44:53.95	11.02	77	15.49	35.3	1.92e-15	2	3.7
NGC 6786	19:10:53.9000	+73:24:37.00	11.40	101	-	-	-	2	1.0
IRAS 20351+2521	20:37:17.8000	+25:31:38.00	11.50	15	-	-	-	1	9.4
II ZW 096	20:57:23.3000	+17:07:34.00	11.94	150	156.77	23.9	1.64e-14	2	3.0
ESO 148-IG002	23:15:46.8000	-59:03:16.00	12.06	190	204.60	48.8	5.88e-15	4	2.5
NGC 7674	23:27:56.7000	+08:46:45.00	11.56	120	61.26	16.4	1.42e-14	2	2.0

^a SFRs calculated using IR+UV data taken from Howell et al. 2010 and U et al. (2012)

^b Merger Stages taken from Haan et al. (2013) and Stierwalt et al. (2013)

^c The maximum A_v adopted for each galaxy taken from the literature. See Appendix for more details.

pixels, remove geometric distortion, and to combine the images into mosaics. Because of the limited number of dithers, additional cosmic rays rejection routines were run on each image prior to drizzling (see Kim et al. 2013 for a detailed description).

The HST far-UV (F140LP) and optical images in the sample were obtained with the Solar Blind Channel (SBC) on the Advanced Camera for Surveys (ACS) during the period 2008 April – 2009 August (PID 11196; PI: A. Evans). The field of view of the SBC is $\sim 30'' \times 30''$ – this placed a limit on the area within each LIRG over which the clusters could be analyzed. The data were taken in the ACCUM mode using the PARALLELOGRAM four-position dither pattern for a total integration time per galaxy of 40–45 minutes. We further reduced the SBC data with the Multidrizzle software included in *IRAF/STSDAS* provided by STScI, to identify and reject cosmic rays and bad pixels, remove geometric distortion, and to combine the images into mosaics.

Before an automated routine for cluster identification could be applied to the images, contamination from foreground stars and distant background galaxies outside of the area of each image subtended by the LIRG (i.e., the “sky” area) had to be minimized. Masks of each image were made by first creating a median-smoothed version of the F435W and F814W images. The effect of this filtering is to minimize structures in the sky region with spatial extents significantly smaller than the filter size (i.e., faint stars and distant background galaxies). The backgrounds, containing low pixel values, were then set to zero, while the high pixels corresponding to the LIRG were set to one. Finally, pixels associated with any bright stars in the image were set to zero. The original reduced

image was then multiplied by the final mask of the galaxy to set the regions outside of the galaxy equal to zero.

Star clusters in all three bands were selected using the program SExtractor (Bertin & Arnouts 1996). The identification of clusters and the extraction of photometry is complicated by the non-uniform surface brightness of the underlying galaxy. To estimate and subtract the underlying galaxy, Source Extractor iteratively computes the median and standard deviation of the pixels within a mesh of $n \times n$ pixels. During each iteration, outlier pixels are discarded until all of the pixels within each mesh are within 3σ of the median value. Several mesh sizes were tested, and for each mesh the photometry of several of the clusters was separately computed via the IPAC image display and analysis program Skyview and compared to values estimated from the original image (Skyview allows users to manually size and place apertures on clusters, and it allows for local background around the aperture to be subtracted). The mesh sizes varied between 9 and 14 pixels, and overall did an efficient job of removing the underlying galaxy and minimizing the creation of negative value holes surrounding clusters created through over-subtraction of the local background. Cluster photometry across all background-subtracted images was then calculated using the IDL package APER (originally modified from DAOPHOT). We used an aperture of radius 6.0 pixels for the HRC images and 3.0 pixels for the WFC images (= 0.15'' in both cases). An annulus with radius 4 pixels and a thickness of 5 pixels was used to measure the local background in the WFC images; the radii and thickness of the annulus was adjusted accordingly for the SBC images. Aperture corrections were calculated based on the flux calibrations of unresolved sources by Sirianni et al. (2005). We corrected the photometry

for foreground Galactic extinction, using the Schlafly & Finkbeiner (2011) dust model combined with the empirical reddening law of Fitzpatrick et al. (1999) available through the NASA Extragalactic Database (NED).

In the process of doing the photometry, we filtered out all sources which had a signal-to-noise ratio, $S/N < 5$ and which were not visible in all three filters. This left us with a total of 1186 cluster candidates identified in the sample. We then used ISHAPE (Larsen 1999) to measure the FWHM values for all remaining sources in all three wavelengths; this was done in order to separate stars and background galaxies from clusters. ISHAPE measures FWHMs by de-convolving the HST instrumental point spread function with a King profile, then performing a χ^2 calculation to test the goodness of fit to each individual cluster (King 1966). ISHAPE iterates through different values for the effective radius until a minimum χ^2 is found. Similiar to the approach in Mulia et al. (2015), we find that a conservative cut of 2 pixels FWHM effectively removes extended sources in both the nearest and furthest galaxies in the sample. Additionally, we made a cut of $M_B \leq -9.5$ mag, corresponding to the Humphreys & Davidson (1979) limit, where we might expect contamination of the cluster sample from single bright yellow supergiants in the Milky Way. This was shown in Whitmore et al. 2010 to be an effective way to remove foreground stars by their luminosity alone. A total of 665 clusters across all 22 LIRGs (27 nuclei) meet the above criteria.

One remaining concern with this approach was that at the average distance of the galaxies in our sample (115 Mpc), our size estimates would not correspond to physically relevant values for individual clusters. Indeed a 2 pixel FWHM at the resolution of WFC gives an average cluster size of $R_{eff} \sim 24$ pc. For the most nearby galaxies in the sample, we derive consistent results with the established cluster size in the Antennae of $R_{eff} \sim 5 - 10$ pc (Anders et al. 2007). However, for the most distant galaxies in the sample our size estimates are nearly three times larger (~ 37 pc), which is an effect we must take into consideration when interpreting our results (see §5). Importantly, the measured cluster sizes are all still well below the average size of an entire cluster complex or OB association ($R_{eff} \sim 100 - 200$ pc: Bastian et al. 2006), where the application of simple stellar population (SSP) models would be questionable.

4. AGE-DATING CLUSTERS

4.1. Model Fitting

For each cluster in each galaxy, the measured colors were compared with the evolutionary tracks from GALAXEV (version 2003), a library of evolutionary stellar population synthesis models that were computed using the isochrone synthesis code of Bruzual & Charlot (2003), hereafter referred to as BC03. This code computes the spectral evolution of a stellar population based on a stellar evolution prescription (Padova 1994) and a library of observed stellar spectra. The output of the model SED was multiplied by the ACS F435W, F814W, and SBC 140LP filter response functions in order to obtain magnitudes and colors in these filters. We first estimate the age and the extinction A_V by performing a χ^2 fit assuming an instantaneous burst simple stellar popu-

lation (SSP), a Salpeter IMF (Salpeter 1955), and both solar and sub-solar metallicities as suggested for LIRGs by Kewley et al. (2010). We also apply a Calzetti extinction law of the form $k(\lambda) = A(\lambda)/E(B - V)_* = a + b/\lambda + c/\lambda^2 + d/\lambda^3$, where a, b, c, and d are constants in a given wavelength range, and $A(\lambda)$ is the attenuation in magnitudes. The total attenuation of the stellar continuum, $R_V = A(V)/E(B - V)_* = 4.05 \pm 0.8$, is calibrated specifically for starburst galaxies and differs from the typical Milky Way value of $R_V \sim 3.1$ (Calzetti et al. 2000). It has been shown empirically that clusters and HII regions are more heavily attenuated than the underlying stellar continuum, due to the fact that these objects are often found near dusty regions of ongoing star formation (Calzetti 1994). From galaxy to galaxy, there can be considerable variations in the detailed dust distributions, but Calzetti et al. (2000) points out that in all the cases they studied, the empirical law recovers the total dust optical depth of UV-bright starburst galaxies within a factor of two.

It is worth noting here that a major concern in estimating cluster ages is the effect of stochasticity which affects clusters with low masses. Such clusters have too low a mass to adequately produce a sufficient number of stars in all mass ranges, and thus any age-dating prescription making use of a standard IMF fails to predict the correct cluster age. Given the distance of the LIRGs in the sample and thus the brightness of clusters detected by our HST observations, the detected clusters are unlikely to have low masses. Indeed, stochastic fluctuations are relatively minor for clusters with masses greater than $10^4 M_\odot$ (Fouesneau et al. 2012), which in our case is the lower limit of clusters we can observe.

Another factor affecting the age estimates is the metallicity. LIRGs are known to have gas-phase metallicities within 0.2 dex of solar in $12 + \log [O/H]$ (Relano et al. 2007; Rupke et al. 2012). Thus we consider both a solar ($z = 0.02$) and sub-solar ($z = 0.008$) BC03 model for each galaxy. Rich et al. 2012 also finds that the metallicity gradients in LIRGs are flattened by the merging process, allowing us to parameterize the metallicity of clusters with a single value for each galaxy.

The mass of each cluster is estimated from the observed B-band extinction-corrected luminosity and the mass-to-light ratios ($M(M_\odot) = L_B \times (M/L)$) predicted by the un-extincted model at the fitted age. The models assume that the stellar IMF for each cluster is fully sampled. The largest contribution to the uncertainty in the mass estimates are the uncertainties in the estimated ages, which are typically on the order of 0.3 dex in $\log(\tau)$. These translate to similar uncertainties of 0.3 and 2 in $\log(M)$ and M , respectively. The derived masses of the clusters depend on the IMF assumed in the stellar population models. For example, if a Chabrier IMF is adopted, the estimated mass of each cluster would decrease by a near constant 40 percent (although the shape of the mass function would not change). The average fractional uncertainty in the distances of each galaxy taken from NED are $\sim 7\%$. This would introduce uncertainties in the cluster mass estimates of roughly 13%, which is less than the error contribution from our cluster age fitting procedure.

The age and mass estimations using color-color diagrams together with evolutionary tracks suffer from age-

reddening degeneracy. As pointed out in Maoz et al. (2001), the use of a UV filter when examining the colors of star clusters does help to avoid the issue of “back-tracking,” whereby the reddening shifts the models in a direction nearly parallel to the aging direction. However, a cluster that appears red in the FUV-B, B-I color space can still be either very old, or young and heavily obscured by dust. In particular, young star clusters are assumed to be embedded in dust that is present in the star-forming region. Despite the fact that a fraction of the dust can be cleared away from young star-forming regions in as little as a few Myr (Larsen 2010), $0.5 \leq A_V \leq 2.5$ mag extinction has been reported for 4 Myr old clusters in nearby, lower luminosity galaxies (Whitmore & Zhang, 2002; Reines et al. 2008). Since our analysis involves the use of three filters, we cannot break this degeneracy with our photometry alone. Thus, the ages of clusters in our LIRG sample are solved for by creating a suite of SSPs within the FUV-B, B-I color space, incrementing by 0.1 in A_V as input to the extinction law, then solving for the age–reddening of each cluster based on the best χ^2 fit to an individual model within the suite. Further, it is important to note that because FUV light can accurately trace the ages of star clusters over two orders of magnitude (Meurer et al. 1995) our analysis of cluster ages is not biased by the requirement to detect a cluster in the F140LP SBC filter.

In order to better refine the age–reddening estimates for each cluster, two additional constraints were applied: First, we required that the extinction of any given cluster could not exceed estimates for the A_V of its host galaxy taken from the literature. Considering the fact that our F140LP cluster detections often span the entire SBC field-of-view, the average galaxy A_V is a good proxy for the amount of reddening one would expect each cluster could have before we are unable to detect it. It is important to note that only 5% of clusters in the final sample have extinctions which are equal to the maximum allowed for their host galaxy based on our fits, meaning that our choice of A_V is not systematically biasing our final derived values. This constraint additionally prevents our model from obtaining cluster properties with arbitrarily high extinctions and therefore cluster masses, which exceed what is possible for bound stellar clusters so far observed in extragalactic systems (Maraston et al. 2004). Second, we constructed B-I color images in order get a visual clue of where the projected dust lanes are in each galaxy. The reasoning is that by making a manual assessment of each image we can distinguish globular clusters, which have much redder colors and are often found in uncrowded regions away from sites of recent star formation (e.g., see Whitmore et al. 2014). One complicating factor is that a YMC that forms behind a projected dust lane can appear to have a color similar to these old GCs. By overlaying the cluster centroids, we identified which clusters had no obvious dust lanes in a surrounding annulus of 4 – 9 pixels. These clusters are therefore more likely to be young and extincted as opposed to relatively old and dust-free clusters. The results can be seen in the false-color images shown in the appendix. In total, only 10% of the clusters modeled had ages which differ by 0.6 dex (roughly twice the expected uncertainty) when including or excluding the additional dust-lane constraints. Whitmore et al. (2014) used this

additional constraint when looking at the cluster populations of 20 star-forming galaxies in the Local Universe, and found it to be effective regardless of the detailed galaxy morphologies seen in the color images.

We consider here how these constraints can be understood based on the $F435W - F814W$ value of each cluster: Clusters designated with $(F435W - F814W) < 0.51$ mag can be reliably age-dated as being younger than 7 Myr, because the old-age track of the model never reach that part of the parameter space. Clusters with $(F435W - F814W) = 0.51 - 1.0$ mag have a wide range of possible ages (7 – 500 Myr), but if the cluster resides in a dustier region of the galaxy, then it is either an unreddened to moderately reddened old cluster or a young, heavily reddened cluster. This color bin covers the widest range of cluster ages and therefore contains the largest number of SCs. Finally, any SCs with $(F435W - F814W) = 1.0 - 1.5$ mag that do not reside in a more heavily extincted region of the galaxy are old, with ages between 500 Myr and 1 Gyr. The ages of clusters in these last two regions that lie in and around dust lanes are the ones most affected by our above criteria for solving the age–reddening degeneracy. Clusters with $(F435W - F814W) > 1.5$ have ages older than 1 Gyr assuming reasonable values for the internal extinction within the galaxy.

By examining the distributions of internal visual extinction and age for each cluster derived from the model, we see that nearly 1/3 of all young clusters in the sample have a relatively small dust correction ($A_V \leq 1$), and nearly 80% of all young clusters have an $A_V \leq 2$ correction. Thus the majority of all clusters in the sample need only a relatively modest dust correction, compared to a galaxies global average, to properly derive young ages.

4.2. Consistency Checks

4.2.1. Comparison with Direct SED-Fitting

In order to account for the effect our chosen filter set has on the derived cluster properties as described above, we compare the results of anchoring each color to the F435W measurement, with the results from fitting the three broadband photometric measurements (F140LP, F435W, and F814W) simultaneously, as was similarly done in Maoz et al. (2001), and shown to be an effective way to further improve our ability to separate the effects of age and extinction. To perform this full “SED-based” fitting we use the same galaxy evolution code, extinction model (minus the additional dust-lane constraints in both cases), IMF, and metallicity. From our sample of 665 clusters, we further remove from the final analysis any clusters for which the method described in Section 4.1 and this SED fitting method do not produce ages which agree within 0.6 dex of each other. These clusters are almost always ones for which their is nearly equal probability of the cluster being young and highly-extincted or old and less heavily extincted. These highly degenerate cases are therefore removed due to their uncertain contribution to the overall shape of the age and mass distributions to be derived. This leaves us with a final sample of 484 ($\sim 83\%$ of verified clusters) clusters that have age and mass estimates independent of the fitting method chosen for deriving cluster properties. We also note that of the original 67 clusters which provide

inconsistent age results in our own dust-lane vs. no-dust-lane analysis, 48 ($\sim 83\%$) are kept when comparing to the results of the full SED-fit. This again shows that our additional dust-lane constraints did not systematically bias the estimation of cluster ages.

4.2.2. Comparisons with Spectroscopic-Derived Ages

Chien (2010) measure Balmer line-derived cluster ages for a sample of GOALS LIRGs. Three of the systems in their sample overlap with our present study (NGC 2623, Arp 256, and Arp 299). Figure 1 is a comparison of our photometrically derived ages and the Balmer line-derived ages. Approximately 77% (17 of 22) of the clusters have ages that agree to within ± 0.3 dex, and 91% (20 of 22) have ages that agree to within ± 0.6 dex. This means that the majority of our 3-band cluster ages agree with the spectroscopic ages within the uncertainty of the BC03 models. Further, it is important to note that we derive young ages for all seven of the star clusters in our sample with identified Wolf-Rayet spectral features from Chien (2010). Wolf-Rayet features are very sensitive probes of young cluster ages since they only exist for clusters with ages of 3 – 7 Myr (Leitherer et al. 1999; Chien 2010).

It is potentially not surprising that the older clusters in the sample have more uncertain spectroscopic age measurements. In particular, as a cluster ages, the strength of the Balmer lines is significantly decreased (Gonzalez Delgado et al. 2005). Finally, the most discrepant age estimates come from NGC 2623. This could be due to the fact that the galaxy has a complicated morphology (Evans et al. 2008). All the young clusters identified come from a single “pie-wedge” structure to the right of the nucleus (see Appendix), while all the older clusters come from the nuclear regions. This makes using a simple prescription for an A_V correction over the entire FOV more uncertain.

4.2.3. Comparisons with Paschen- β Equivalent Widths Derived from WFC3 Imaging

Larson et al. (in prep) obtained Paschen- α and Paschen- β imaging for a subset of the GOALS sample, with 6 LIRGs (9 galaxies) overlapping our present HST sample. For any B-band cluster centroid that is spatially coincident with a high density clump in the Pa β images we can directly compare our cluster ages to ages derived via the equivalent width (in Angstroms) of the Pa β emission line. For an instantaneous burst SSP and a Salpeter IMF, the presence of Pa β emission constrains the burst age to less than 20 Myr because stars with masses greater than $10 M_{\odot}$ are required for significant production of ionizing photons. We utilize Starburst99 models of Pa β equivalent width as a function of clump age to independently derive ages for 27 clusters in the sample (Leitherer et al. 1999).

From Figure 2 we find that approximately 78% (21 of 27) of the clusters have ages that agree to within ± 0.3 dex, and 96% (26 of 27) have ages that agree to within ± 0.6 dex. This shows us that the majority of all clusters we identify as having bright Pa β counterparts are indeed young. Additionally, 89% of the clusters (= 24 out of 27) which are photometrically identified as having ages less than 20 Myrs have a mean Pa β equivalent width of $\log(W(Pa\beta)[\text{\AA}]) \sim 1.7$ or $\log(\text{Age}_{SB99}(\text{yr})) \sim 6.8$. It is

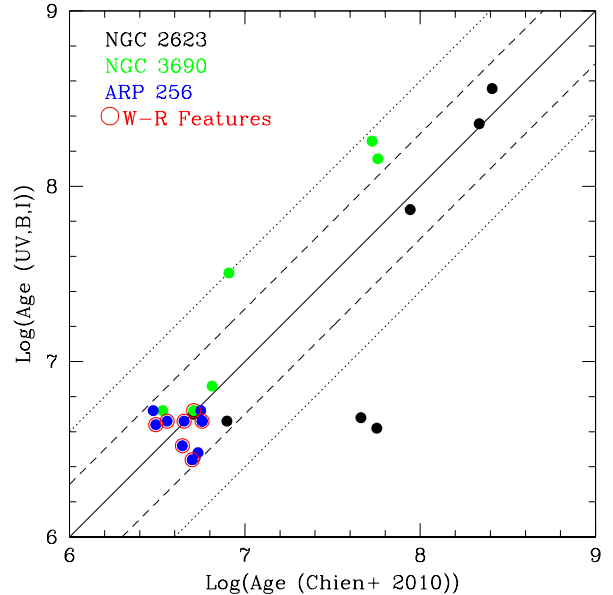


FIG. 1.— A comparison between the spectroscopically derived ages from Chien 2010 to our UV, B, I broadband age estimates for NGC 2623, NGC 3690E/W, and ARP 256N/S. The red circles denote star clusters which have Wolf-Rayet spectral features as identified in Chien (2010). The solid line represents the 1 : 1 correlation, whereas the dashed and dotted lines are within 0.3 and 0.6 dex of the 1 : 1 correlation.

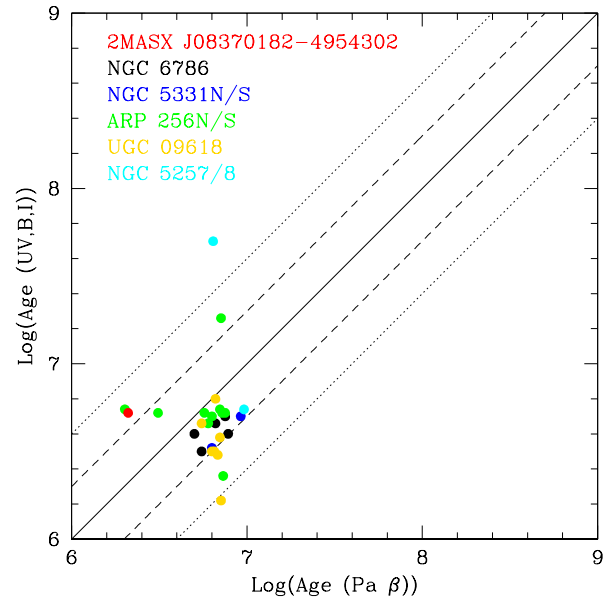


FIG. 2.— The 1 : 1 comparison of cluster ages derived using our UV, B, and I photometry and the equivalent width of the Pa β emission line associated with the cluster centroid from Larson et al. (in prep). The solid line represents the 1 : 1 correlation, whereas the dashed and dotted lines are within 0.3 and 0.6 dex of the 1 : 1 correlation.

important to note that of the 142 young ($t \leq 10^7$ yr) star clusters photometrically identified in these 6 LIRGs, we only associated a strong Pa β clump in the continuum-subtracted image with 19% (27 of 142) of them. This fraction is likely low for two reasons: (1) Our clusters are located primarily in the central regions of the galaxies, where the continuum subtraction is much more uncertain

due to the larger contribution of diffuse large-scale NIR emission. As a result, the minimum equivalent width of a marginal 3σ Pa β detection can vary by a factor of a few within a galaxy and by almost an order of magnitude on a galaxy-by-galaxy basis. This variation corresponds to ~ 0.3 dex change in the maximum derivable age using the SB99 model, which if we assume a 1 : 1 correlation, changes the age of the oldest cluster for which we would expect a counterpart in FUV emission by the same amount. (2) The resolution of the NIR Pa β images is $0.12''/\text{pixel}$, which is a factor of two lower than what we achieve in the FUV and optical imaging. This makes detecting bright compact sources of Pa β line emission embedded in a larger diffuse GMC cloud difficult at the distance of the galaxies in our sample.

Ultimately, both the local background subtraction and resolution contribute to the lack of overlap we observe in the Pa β and FUV emission. Regardless, this is an independent verification of our ability to derive accurate young ages for clusters in the sample, and shows us that our A_V corrections can do a reasonable job at photometrically separating young and old clusters.

4.3. Mass-Age Diagram and Completeness

Figure 3 shows the derived age and corresponding mass of each cluster identified in the sample. An immediate observation one can make is the lack of low-mass, old clusters. This is due to the fact that clusters dim as they age and eventually become fainter than our UV detection limits. We also note the large number of clusters seen with ages below 10 Myr over the full range of masses.

Although the cluster fitting method can create some observed structure in the mass-age diagram, it is unlikely to do so over all masses at young ages. In particular the lack of clusters with ages of $\sim 10^7$ Myr is a common feature of model-derived mass-age diagrams of star clusters in galaxies (Gieles et al. 2005, Goddard et al. 2010). This is due to the limited age resolution and overall degeneracy of the UV-B, B-I color track at these ages (See color-color diagrams in the Appendix). From the histograms in Figure 3, we conclude that there is a genuine over-density of clusters with ages below 10 Myr compared to above 10 Myr.

In order to determine the completeness limit of the cluster sample, we used a similar prescription to Whitmore et al. (1999), and set the limit for each galaxy as the magnitude at which 50% of the clusters are detected at B and I, but are missed at FUV. The magnitude distributions for each band are corrected for foreground galactic extinction, and spatially matched to the FOV of the SBC. Of the 22 LIRGs in the sample, 19 have magnitude distributions which span the full range of observed cluster values ($M_B = -10 \sim -15$ mag), and have a mean completeness of $M_B \sim -11.2$ mag. The three remaining sources have completeness limits which are shifted to higher magnitudes $M_B \sim -13$ mag, likely due to the fact that they are all further away than the mean distance of the galaxies in the sample (115 Mpc). It is important to note however, that there are several other galaxies for which a larger distance did not result in a shifted magnitude distribution, meaning that the actual 50% limit for the sample is not a strong function of the mean distance to any galaxy. Additionally, these outliers represent only 7% of the total cluster population. Therefore, to min-

imize their contributions to the final adopted limit for the entire sample, we calculated a cluster-weighted mean completeness limit, and found that the mean shifted only slightly to $M_B = -11.26$.

By applying this completeness limit to the BC03 model, we can define regions of this parameter space (both as a function of cluster ages over a mass range and masses over an age range) where we are observationally complete and thus working with a mass-limited sample of clusters. Mass-limited cluster samples have the advantage over luminosity-limited samples because they recover the underlying shape of the age distribution, and are thus not affected by the distance to each galaxy. However, the total number of clusters can be highly uncertain simply because the lower mass clusters are not included. We will discuss the implications for this fact in §5.

The four cuts were selected to sample distinct regions of the mass and age distribution for which we could maintain completeness. We define Region 1 to be:

$$6 < \log(M/M_\odot) < 8 \quad (1)$$

$$6.5 < \log(\tau) < 8.7 \quad (2)$$

Region 2 to be:

$$5.3 < \log(M/M_\odot) < 6 \quad (3)$$

$$6.6 < \log(\tau) < 8 \quad (4)$$

Region 3 to be:

$$\log(\tau) < 7 \quad (5)$$

$$5.3 < \log(M/M_\odot) < 8 \quad (6)$$

and Region 4 to be:

$$7.5 < \log(\tau) < 8.7 \quad (7)$$

$$6 < \log(M/M_\odot) < 8 \quad (8)$$

The two mass cuts are marked as Regions 1 and 2 in the left panel of Figure 3. Since older clusters are intrinsically fainter, a higher mass limit will result in a cluster population that is mass-limited to a wider range of ages. Note that the chosen mass-regimes do not contain the youngest least massive clusters that are only observed in a subset of our galaxies, and thus would bias any estimate for the global mass and age distributions of all the galaxies combined. Region 2 is chosen to match the age and mass limits from Fall et al. (2005), allowing us to make accurate comparisons to the cluster population of the most well-studied nearby major merger, the Antennae Galaxy. Regions 3 and 4 are chosen to sample the young (≤ 10 Myr) and old ($\tau \geq 10^{7.5}$) clusters respectively within the completeness limit. When analyzing Regions 1, 3, and 4 we will exclude the largest mass bin of $\log(M/M_\odot) = 8.0$. These very high masses are most likely the result of either an imperfect extinction correction or multiple star clusters in close proximity appearing as a single star cluster at the resolution of these images, resulting in a large derived total mass (See §5.2). While clusters of these masses have rarely been observed in abundance, we note that Bastian et al. (2013c) studied several young star clusters in NGC 7252 with masses

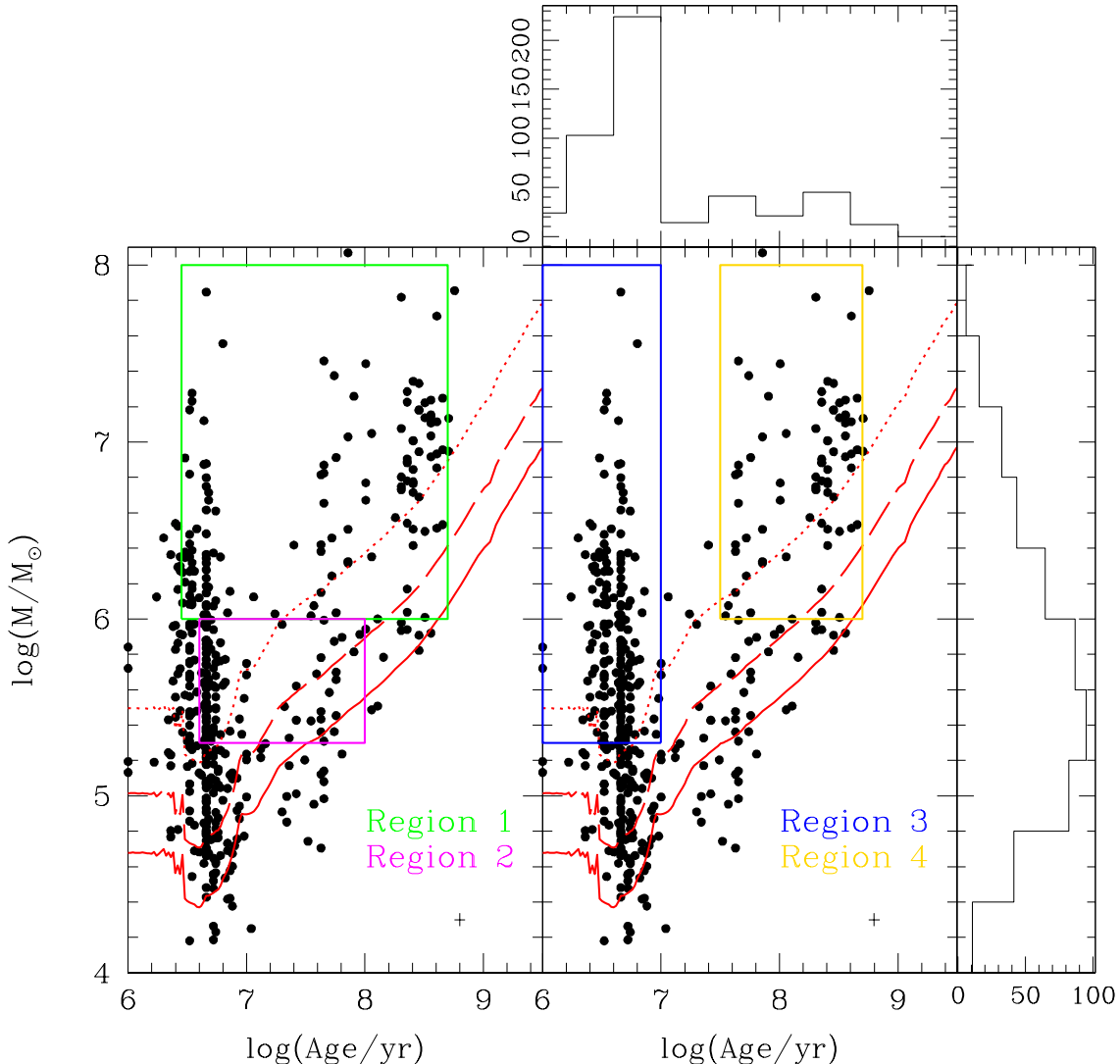


FIG. 3.— The mass, age distribution of all 484 clusters found in the 27 galaxies. The solid, dashed, and dotted red curves represent mass-age tracks produced from the BC03 model with an input of $M_B = -11.26$, $M_B = -12.07$, $M_B = -13.31$ for the 50%, 75%, and 100% completeness limits respectively. The green and purple boxes in the left panel represent Regions 1 and 2 respectively, and are used for the two mass-age cuts applied when analyzing the cluster age distribution. The blue and gold boxes in the middle panel represent Regions 3 and 4 respectively, and are used for the two mass-age cuts applied when analyzing the cluster mass distribution. The histograms show the distribution of cluster ages and masses for the full sample. The cross on the bottom right of each panel represents the median errors in cluster age and mass bootstrapped from our model.

greater than $10^7 M_\odot$, including one cluster with a total mass of $\sim 10^8 M_\odot$.

5. DISCUSSION

After determining ages, masses, and extinctions for the entire cluster sample we directly compare these distributions with those of nearby normal and interacting galaxies. We focus on the interpretation of the derived cluster age distribution and mass function, and briefly discuss the implications for cluster formation efficiency. Ultimately, we discuss to what degree the differences observed in our cluster population can be attributed to the extreme star-forming environment unique to LIRGs in the local Universe. Individual cluster age and mass functions for the most ‘cluster-rich’ (i.e. greater than 25 detected clusters) galaxies are computed in Table 2.

5.1. Age Distribution

We consider the age distribution of clusters in our complete LIRG sample over the two mass ranges (i.e., Regions 1 and 2) described in §4.3. Specifically, we are interested in measuring the power law index γ , where $dN/d\tau = \tau^\gamma$. Figure 4 is a plot of the logarithm of the number of clusters per time interval, $\log(dN/d\tau)$, versus the logarithm of the cluster age, $\log(\tau)$. The plotted data are binned by 0.4 in $\log(\tau)$ so as to fully encapsulate the model errors of 0.3 in $\log(\tau)$ discussed in §4.1. We see that that a large fraction ($\sim 30\%$) of the clusters have ages less than 7.5 Myr. For the youngest most massive clusters in the sample (contained in Region 1), a weighted linear least-squares fit to the cluster age distribution gives a power law index of $\gamma = -0.9 \pm 0.3$, consistent with the derived power law index for the Antennae Galaxies within 1σ (Fall et al. 2005; Figure 2).

The distribution of the lower mass clusters (Region 2) can be fit with a power law index of $\gamma = -0.87 \pm$

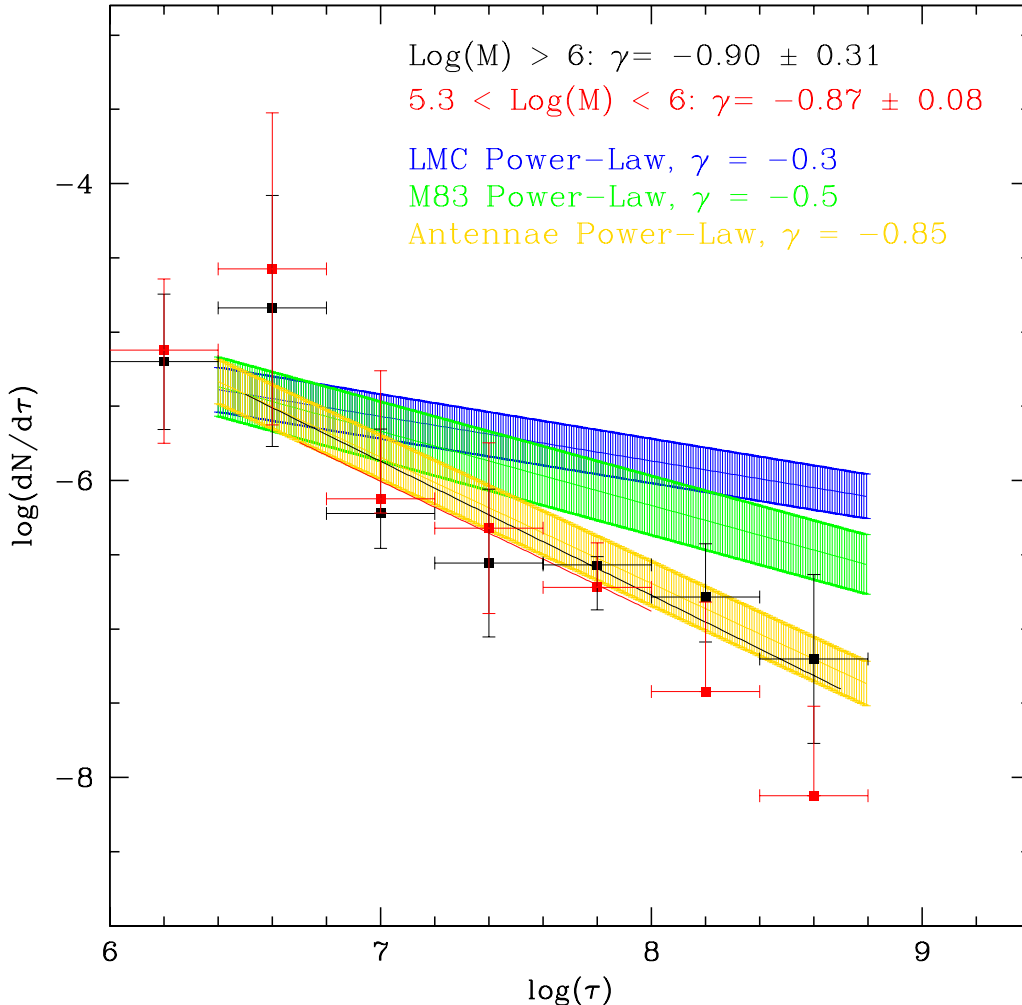


FIG. 4.— The stacked age distribution functions for all 27 galaxies. We have broken our age distribution up into the two age-mass ranges described in Equations 1 and 2, and shown as Regions 1 and 2 in the left panel of Figure 3. The red and black lines represent weighted linear least squares fits to the data. The blue, green, and yellow age functions of the LMC, M83, and the Antennae respectively, are taken from Adamo & Bastian 2016, and are normalized to the total number of clusters in our sample to best compare the slope for each galaxy.

0.1, also consistent with the derived power law index for the Antennae Galaxies within 1σ . The change in γ (~ 0.04) for the solar and sub-solar models was less than the uncertainty in the fit to the data in Figure 4. The similarity in the slope of the power-law index between the two mass-cuts is also further confirmation that we are working in a mass-limited regime, where the slope of the age distribution does not get systematically flatter with increasing cluster mass or distance to the host galaxy (Bastian 2016).

Also plotted in Figure 4 are the age distributions for M83 and the LMC, normalized to the fitted-number of clusters in the youngest age bin. As can be seen, γ for the LIRG sample is steeper than what is measured for these lower mass, normal star-forming systems. In addition, Adamo & Bastian (2016) provide a Table summary of γ for several local galaxies; in all cases, γ is flatter than -1.

There are two possible interpretations of this plot:

(1) If a continuous (or near continuous) cluster formation rate is assumed during the merging process for each LIRG, then the index of $\gamma = -1$ is an indication that 90% of the clusters formed are disappearing every age

dex. In the case of the Antennae Galaxies, Fall et al. (2005) concluded that the majority of the clusters are rapidly disrupted within the merger via ‘infant mortality’. This scenario not only seems to fit into the nature of the violent environments of galaxy mergers, but may also explain the negative value of γ (albeit, not as negative as measured for mergers) observed in lower-mass, less star-forming, quiescent nearby spirals.

We note that when discussing ‘infant mortality’, it is important to mention that the rapid decrease in the number of clusters as a function of age could be due to the inclusion of young, low-density, unbound OB associations in cluster catalogues (e.g., Bastian et al.2012; Silva-Villa et al. 2014). When these associations are removed, the age distributions for local star-forming galaxies appear to flatten. Kruijssen et al. (2015) point out that these effects can be minimized by selecting slightly older clusters (10 – 50 Myr), so that associations will have already been dispersed into the field. If this were a dominant effect in our sample, we would expect the age distribution of Region 2 to be much flatter and inconsistent with the Antennae value. Further, while we cannot verify the

amount of contamination from OB associations for the youngest clusters ($t < 10$ Myr) in our sample, the high mass cut-off for Region 1, ensures that this effect is minimized.

(2) The star formation rate has increased such that the bulk of the star formation, and cluster formation, has happened fairly recently as a result of the interaction of the two galaxies. This seems unlikely due to the fact that many of the galaxies within the sample have been interacting for a few hundred million years, whereas the median age of clusters for the whole sample is only $\sim 10^7$ years. Hopkins et al. (2013) finds that when simulations use realistic prescriptions for galaxy feedback, the star formation in a galaxy merger can in fact be time-variable and drops between each passage. Therefore, the average SF enhancement is only ever a factor of a few during the course of a merger, which is not enough to explain a 90% decrease in the number of clusters at each age dex (Karl et al. 2011). We could assume that all of the galaxies across the various merger stages are being viewed at these bursty peaks in the star formation rate, but we also consider this an unlikely scenario.

Under this framework, we would also be forced to accept that the star formation rates in nearby normal galaxies (which have negative γ values - though, note the above discussion of possible OB association contamination) are also increasing. In well-studied star-forming galaxies like the Milky Way and the Magellanic Clouds, the SFR is observed to have been nearly constant over the last Gyr, which argues strongly for the fact that the decline in $dN/d\tau$ is primarily a consequence of disruption in the MW and Magellanic Clouds (Harris & Zaritsky 2009; Chandar et al. 2010a).

Given the above, the most plausible explanation is that clusters are being rapidly destroyed in luminous galaxy mergers at a rate that exceeds the cluster destruction process occurring in nearby normal galaxies.

5.2. Mass Function

The cluster mass function (CMF) has the form $dN/dM \sim M^\beta$. For star clusters in our sample, this was derived by stacking the mass distributions of each galaxy, keeping the binning constant (0.4 in $\log(M)$), and then performing a cluster-weighted linear least-square fit as a function of derived mass. For clusters with ages $t \leq 10^7$ years and $t \sim 10^8$ years, we derive a mass function with a $\beta = -1.95 \pm 0.11$ and -1.67 ± 0.33 , respectively (see Figure 5). By comparison, β is commonly measured to be -2 for the majority of lower luminosity star-forming galaxies, as well as the Antennae Galaxies (Larsen 2010). The change in β for the solar and sub-solar models was less than the uncertainty in the fit (i.e., < 0.1) to the data in Figure 5.

An alternative approach to modeling the ICMF is with a two component Schechter function of the form $dN/dM = (M/M_c)^\alpha e^{-(M/M_c)}$. For reference, the M_c , or characteristic mass, measured for the Milky Way is $\sim 10^5 M_\odot$ (Bastian 2008). If we assumed that a star formation rate of $\sim 100 M_\odot/\text{yr}$ went into forming only clusters, the number clusters with $M \geq 10^7 M_\odot$ would still be negligible for $M_c = 10^5 M_\odot$; even if these high SFRs could be sustained for ~ 100 Myrs. Thus, the mere presence of $10^7 M_\odot$ clusters in our sample indicates that the

cluster formation environment in more extreme systems is different than that observed in lower-luminosity spiral galaxies.

Larsen (2010) shows that a Schechter function with a canonical -2 power-law slope and $M_c = 10^{6.3} M_\odot$ can reproduce the observed distribution in the Antennae galaxies equally well. In Figure 5 it is clear that we cannot simply adopt these parameters to fit our observations. Instead, we require both a slightly shallower power-law slope and a slightly larger cut-off mass due primarily to the fact that we are observing clusters with masses greater than $10^{6.5} M_\odot$, which simply are not observed in the Antennae. It is important to note that our data (Region 3 + 4) is consistent to within 1σ of a -2 power law in dN/dM over the same mass range as the Antennae, but can also be fit at the high-mass end using a modified Schechter function with a cut-off mass of $10^7 M_\odot$. This is clearly larger than what has been recently observed in M31, where the observed cut-off mass for the cluster sample is $M_c \sim 8 \times 10^3 M_\odot$ (Johnson et al. 2017). Interestingly, in that work, the authors define a relationship for the expected M_c as a function of Σ_{SFR} as: $\log M_c = (1.07 \pm 0.10) \times \log \Sigma_{SFR} + (6.82 \pm 0.20)$. If a typical value of Σ_{SFR} for LIRGs in the GOALS sample is used (U et al. 2012), we expect an $M_c \sim 10^7 M_\odot$, which is consistent with our derived fit, and indicates that high-mass clusters can indeed form more efficiently in higher star-forming environments.

When interpreting these results, it is important to consider several possible factors which could affect our derived mass functions:

(1) If lower-mass star clusters are preferentially disrupted, the mass distribution of the surviving star clusters in a merger remnant will be shallower than what is observed in a quiescent spiral galaxy (Kruijssen et al. 2012; Li et al. 2016). We might also expect this to correspond to a steeper age distribution for the lower-mass cluster sample (Figure 4; Region 2), but given that our 'low-mass' clusters are still rather massive, the lack of a clear difference in $dN/d\tau$ is not surprising. Therefore, the cluster disruption in these galaxies appears to be mostly mass-independent (i.e., we find that $\gamma \sim -1$ over the mass range of $M_\odot = 10^5 - 10^6$), a finding that Whitmore et al (2010) confirmed for the Antennae over the same range of cluster masses (Figure 5; yellow track).

When we increase the lower limit cluster mass for Region 1 to $10^{6.5} M_\odot$ in Figure 4, we observe a disruption rate of $dN/d\tau \sim \tau^{-0.75 \pm 0.4}$. This leads us to conclude that cluster disruption in LIRGs appears largely consistent with what is seen in the Antennae up to $10^{6.5} M_\odot$. We note that the uncertainty on the measured slope is much larger than for Region 2, so in principle, gamma could be shallower than the Antennae Galaxies in this mass regime. However, if this were a strong effect in our data we would expect our observed CMF in Region 3 to be shallower than the -2 power-law used to represent the underlying ICMF.

(2) The choice of bin size for our data could systematically flatten the measured β (Maiz Apellaniz & Ubeda 2005). We use bin sizes in mass and age of 0.4 dex in $\log(M)$ and $\log(t)$, chosen to fully encapsulate the typical uncertainty associated with our age and subsequent mass estimations. To test the effect this choice has on the

measured slope, we explored two other bin sizes, 0.2 and 0.6 dex respectively. We found that the slopes derived for $dN/d\tau$ and dN/dM change on average by 0.1 – 0.2 dex. As this is comparable with the 1σ uncertainties on each slope measurement, we conclude our choice of bin size is not significantly affecting our determination of the shape of the cluster mass distribution.

(3) At the resolution of our observations, multiple lower mass clusters may appear as one, massive cluster, and thus systematically flatten the CMF. To test this possibility, we ran Source Extractor on B-band and I-band WFC images of NGC4038/9 from the Hubble Legacy Archive (HLA) to identify star clusters. The distance used for NGC4038/9 is ~ 24 Mpc, but the median distance of our sample is four times farther away. Since the pixel scale of the Drizzlepac output images is the same, we simply smoothed the HLA images with a boxcar function of 4 pixels. Source Extractor was then run on this smoothed image with the Source Extractor results from the original, pre-smoothed images as a reference. For this step, Source Extractor only outputs sources which are both identified in the smooth image and also match a source in the original list (within a search radius of 4 pixels, i.e., the same size as the smoothing). The ratio: $(N_{orig} - N_{smoothed})/N_{orig}$ should give an upper limit for the fraction of dual sources identified as 1 in the smoothed image.

For the B-band and I-band image comparisons, this ratio is 0.3 and 0.26, respectively. Thus, roughly 30% of ‘blended clusters’ identified in our LIRGs with $D \geq 100$ Mpc would actually be identified as a complex of single clusters at the resolution of the Antennae. By redistributing to the lower mass end this percentage of clusters, with masses greater than $5 \times 10^6 M_{\odot}$, we observe a steepening of the mass function ~ 0.1 dex. Despite this fact, it is clear that the existence of young high-mass ($\geq 10^7 M_{\odot}$) clusters in our sample cannot be solely attributed to a resolution limit. Finally, it is worth noting that cluster blending can effect the estimated cluster ages. The effect most likely pushes clusters toward the median cluster age, and thus if deblending randomly populates the young and old cluster parts of the age distribution, there will not be a dramatic effect on γ .

Given the above, it appears that the differences in the slope observed in the LIRG sample relative to the Antennae mass function is not caused by mass-dependent cluster disruption from $10^5 - 10^{6.5} M_{\odot}$. When we consider the effect of a resolution limit on the high-mass end of the distribution, we can reconcile the small discrepancies in the observed slopes. Therefore, cluster formation in these galaxies can be explained with a universal -2 power law fit to the mass distribution up to at least $10^{6.5} M_{\odot}$. However, we emphasize that the prevalence of the most-massive clusters observed in the sample is compelling evidence that these clusters exist more predominately in the more extreme star-forming environments of LIRGs.

This idea is further supported by the fact that a Schechter function, with an $M_c \sim 10^7 M_{\odot}$, can also fit our data over the full range of observed cluster masses relative to a simple power-law formalism. This implies that GMCs in LIRGs can have higher ISM pressures and densities than what has been seen in other galactic environments. Recently, Maji et al. (2016) used hydrodynamic simulations of two equal-mass MW-like merging

galaxies to show that such ISM conditions are actually capable of producing clusters in the range of $10^{5.5-7.5} M_{\odot}$ (Figure 4), consistent with the mass-scales we observe in our LIRG sample.

5.3. Merger Stage Dependence

Since our LIRG sample spans the full range of merger stages, we can test if our explanation of cluster formation and destruction depends on the dynamical state of the galaxy. Haan et al (2013), Kim et al. (2013), and Stierwalt et al. (2013) have classified the merger stage of each U/LIRG in the GOALS sample based on their morphological appearance at multiple wavelengths. These merger classification schemes run from pre-first passage to single coalesced nuclei. We separated the sample into early (classes 0-2), middle (classes 3-4), and late-stage (classes 5-6) mergers. In order to quantify any differences in each age distribution we ran a KS-test comparing the normalized distributions of the early, middle, and late-stage mergers to the total sample. We find that within our sub-sample of GOALS LIRGs these individual merger stage distributions are drawn from the same parent distribution of ages with a 92% probability or higher.

For galaxies classified across all merger stage bins we find that the most massive clusters in the sample (Region 1) are always consistent with a -1 power law in $dN/d\tau$, which is further justification for combining the cluster populations for each galaxy into a single sample, and indicates that disruption does not vary much, within uncertainty, throughout the merger. It also provides credence to the idea that the SFR of a merging galaxy is bursty, which given the large size of our age bins, is an effect on the age distribution we can safely ignore. This allows us to characterize each galaxy as having an elevated but roughly continuous SFR.

When breaking the sample down to early and mid-stage mergers in Figure 6 we find that star clusters in both early and mid-stage mergers show a power-law distribution of $dN/dM \sim M^{-1.8}$ across both age-regimes. Additionally, each mass function is normalized by the total duration within their respective age bin in order to remove any artifacts of the bins having different time ranges. This helps to emphasize that the number of clusters that survive decreases in absolute number and independent of mass from the pre- to ongoing-merger systems.

Under the assumption of a constant SFR, the youngest clusters in each galaxy merger class will show the same slope in dN/dM . Our results are consistent with the idea that the star formation history is not changing significantly between merger stages, and thus cannot be a dominant effect in driving the observed age distributions we see for our sample, when combining all galaxies together.

Additionally, when analyzing the cluster mass distribution we assumed that the formation conditions (i.e characteristic mass M_c and slope α) do not change significantly throughout the merging process. The similarity of the slopes between each merger class is consistent with simulations of merging disk galaxies, which find that the characteristic mass M_c evolves at a rate of only $\sim 0.3 - 0.4$ dex/Gyr (Kruijssen et al. 2012).

5.4. Cluster Formation Efficiency

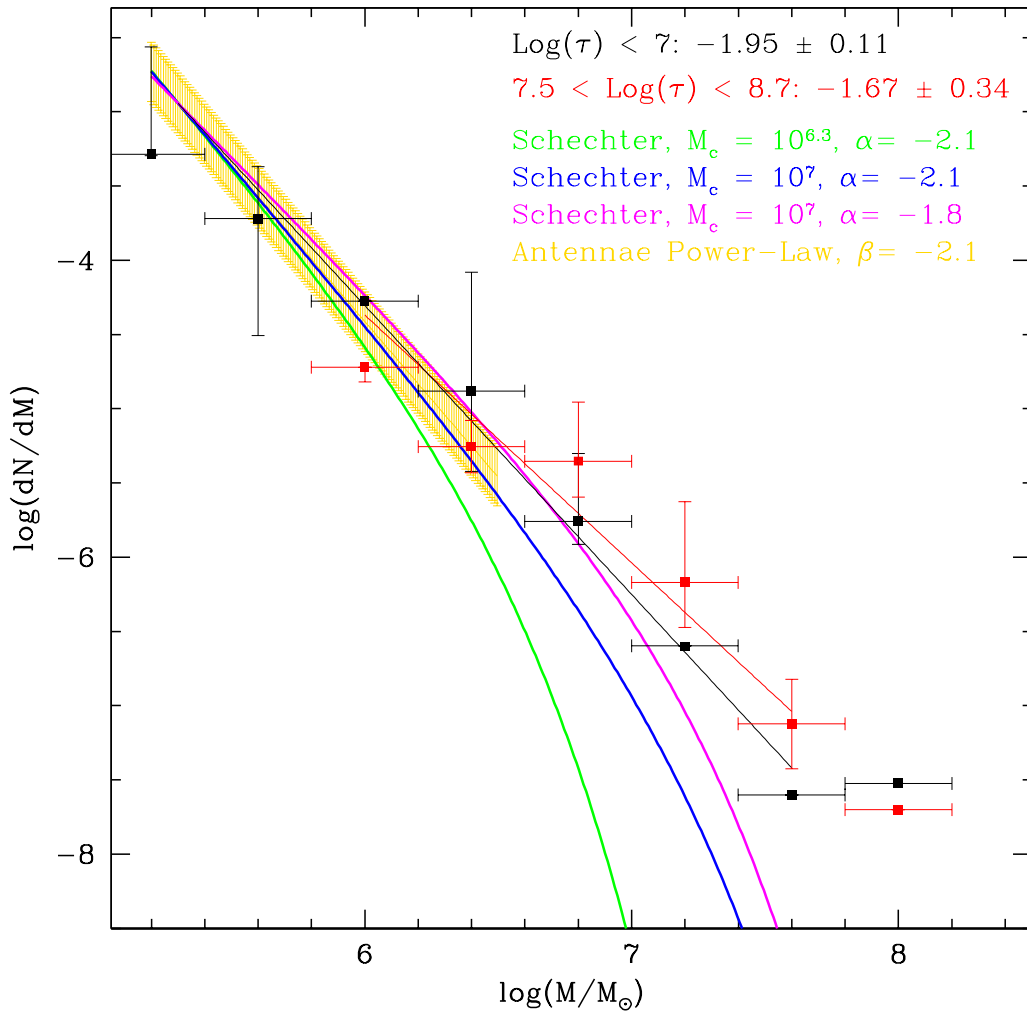


FIG. 5.— The stacked mass distribution functions for all 27 galaxies. We have separated our mass distribution up into two mass-age ranges described in Equations 3 and 4, and shown as Regions 3 and 4 in the right panel of Figure 3. These cuts allow us to test the effects of our completeness limits and the mass dependence of cluster disruption in the sample. The red and black lines represent weighted linear least squares fits to the data. The yellow error bars represent the mass function of the Antennae taken Whitmore et al. (2010), and is normalized to the total number of clusters in our sample. The green, magenta, and blue lines represent three different analytic Schechter function fits to the empirical distribution.

TABLE 2
DERIVED AGE AND MASS FUNCTION SLOPES

Name	$\gamma_{0.02}$	σ_γ	$\gamma_{0.008}$	σ_γ	$\beta_{0.02}$	σ_β	$\beta_{0.008}$	σ_β
NGC 1614	-0.96	0.18	-1.16	0.17	-1.35	0.23	-1.60	0.10
NGC 7674	-1.67	0.46	-0.78	0.28	-1.15	0.12	-1.32	0.29
NGC 3690E	-0.62	0.54	-1.01	0.44	-1.44	0.14	-1.31	0.23
NGC 3690W	-1.26	0.12	-1.24	0.14	-1.92	0.24	-1.45	0.26
Arp 148	-0.87	0.38	-1.38	0.69	-1.44	0.17	-1.8	0.18
IRAS 20351+2521	-1.19	0.11	-1.27	0.10	-1.60	0.52	-1.12	0.25
NGC 6786	-1.29	0.18	-1.17	0.26	-1.40	0.12	-1.58	0.21
UGC 09618NED02	-1.18	0.23	-1.42	0.12	-2.13	0.47	-1.52	0.31

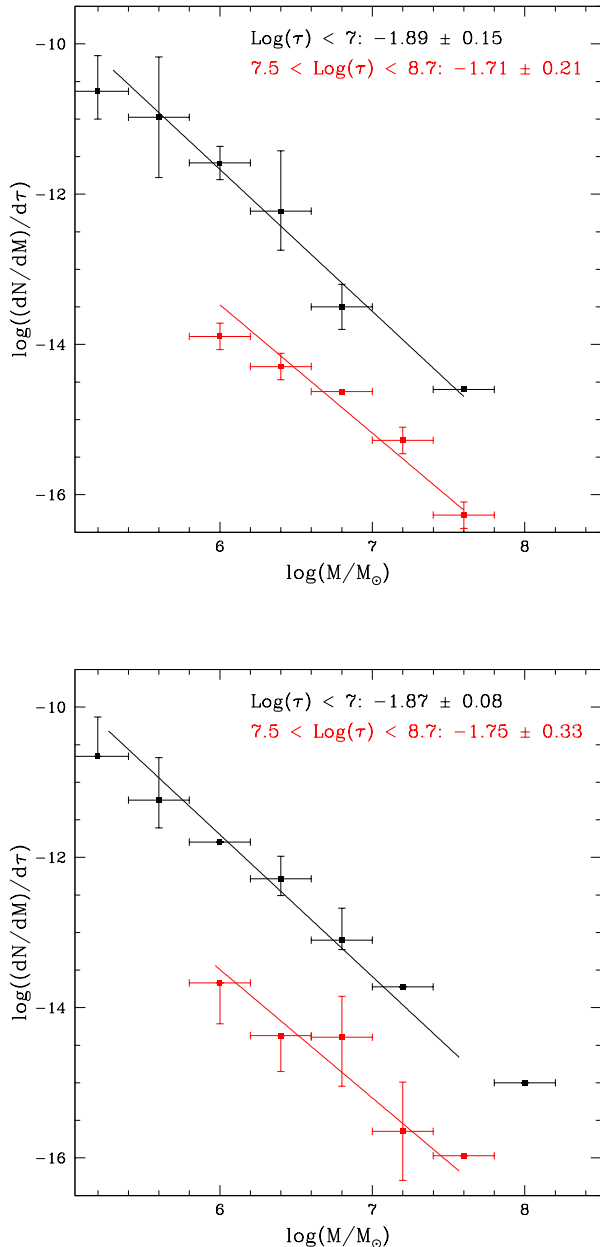


FIG. 6.— The stacked age-normalized mass distribution functions for the 11 galaxies with a merger class of 0-2 (Top Plot) and the 8 galaxies with a merger class 3-4 (Bottom Plot) identifying them as early-stage and mid-stage mergers respectively. The total number of clusters in each class is 260 and 154 for pre- and mid-stage mergers respectively. We have broken our mass distribution up into the same age ranges as in Figure 5

Finally, we consider the efficiency of cluster formation (CFE) within the high star formation rate environments of LIRGs. CFE, or Γ , is defined the ratio of the rate of stellar mass formation in bound clusters, \dot{M}_{SC} , to the global star formation rate, \dot{M}_{SF} , over the same time interval, i.e.,

$$\Gamma = \frac{\dot{M}_{SC}}{\dot{M}_{SF}} \times 100\%. \quad (9)$$

For our sample, the fact that we do not detect clusters well below $10^5 M_{\odot}$, and that we have significant cluster disruption over all masses, makes the estimation of the cluster formation efficiency (CFE) highly uncertain.

This is compounded by the fact that our UV-Bright cluster population is not sampling the full SFR as traced by the total UV+IR based SFR measurements from Howell et al. (2010). Additionally, we cannot match our UV-based CFR to the total GALEX UV SFR estimation because the field of view of the SBC is $\sim 1/140$ that of GALEX, and thus a correction for the clusters we miss is uncertain. The large amount of obscuring dust also makes a completeness correction to derive a total mass and CFR based on our mass distributions difficult for our LIRG sample. Johnson et al. (2016) notes that CFE calculations are best done in dust-free environments that show little sign of significant cluster disruption, a scenario we are simply not presented with in our sample. Therefore we leave a discussion about CFE in LIRGs to future studies involving deep IR-based observations that have both a larger FOV, and the ability to detect more dust-enshrouded low-mass clusters.

6. SUMMARY

Hubble Space Telescope ACS/HRC FUV (F140LP) and ACS/WFC optical (F435W and F814W) observations of a sample of 22 star cluster-rich LIRGs in the GOALS sample were obtained. These observations have been utilized to derive the ages and masses of the star clusters contained within these systems in order to examine the cluster properties in extreme starburst environments relative to those in nearby, lower luminosity star-forming galaxies. The following conclusions are reached:

- (1) We have detected 665 clusters within the inner $30'' \times 30''$ of these 22 LIRGs (27 nuclei). These clusters have $S/N \geq 5$ in all three filters and de-convolved FWHMs as measured by ISHAPE of ≤ 2 pixels.
- (2) Cluster ages have been derived by assuming an instantaneous SSP, Salpeter IMF, and either a solar or sub-solar metallicity. By requiring the derived cluster ages to be consistent when using both a color-color and SED-based fitting technique, we obtain a final sample of 484 clusters whose properties are reliably constrained within the 1σ uncertainties of the SSP models. The derived cluster ages imply a disruption rate of $dN/d\tau = \tau^{-0.9+/-0.3}$ for cluster masses $\geq 10^6 M_{\odot}$, and $dN/d\tau = \tau^{-0.87+/-0.08}$ for cluster masses $10^{5.3} < M < 10^6 M_{\odot}$. This is consistent with what is seen in the Antennae, and indicates the general influence mergers have on the creation and destruction of star clusters. The measured γ is steeper than that measured for lower mass, less star-forming systems in the local Universe, implying that the merging process produces a fundamentally different cluster disruption law.
- (3) We have identified a large number of $M \geq 10^6 M_{\odot}$ clusters in the sample, which indicates that the more extreme star-forming environments of LIRGs are capable of producing more high-mass clusters than what is observed in galaxies like the Milky Way or even the Antennae (Larsen 2009; Bastian et al. 2012; Whitmore et al. 2010). The derived cluster masses also imply a CMF for the sample of $dN/dM = M^{-1.95+/-0.11}$, which is consistent with a -2 power law in dN/dM . Together with the

fact that we do not see a significant change in the age distribution slope as a function of mass, we interpret our mass function slope as evidence against mass-dependent cluster disruption at $M \geq 10^{5.3} M_{\odot}$ which would flatten the observed CMF relative to a canonical -2 power law in this regime.

The authors thank B. Whitmore, R. Chandar, A. Mulia, and G. Soutchkova for useful discussions and assistance. The authors also thank the referee for detailed comments and suggestions which have improved the manuscript. S.T.L. was supported by the NASA VSGC Graduate Fellowship. A.S.E., and D.C.K. were supported by NSF grant AST 1109475 and by NASA through grants HST-GO10592.01-A, HST-GO11196.01-A, and HST-GO13364 from the Space Telescope Science Institute, which is operated by the Association

of Universities for Research in Astronomy, Inc., under NASA contract NAS5-26555. G.C.P. was supported by a FONDECYT Postdoctoral Fellowship (No. 3150361). A.S.E. was also supported by the Taiwan, R.O.C. Ministry of Science and Technology grant MoST 102-2119-M-001-MY3. T.D-S. acknowledges support from ALMA-CONICYT project 31130005 and FONDECYT regular project 1151239.

Portions of this work were performed at the Aspen Center for Physics, which is supported by National Science Foundation grant PHY-1066293. This work was partially supported by a grant from the Simons Foundation. Finally, This research has made use of the NASA/IPAC Extragalactic Database (NED) which is operated by the Jet Propulsion Laboratory, California Institute of Technology, under contract with the National Aeronautics and Space Administration.

REFERENCES

- Adamo & Bastian 2016, *The Origin of Stellar Clusters*, Stahler (Springer)
- Adamo et al. 2011, *MNRAS*, 414, 1793
- Adamo et al. 2015, *IAU*, 316
- Alonso-Herrero et al. 2001, *ApJ*, 546, 952
- Anders, P., Bissantz, N., Fritze-v. Alvensleben, U., & de Grijs, R. 2004, *MNRAS*, 347, 196
- Anders et al. 2007, *MNRAS*, 377, 91
- Armus et al. 2009, *PASP*, 121, 559
- Bastian et al. 2006, *A&A*, 445, 471
- Bastian 2008, *ASPC*, 390, 47
- Bastian 2008, *MNRAS*, 390, 759
- Bastian et al. 2012, *MNRAS*, 419, 2606
- Bastian, N., Schweizer, F., Goudfrooij, P., Larsen, S. S., & Kissler-Patig, M. 2013, *MNRAS*, 431, 1252
- Bastian, N. 2016, arXiv:1606.09468
- Bertin & Arnouts 1996, *A&AS*, 117, 393
- Bruzual & Charlot 2003, *MNRAS*, 344, 1000
- Calzetti, D., Kinney, A. L., & Storchi-Bergmann, T. 1994, *ApJ*, 429, 582
- Calzetti, D., Armus, L., Bohlin, R. C., et al. 2000, *ApJ*, 533, 682
- Cao et al. 2015, Accepted
- Chandar et al. 2010a, *ApJ*, 711, 1263
- Chandar et al. 2010b, *ApJ*, 713, 1343
- Chandar et al. 2015, *ApJ*, 810, 1
- Charlot & Fall 2000, *ApJ*, 539, 718
- Chien et al. 2007, *ApJ*, 660, 105
- Chien, L. 2010, *ASPC*, 423, 197C
- Cook et al. 2012, *ApJ*, 751, 100
- Dametto et al. 2014, *MNRAS*, 443, 1754
- Davies et al. 2016, Submitted
- de Grijs et al. 2003, *MNRAS*, 343, 1285
- Di Matteo, Springel & Hernquist 2005, *Nature*, 433, 604
- Evans et al. 2008, *ApJ*, 675, 69
- Evans et al. 2017, in prep.
- Fall et al. 2005, *ApJ*, 631, 133
- Fall 2006, *ApJ*, 652, 1129
- Fall et al. 2009, *ApJ*, 704, 453
- Fall & Chandar 2012, *ApJ*, 752, 96
- Fitzpatrick et al. 1999, *PASP*, 111, 63
- Fouesneau et al. 2012, *ApJ*, 750, 60
- Gieles 2009, *Ap&SS*, 324, 299
- Gieles et al. 2005, *A&A*, 441, 949
- Gnedin, O. Y., & Ostriker J. P., 1997, *ApJ*, 474, 223-255
- Goddard et al. 2010, *MNRAS*, 405, 857
- González Delgado, R. M., Cerviño, M., Martins, L. P., Leitherer, C., & Hauschildt, P. H. 2005, *MNRAS*, 357, 945
- Haan et al. 2013, *MNRAS*, 434, 1264
- Harris & Zaritsky 2009, *AJ*, 138, 1243
- Homeier, Gallagher & Pasquali 2002, *A&A*, 391, 857
- Hopkins et al. 2013, *MNRAS*, 430, 1901-1927
- Howell et al. 2010, *ApJ*, 715, 572
- Hunter et al. 2003, *AJ*, 126, 1836
- Humphreys, R. M., & Davidson, K. 1979, *ApJ*, 232, 409
- Inami et al. 2010, *AJ*, 140, 63
- Jog & Solomon 1992, *ApJ*, 387, 152
- Johansson & Bergvall 1988, *A&A*, 192, 81
- Johnson, L. C., Seth, A. C., Dalcanton, J. J., et al. 2016, *ApJ*, 827, 33
- Johnson, L. C., Seth, A. C., Dalcanton, J. J., et al. 2017, arXiv:1703.10312
- Joy & Harvey 1997, *ApJ*, 315, 1480
- Karl et al. 2011, *ApJ*, 734, 11
- Kennicutt et al. 2009, *ApJ*, 703, 1672
- Kewley et al. 2010, *ApJ*, 721, 48
- King 1966, *AJ*, 71, 276
- Kruijssen 2012, *MNRAS*, 426, 3008
- Kruijssen 2014, *ASSP*, 36, 437
- Kruijssen et al. 2012, *MNRAS*, 421, 1927
- Kruijssen, J. M. D., & Bastian, N. 2016, *MNRAS*, 457, L24
- Larsen & Brodie 2002, *AJ*, 123, 1488
- Larsen & Richtler 2000, *A&A*, 354, 836
- Larsen 1999, *A&AS*, 139, 393
- Larsen 2009, *A&A*, 494, 539
- Larsen 2010, *RSPTA*, 368, 867
- Larson 1976, *MNRAS*, 176, 31
- Leech et al. 1989, *MNRAS*, 240, 349
- Leitherer et al. 1999, *ApJ*, 123, 3
- Li, H., Gnedin, O. Y., Gnedin, N. Y., et al., 2016, arXiv:1608.03244
- Lutz 1992, *A&A*, 259, 462
- Magnelli, B. et al. 2011, *A&A*, 528, 35
- Maiz Apellaniz, J., & Ubeda, L. 2005, *ApJL*
- Maji, M., Zhu, Q., Li, Y., et al. 2016, arXiv:1606.07091
- Maoz, D., Barth, A. J., Ho, L. C., Sternberg, A., & Filippenko, A. V. 2001, *AJ*, 121, 3048
- Maraston, C., Bastian, N., Saglia, R. P., et al. 2004, *A&A*, 416, 467
- Martin et al. 1991, *A&A*, 245, 393
- Matteucci & Franco 1989, *MNRAS*, 239, 885
- Mazzarella, et al. 2012, *AJ*, 144, 125
- Meurer, G. R., Heckman, T. M., Leitherer, C., Kinney, A., Robert, C., & Garnett, D. R. 1995, *AJ*, 110, 2665
- Mihos & Hernquist 1996, *ApJ*, 464, 641
- Miller et al. 1997, *AJ*, 114, 2381
- Miralles-Caballero et al. 2012, *A&A*, 538, 61
- Modica et al. 2012, *AJ*, 143, 16
- Momjian et al. 2003, *ApJ*, 597, 809
- Mulia et al. 2015, *ApJ*, 805, 99
- Naab & Ostriker 2006, *MNRAS*, 366, 899
- Pasquali, de Grijs & Gallagher 2003, *MNRAS*, 345, 161
- Privon et al. 2013, *ApJ*, 771, 120
- Reines et al. 2008, *AJ*, 135, 2222
- Rich et al. 2012, *ApJ*, 753, 5
- Rupke et al. 2008, *ApJ*, 674, 172
- Salpeter 1955, *ApJ* 121, 161
- Sanders & Mirabel 1996, *ARA&A* 34, 749

- Sanders et al. 2003, AJ, 126, 1607
 Schlafly & Finkbeiner 2011, ApJ 737, 103, 2011
 Schweizer & Seitzer 1998, AJ, 116, 2206
 Schweizer et al. 1996, AJ, 112, 1839
 Schweizer et al. 2004, ASPC, 322, 111
 Silva-Villa, E., Adamo, A., Bastian, N., Fouesneau, M., & Zackrisson, E. 2014, MNRAS, 440, L116
 Sirianni et al. 2005, PASP, 117, 1049
 Smith et al. 2014, AJ, 147, 60
 Smith et al. 2016, Submitted
 Soto & Martin 2010, ApJ, 716, 332
 Stierwalt et al. 2013, ApJS, 206, 1
 van den Broek et al. 1991, A&A, 91, 61
 van Driel et al. 2001, AA&A, 368, 64
 Vavilkin et al. 2011, PhD, 8
 Vavilkin et al. 2015, in prep.
 Whitmore & Schweizer 1995, AJ, 109, 960
 Whitmore et al. 1997, AJ, 114, 1797
 Whitmore et al. 1999, AJ, 118, 1551
 Whitmore & Zhang, 2002, AJ, 124, 1418
 Whitmore et al. 2007, AJ, 133, 1067
 Whitmore et al. 2010, AJ, 140, 75
 Whitmore, B., Chandar, R., Bowers, A., et al. 2014, AJ, 147, 78
 Wilson et al. 2006, ApJ, 641, 763
 Wilson et al. 2008, ApJ, 178, 189
 Zhang Q., Fall S. M., 1999, ApJ, 527, L81
 Zepf et al. 1999, AJ, 118, 752

APPENDIX
 GALAXY DESCRIPTIONS

In the following sections we give a brief description of the basic morphology and star cluster spatial distributions within each galaxy, as well as the adopted values for the maximum amount of visual extinction we use in our model. See Evans et al. 2017 for a detailed description of all 88 LIRGs in the GOALS sample that have been observed with HST.

NGC 0017

NGC 0017 is a late stage merger that contains a single resolved nucleus surrounded by dust lanes associated with spiral arms in the inner few kpc. Several bright star clusters are visible within this nuclear spiral region. The maximum A_V adopted for this galaxy is 3.0 mags of visual extinction. (Dametto et al. 2014).

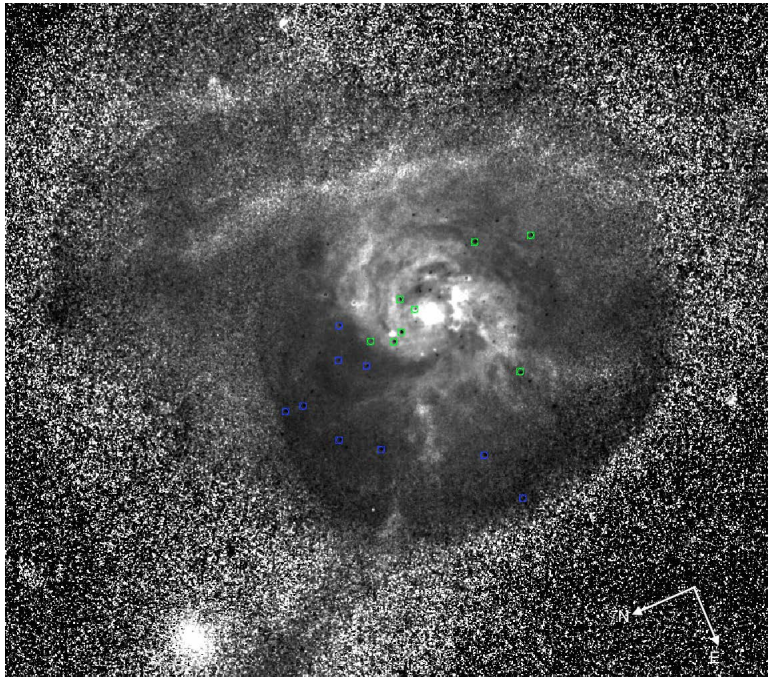


FIG. 7.— Inverted black and white B-I image of NGC 0017 taken with HST ACS/WFC F814W and F435W. The bright emission corresponds to redder (i.e. dustier) regions of the galaxy. The blue centroids correspond to clusters found in relatively “dust-free” regions of these galaxies, whereas the green centroids correspond to clusters found in relatively dustier regions of the galaxy.

Arp 256S

Arp 256 is a mid-stage merger containing a southern (MCG-02-01-051) and northern (MCG-02-01-052) galaxy. Arp 256S has an elongated $\sim 1''$ (400 pc) nucleus, and the north and southwest tails contain the majority of the star clusters in the galaxy. The maximum A_V adopted for this galaxy is 1.7 mags of visual extinction (Smith et al. 2014).

Arp 256N

Arp 256N has a central, point-like nucleus. The majority of the star clusters are seen along the tidal tails in this galaxy. The maximum A_V adopted for this galaxy is 1.7 mags of visual extinction (Smith et al. 2014).

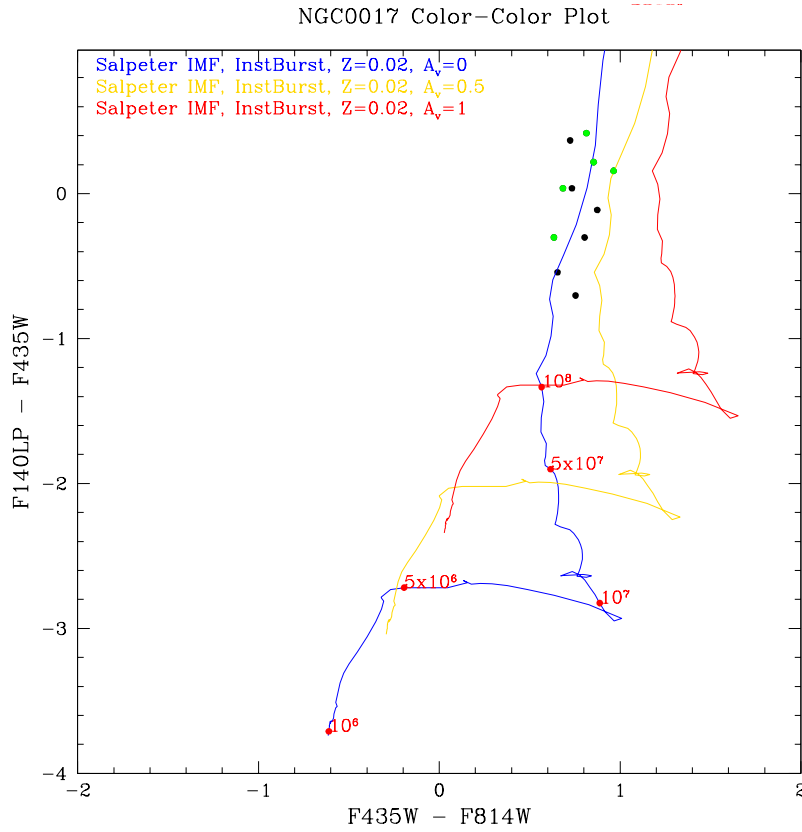


FIG. 8.— Color-Color plot of all star clusters identified in NGC 0017 in F814W, F435W, and F140LP plotted against SSP models with various amount of visual extinction. The green points correspond to the clusters found in dustier regions of the galaxy in Figure 7

TABLE 3
OBSERVED PROPERTIES OF STAR CLUSTERS IN NGC 0017

ID	RA	Dec	M_B	σ_B	M_I	σ_I	M_{FUV}	σ_{FUV}
1	2.776819641	-12.10616498	-13.81	0.01	-14.87	0.01	-12.67	0.03
2	2.777320196	-12.10713204	-13.89	0.01	-14.53	0.01	-14.20	0.01
3	2.777273773	-12.10658526	-11.05	0.06	-11.91	0.05	-10.84	0.18
4	2.777432692	-12.10695518	-13.56	0.01	-14.43	0.01	-12.32	0.05
5	2.777660645	-12.10636335	-12.56	0.01	-13.44	0.01	-12.68	0.03
6	2.778745035	-12.10880075	-14.29	0.01	-15.27	0.01	-12.96	0.02
7	2.777920896	-12.10509066	-12.03	0.01	-12.76	0.01	-11.67	0.08
8	2.778717571	-12.10546794	-10.72	0.02	-11.38	0.02	-11.27	0.12
9	2.779140091	-12.10608216	-15.05	0.01	-15.86	0.01	-15.36	0.01
10	2.779887259	-12.10772035	-11.65	0.01	-12.39	0.01	-11.62	0.16
11	2.780845501	-12.10807908	-10.35	0.03	-11.11	0.03	-11.06	0.02
12	2.777023706	-12.10749699	-13.10	0.04	-14.80	0.16	-11.10	0.14
13	2.776766427	-12.10731248	-13.23	0.02	-14.20	0.02	-13.08	0.02
14	2.776532232	-12.10983287	-11.54	0.01	-12.36	0.01	-11.13	0.08
15	2.776287946	-12.10888848	-13.35	0.01	-14.04	0.01	-13.32	0.02

NGC 0695

NGC 0695 is a face-on spiral galaxy with a companion at a projected nuclear separation of $\sim 26''$ (16 kpc) to the northwest. There are multiple spiral arms on the northwestern half of the galaxy, and star clusters are distributed throughout disk. The maximum A_V adopted for this galaxy is 2.8 mags of visual extinction (Kennicutt et al. 2009).

UGC 02369

UGC 02369 is a mid-stage merger consisting of a southern face on galaxy (MCG +02-08-029) and an inclined northern galaxy (MCG +02-08-030). The nuclei of the two galaxies are separated by $\sim 21''$ (13 kpc). A spiral arm containing multiple star clusters extends from the nucleus of the southern galaxy towards the northern galaxy. The maximum A_V adopted for this galaxy is 2.3 mags of visual extinction (van Driel et al. 2001).

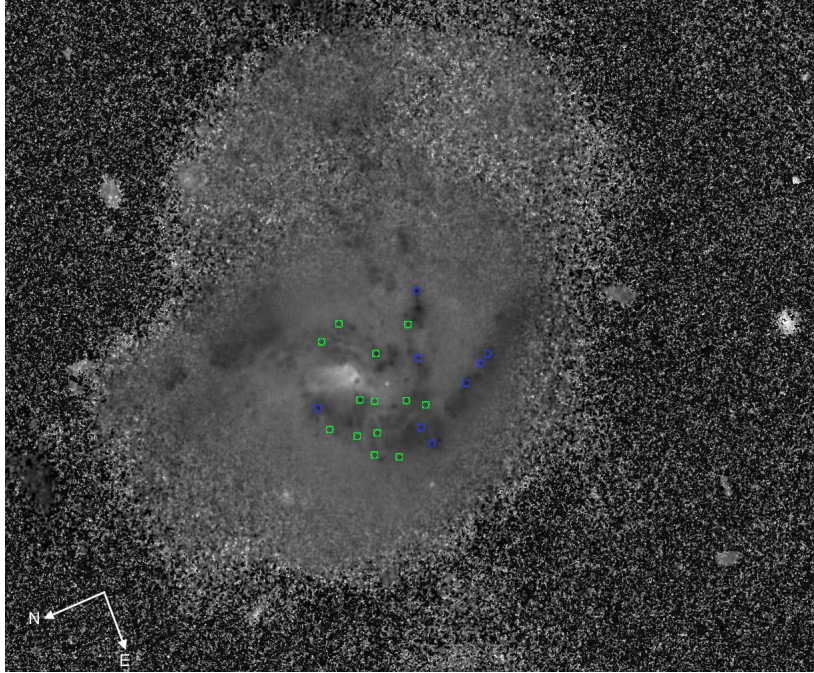


FIG. 9.— Inverted black and white B-I image of Arp 256S taken with HST ACS/WFC F814W and F435W. The bright emission corresponds to redder (i.e. dustier) regions of the galaxy. The blue centroids correspond to clusters found in relatively “dust-free” regions of these galaxies, whereas the green centroids correspond to clusters found in relatively dustier regions of the galaxy.

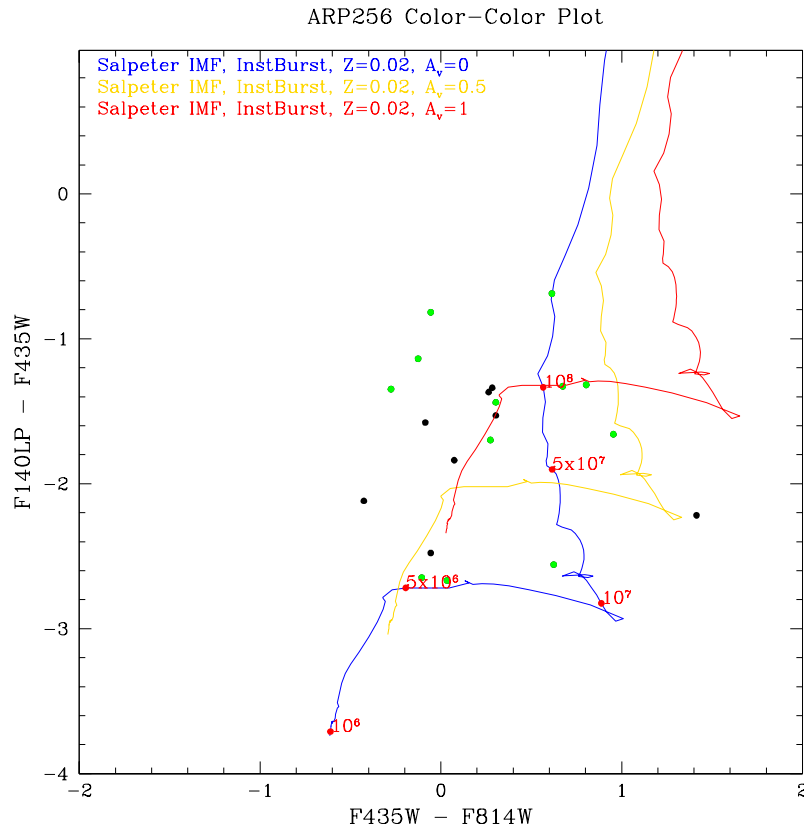


FIG. 10.— Color-Color plot of all star clusters identified in Arp 256S in F814W, F435W, and F140LP plotted against SSP models with various amount of visual extinction. The green points correspond to the clusters found in dustier regions of the galaxy in Figure 9

TABLE 4
DERIVED PROPERTIES OF STAR CLUSTERS IN NGC 0017

ID	Log(Age)	σ_{Age}	Log(M/M_{\odot})	σ_M	A_V	σ_{A_V}
1	8.61	0.02	7.34	0.16	0.20	0.05
2	8.36	0.02	7.11	0.17	0.10	0.06
3	8.46	0.58	6.04	0.61	0.10	0.63
4	8.66	0.02	7.18	0.16	0.01	0.04
5	6.66	0.81	6.18	0.70	1.90	0.77
6	8.66	0.69	7.47	0.16	0.01	5.27
7	6.66	0.03	6.08	0.16	2.10	0.04
8	6.66	0.79	5.29	0.69	1.60	0.74
9	6.64	0.10	7.10	0.16	1.80	5.62
10	6.66	2.37	5.87	0.16	2.00	4.73
11	6.34	0.86	5.65	0.67	2.10	0.71
12	8.46	0.18	7.55	0.52	1.40	0.51
13	8.36	0.29	7.00	0.37	0.40	0.33
14	8.51	1.93	6.23	0.16	0.01	0.03
15	8.46	5.32	6.91	0.16	0.01	0.78

TABLE 5
OBSERVED PROPERTIES OF STAR CLUSTERS IN ARP 256S

ID	RA	Dec	M_B	σ_B	M_I	σ_I	M_{FUV}	σ_{FUV}
1	4.713679548	-10.37685826	-10.41	0.05	-11.03	0.07	-12.97	0.05
2	4.710809481	-10.37888736	-12.54	0.01	-12.61	0.02	-14.38	0.01
3	4.710599656	-10.377146	-10.45	0.13	-10.34	0.22	-13.10	0.04
4	4.711341331	-10.37839176	-11.99	0.02	-12.79	0.02	-13.31	0.03
5	4.71074686	-10.37664793	-12.51	0.03	-13.46	0.04	-14.17	0.03
6	4.711535325	-10.37750998	-13.53	0.02	-13.80	0.02	-15.23	0.02
7	4.712724227	-10.37952183	-10.43	0.15	-11.84	0.08	-12.65	0.13
8	4.712065091	-10.37821862	-12.93	0.03	-13.21	0.04	-14.27	0.03
9	4.712819126	-10.37928414	-11.79	0.05	-12.05	0.09	-13.16	0.08
10	4.713033719	-10.37882884	-12.69	0.02	-12.63	0.05	-15.17	0.02
11	4.712218761	-10.37674074	-14.31	0.02	-14.61	0.02	-15.75	0.01
12	4.712398738	-10.3769871	-12.19	0.03	-12.13	0.21	-13.01	0.05
13	4.712719547	-10.37756498	-11.80	0.06	-11.67	0.12	-12.94	0.10
14	4.71300344	-10.37787256	-12.42	0.03	-13.03	0.03	-13.11	0.04
15	4.71191981	-10.37588942	-12.99	0.03	-12.56	0.06	-15.11	0.01
16	4.713366435	-10.37755202	-13.26	0.05	-13.56	0.07	-14.79	0.03
17	4.713006219	-10.37670878	-11.65	0.10	-11.37	0.15	-13.00	0.05
18	4.712859587	-10.37631389	-11.93	0.03	-12.60	0.05	-13.26	0.04
19	4.713776161	-10.37757731	-12.27	0.04	-12.18	0.04	-13.85	0.06
20	4.713381893	-10.37643331	-10.68	0.07	-10.71	0.14	-13.35	0.03

TABLE 6
DERIVED PROPERTIES OF STAR CLUSTERS IN ARP 256S

ID	Log(Age)	σ_{Age}	Log(M/M_{\odot})	σ_M	A_V	σ_{A_V}
1	6.88	0.17	4.60	0.20	0.10	0.07
2	6.64	0.02	5.51	0.18	0.70	0.05
3	5.10	0.43	5.10	0.33	0.80	0.23
4	7.81	0.42	6.12	0.34	0.30	0.28
5	7.54	0.28	6.24	0.26	0.40	0.18
6	6.46	0.27	6.49	0.33	1.30	0.27
7	5.10	0.09	5.57	0.29	1.70	0.16
8	6.66	0.04	5.85	0.20	1.00	0.09
9	6.66	0.41	5.40	0.29	1.00	0.22
10	6.40	0.64	5.78	0.35	0.80	0.30
11	6.60	0.06	6.34	0.23	1.00	0.15
12	6.66	0.25	5.66	0.28	1.20	0.21
13	6.66	0.72	5.40	0.21	1.00	0.10
14	6.66	0.81	5.92	0.68	1.50	0.73
15	6.66	0.76	5.56	0.18	0.40	0.04
16	6.56	0.17	5.99	0.35	1.10	0.30
17	6.66	0.76	5.29	0.24	0.90	0.11
18	6.74	0.53	5.48	0.43	1.00	0.39
19	6.66	0.27	5.48	0.19	0.80	0.06
20	6.74	0.38	4.45	0.31	0.01	0.24

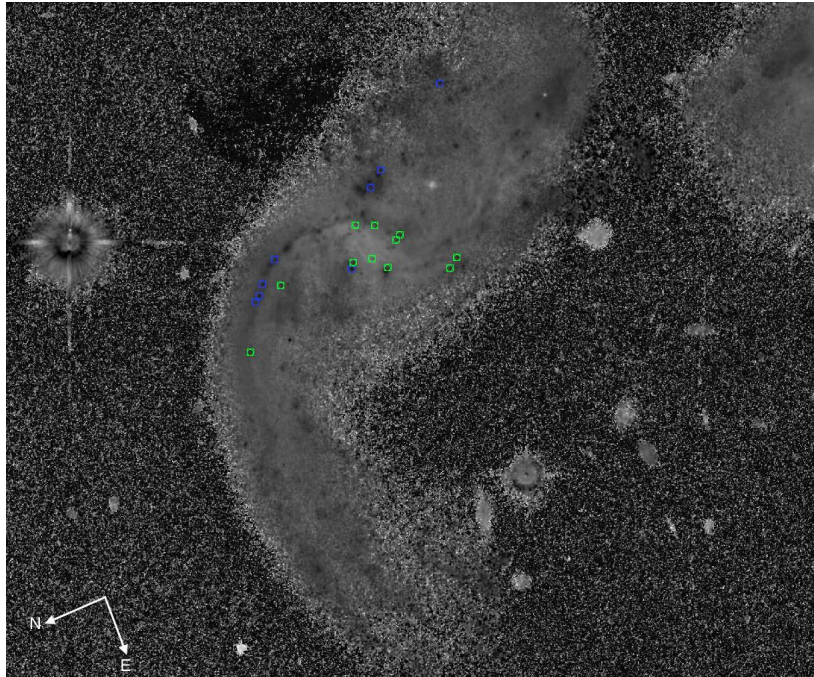


FIG. 11.— Inverted black and white B-I image of Arp 256N taken with HST ACS/WFC F814W and F435W. The bright emission corresponds to redder (i.e. dustier) regions of the galaxy. The blue centroids correspond to clusters found in relatively “dust-free” regions of these galaxies, whereas the green centroids correspond to clusters found in relatively dustier regions of the galaxy.

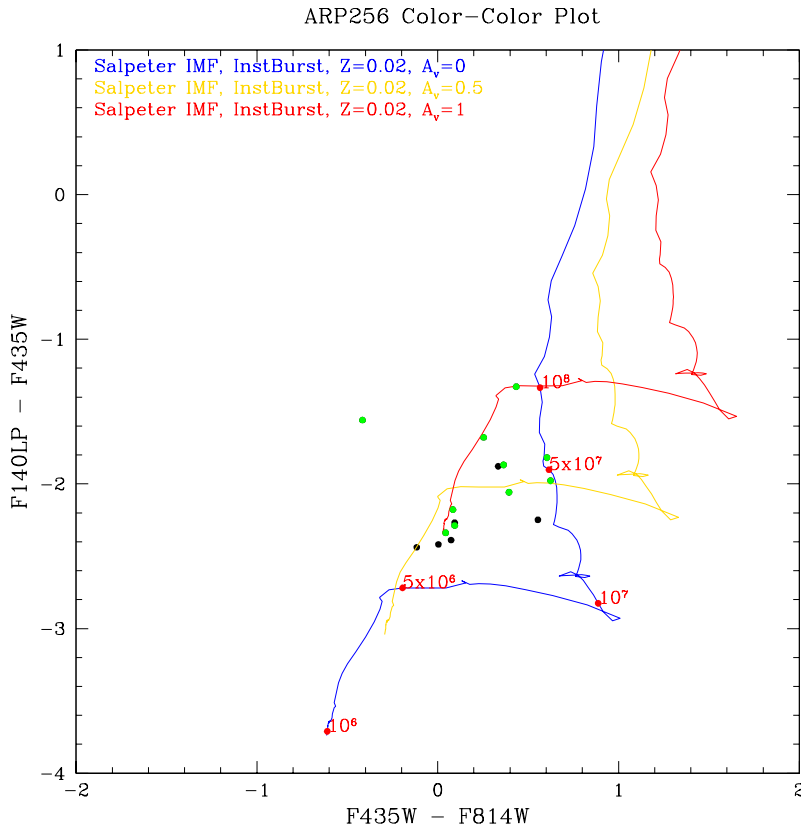


FIG. 12.— Color-Color plot of all star clusters identified in Arp 256N in F814W, F435W, and F140LP plotted against SSP models with various amount of visual extinction. The green points correspond to the clusters found in dustier regions of the galaxy in Figure 11

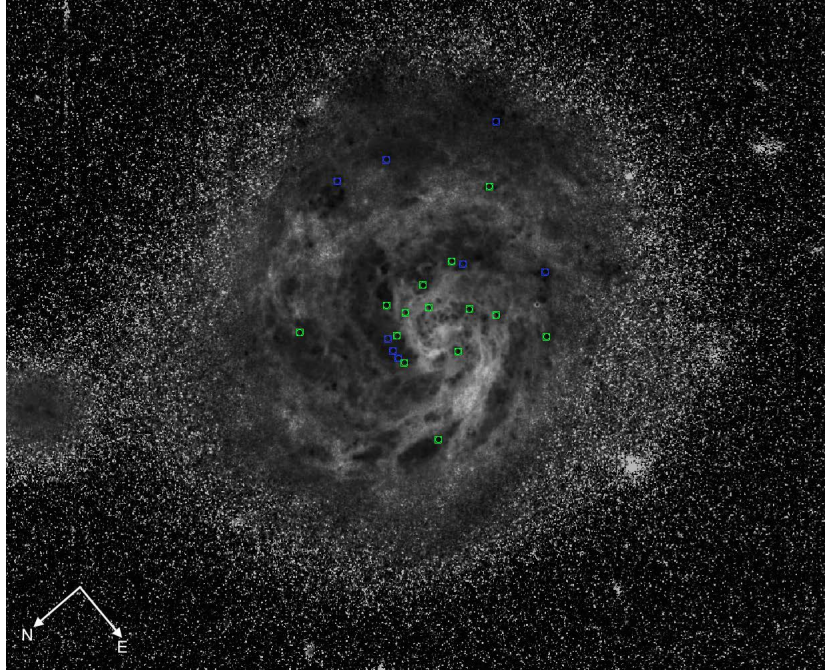


FIG. 13.— Inverted black and white B-I image of NGC 0695 taken with HST ACS/WFC F814W and F435W. The bright emission corresponds to redder (i.e. dustier) regions of the galaxy. The blue centroids correspond to clusters found in relatively “dust-free” regions of these galaxies, whereas the green centroids correspond to clusters found in relatively dustier regions of the galaxy.

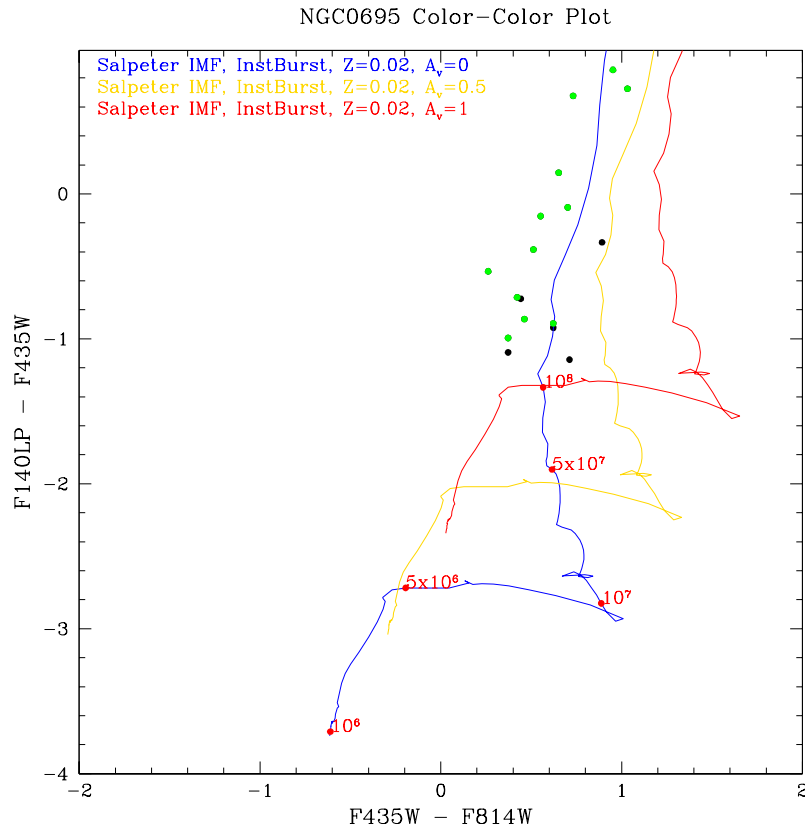


FIG. 14.— Color-Color plot of all star clusters identified in NGC 0695 in F814W, F435W, and F140LP plotted against SSP models with various amount of visual extinction. The green points correspond to the clusters found in dustier regions of the galaxy in Figure 13

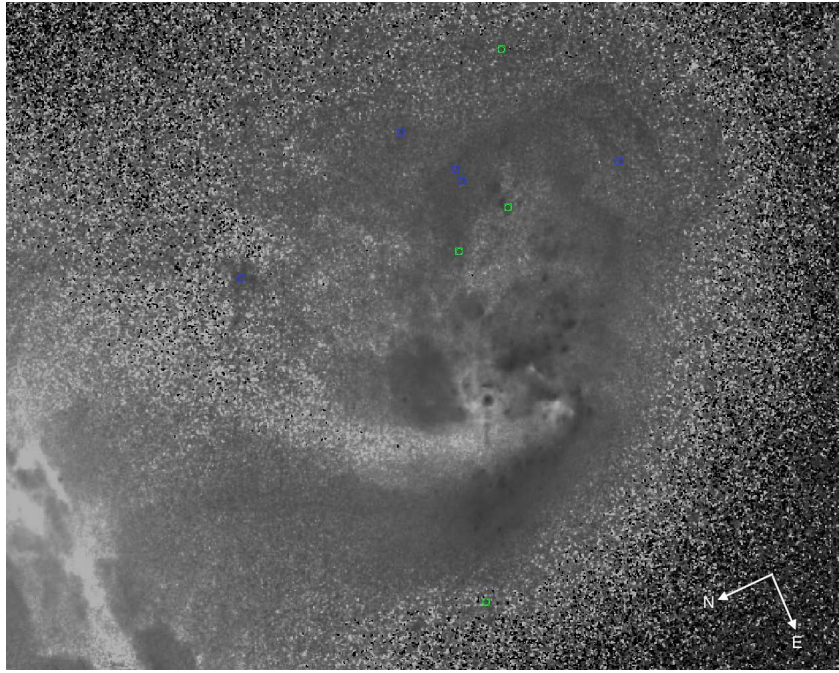


FIG. 15.— Inverted black and white B-I image of UGC 02369 taken with HST ACS/WFC F814W and F435W. The bright emission corresponds to redder (i.e. dustier) regions of the galaxy. The blue centroids correspond to clusters found in relatively “dust-free” regions of these galaxies, whereas the green centroids correspond to clusters found in relatively dustier regions of the galaxy.

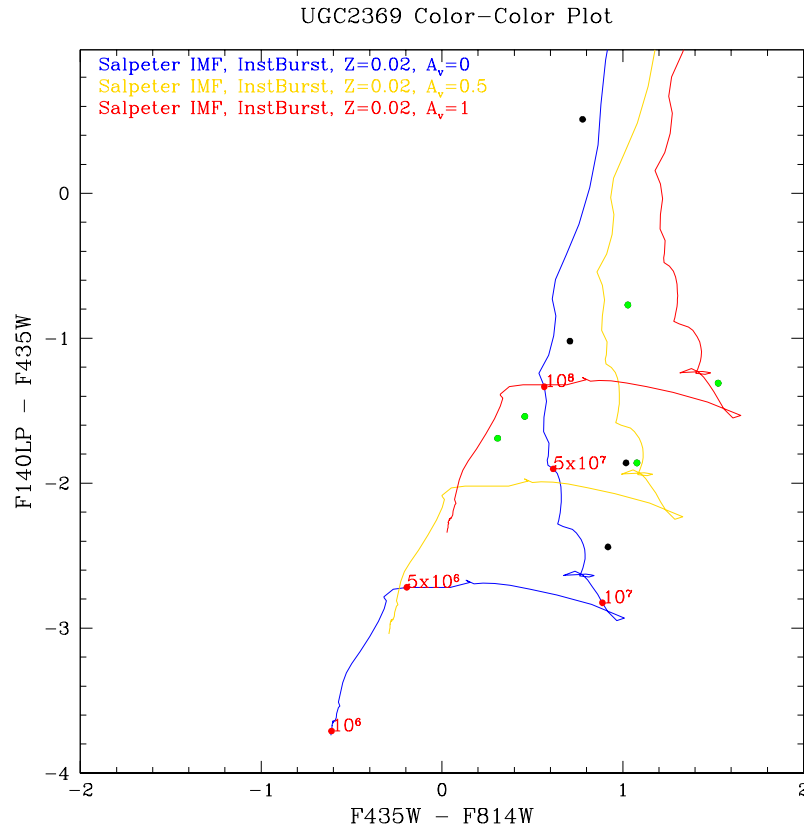


FIG. 16.— Color-Color plot of all star clusters identified in UGC 02369 in F814W, F435W, and F140LP plotted against SSP models with various amount of visual extinction. The green points correspond to the clusters found in dustier regions of the galaxy in Figure 15

TABLE 7
OBSERVED PROPERTIES OF STAR CLUSTERS IN ARP 256N

ID	RA	Dec	M_B	σ_B	M_I	σ_I	M_{FUV}	σ_{FUV}
1	4.705283874	-10.36593186	-10.52	0.03	-10.40	0.07	-12.96	0.03
2	4.706681456	-10.36309635	-11.05	0.02	-11.05	0.08	-13.47	0.03
3	4.706997794	-10.36259164	-12.33	0.02	-12.88	0.02	-14.58	0.04
4	4.708060796	-10.36212902	-11.79	0.03	-12.41	0.04	-13.77	0.02
5	4.707757416	-10.3616235	-11.16	0.06	-10.74	0.22	-12.72	0.06
6	4.708684462	-10.36263369	-12.69	0.01	-13.05	0.02	-14.56	0.01
7	4.708763384	-10.36246337	-11.99	0.02	-12.38	0.03	-14.05	0.03
8	4.710151015	-10.36378048	-11.10	0.03	-11.14	0.06	-13.44	0.03
9	4.708704027	-10.36100592	-12.08	0.05	-12.17	0.03	-14.37	0.04
10	4.709365918	-10.361838	-12.00	0.04	-12.08	0.13	-14.18	0.03
11	4.708851609	-10.3608711	-13.78	0.01	-13.85	0.02	-16.17	0.01
12	4.710324609	-10.36344198	-11.80	0.02	-12.23	0.02	-13.13	0.06
13	4.707903866	-10.35832277	-13.74	0.01	-14.07	0.02	-15.62	0.01
14	4.708214025	-10.3587839	-11.98	0.02	-12.23	0.04	-13.66	0.02
15	4.708155895	-10.358066	-13.40	0.01	-13.49	0.02	-15.67	0.01
16	4.709517938	-10.35699562	-11.91	0.02	-12.51	0.03	-13.73	0.02

TABLE 8
DERIVED PROPERTIES OF STAR CLUSTERS IN ARP 256N

ID	Log(Age)	σ_{Age}	Log(M/M_\odot)	σ_M	A_V	σ_{A_V}
1	6.54	0.08	4.77	0.22	0.70	0.13
2	6.66	0.19	5.00	0.30	0.60	0.23
3	7.42	0.21	5.84	0.21	0.10	0.11
4	7.32	0.25	5.73	0.25	0.40	0.17
5	6.52	0.01	5.29	0.21	1.20	0.10
6	7.76	0.53	5.68	0.47	0.01	0.44
7	7.63	0.45	5.34	0.36	0.01	0.31
8	6.64	0.11	5.07	0.26	0.70	0.19
9	6.66	0.27	5.47	0.29	0.70	0.22
10	6.44	0.16	5.70	0.28	1.10	0.21
11	6.68	0.26	6.09	0.24	0.60	0.15
12	6.44	0.41	5.94	0.45	1.70	0.42
13	6.72	0.49	6.16	0.42	0.80	0.39
14	6.48	0.07	5.79	0.22	1.40	0.12
15	5.70	0.44	6.52	0.29	1.10	0.23
16	6.76	0.33	5.36	0.30	0.70	0.24

TABLE 9
OBSERVED PROPERTIES OF STAR CLUSTERS IN NGC 0695

ID	RA	Dec	M_B	σ_B	M_I	σ_I	M_{FUV}	σ_{FUV}
1	27.80620232	22.58288641	-11.35	0.06	-12.24	0.06	-11.68	0.08
2	27.8065178	22.57996324	-11.21	0.02	-11.65	0.03	-11.93	0.06
3	27.80625132	22.58196385	-10.37	0.04	-10.99	0.04	-11.29	0.11
4	27.80849949	22.58172092	-10.96	0.10	-11.58	0.10	-11.85	0.06
5	27.80866289	22.58234757	-13.19	0.02	-13.45	0.04	-13.72	0.02
6	27.808703	22.58307422	-12.36	0.05	-12.82	0.06	-13.22	0.02
7	27.80909168	22.58243561	-12.16	0.02	-12.89	0.06	-11.48	0.10
8	27.80945496	22.58181348	-12.71	0.03	-13.26	0.05	-12.86	0.03
9	27.80898694	22.58283593	-12.19	0.03	-13.14	0.04	-11.33	0.03
10	27.8097772	22.58144334	-13.05	0.01	-13.70	0.01	-12.90	0.02
11	27.80843983	22.58463146	-10.70	0.07	-11.21	0.08	-11.08	0.14
12	27.80929961	22.58314413	-12.17	0.03	-12.87	0.06	-12.26	0.04
13	27.8105601	22.5808227	-10.89	0.02	-11.31	0.03	-11.60	0.05
14	27.80927543	22.58330795	-10.97	0.06	-11.34	0.09	-12.06	0.05
15	27.80952221	22.58331847	-11.14	0.05	-11.85	0.13	-12.28	0.04
16	27.81139357	22.58329741	-11.56	0.02	-11.93	0.04	-12.55	0.03
17	27.80755568	22.58055984	-12.43	0.02	-13.46	0.04	-11.70	0.07

NGC 1614

NGC 1614 is a late-stage merger with two resolved components in the nucleus separated by $\sim 0.8''$ (300 pc). Beyond the nucleus are two well defined spiral arms, with a significant number of bright clusters scattered throughout this region. The maximum A_V adopted for this galaxy is 4.0 mags of visual extinction (Alonso-Herrero et al. 2001).

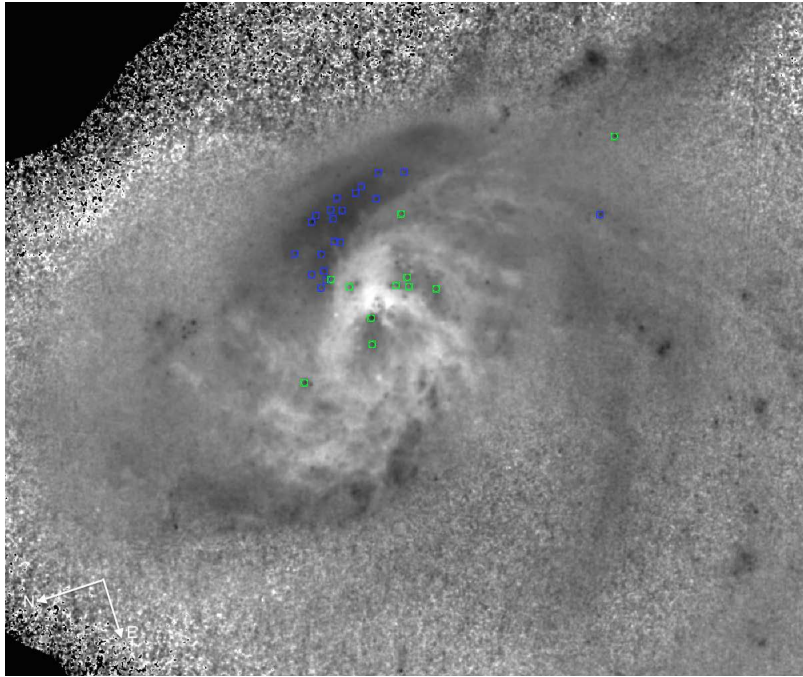


FIG. 17.— Inverted black and white B-I image of NGC 1614 taken with HST ACS/WFC F814W and F435W. The bright emission corresponds to redder (i.e. dustier) regions of the galaxy. The blue centroids correspond to clusters found in relatively “dust-free” regions of these galaxies, whereas the green centroids correspond to clusters found in relatively dustier regions of the galaxy.

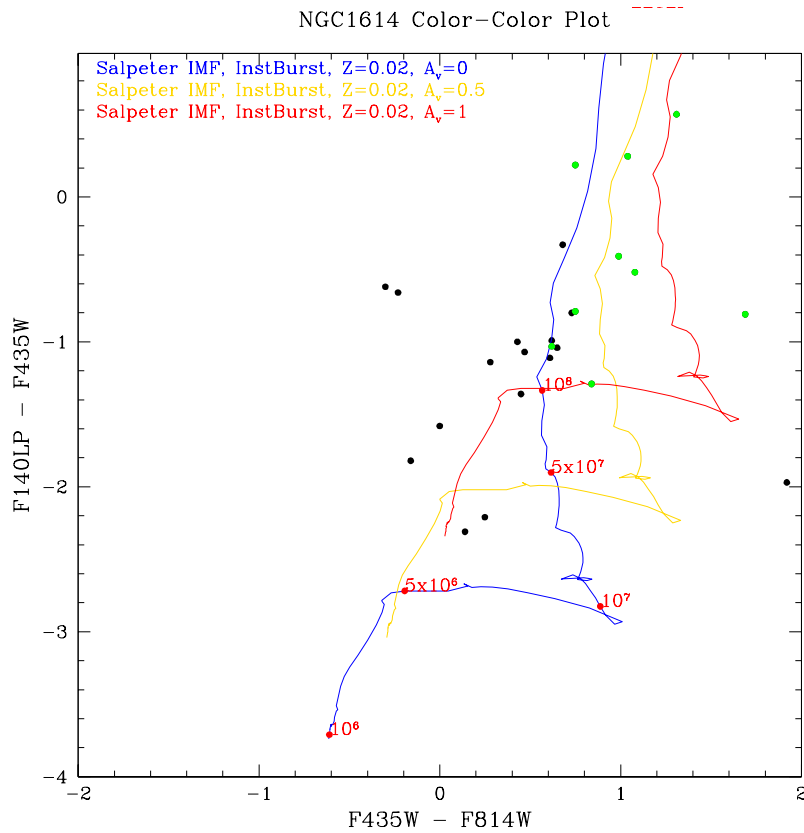


FIG. 18.— Color-Color plot of all star clusters identified in NGC 1614 in F814W, F435W, and F140LP plotted against SSP models with various amount of visual extinction. The green points correspond to the clusters found in dustier regions of the galaxy in Figure 17

TABLE 10
DERIVED PROPERTIES OF STAR CLUSTERS IN NGC 0695

ID	Log(Age)	σ_{Age}	Log(M/M_{\odot})	σ_M	A_V	σ_{A_V}
1	6.70	0.92	6.22	0.76	1.70	0.84
2	6.66	0.82	5.99	0.66	1.40	0.70
3	6.40	0.74	6.05	0.71	1.90	0.76
4	6.70	0.86	5.85	0.63	1.30	0.65
5	6.66	0.40	6.84	0.17	1.50	0.42
6	6.68	0.24	6.40	0.31	1.30	0.25
7	8.56	0.86	7.14	0.17	0.01	0.02
8	8.41	0.01	7.23	0.18	0.01	0.03
9	8.56	0.03	7.26	0.21	0.20	0.10
10	8.46	0.48	7.40	0.17	0.01	0.02
11	8.36	0.52	6.39	0.50	0.01	0.48
12	8.41	0.04	7.07	0.20	0.10	0.10
13	6.66	0.76	5.86	0.64	1.40	0.67
14	6.66	0.40	5.79	0.28	1.20	0.21
15	6.74	0.90	5.83	0.59	1.10	0.61
16	6.66	0.49	6.03	0.18	1.20	0.05
17	8.51	0.04	7.36	0.22	0.30	0.13

TABLE 11
OBSERVED PROPERTIES OF STAR CLUSTERS IN UGC 02369

ID	RA	Dec	M_B	σ_B	M_I	σ_I	M_{FUV}	σ_{FUV}
1	43.50963156	14.97660266	-10.85	0.06	-11.31	0.13	-12.39	0.02
2	43.50342276	14.96966218	-9.69	0.10	-10.01	0.15	-11.38	0.05
3	43.5048427	14.97058419	-9.36	0.12	-10.28	0.14	-11.80	0.04
4	43.50519206	14.96870793	-9.54	0.10	-10.56	0.09	-11.40	0.05
5	43.50404048	14.97111855	-12.20	0.01	-12.98	0.01	-11.69	0.04
6	43.50533035	14.97014987	-9.73	0.17	-11.26	0.10	-11.04	0.05
7	43.50518643	14.9734774	-9.84	0.10	-10.55	0.13	-10.86	0.11
8	43.50567241	14.97086958	-9.81	0.11	-10.84	0.10	-10.58	0.11
9	43.50995014	14.97180788	-10.08	0.07	-11.16	0.06	-11.94	0.03

TABLE 12
DERIVED PROPERTIES OF STAR CLUSTERS IN UGC 02369

ID	Log(Age)	σ_{Age}	Log(M/M_{\odot})	σ_M	A_V	σ_{A_V}
1	5.10	0.77	5.68	0.52	1.60	0.50
2	6.36	0.58	4.99	0.45	1.40	0.40
3	7.04	0.20	4.47	0.26	0.20	0.15
4	7.63	0.26	4.93	0.26	0.10	0.17
5	6.66	0.03	6.20	0.17	2.20	0.05
6	6.92	0.21	4.98	0.31	1.10	0.19
7	6.72	0.74	4.74	0.59	1.20	0.59
8	7.81	0.55	5.46	0.51	0.70	0.49
9	7.34	0.18	5.22	0.23	0.50	0.12

2MASX J06094582-2140234

2MASX J06094582-2140234 is a mid-stage merger consisting of two face-on galaxies which appear to overlap and have a projected separation of $\sim 8.4''$ (6.3 kpc). Prominent rings/arms in each galaxy contain the bulk of the visible star clusters. The maximum A_V adopted for this galaxy is 1.0 mags of visual extinction (Miralles-Caballero et al. 2012).

2MASX J08370182-4954302

2MASX J08370182-4954302 is a mid-stage merger containing two nuclei separated by $\sim 0.66''$ (0.36 kpc). Surrounding the nuclei are multiple bright star clusters in a spiral ridge just northwest and west of the nuclei. The maximum A_V adopted for this galaxy is 3.7 mags of visual extinction (Rich et al. 2012).

NGC 2623

Evans et al. (2008) discusses the detailed morphology of this galaxy at length. NGC 2623 is a late-stage merger with dust lanes running along its tidal tails into the nucleus. Several bright clusters are distributed throughout the bulge and in a 'pie-wedge' concentration south of the nucleus. The maximum A_V adopted for this galaxy is 1.9 mags of visual extinction (Privon et al. 2013).

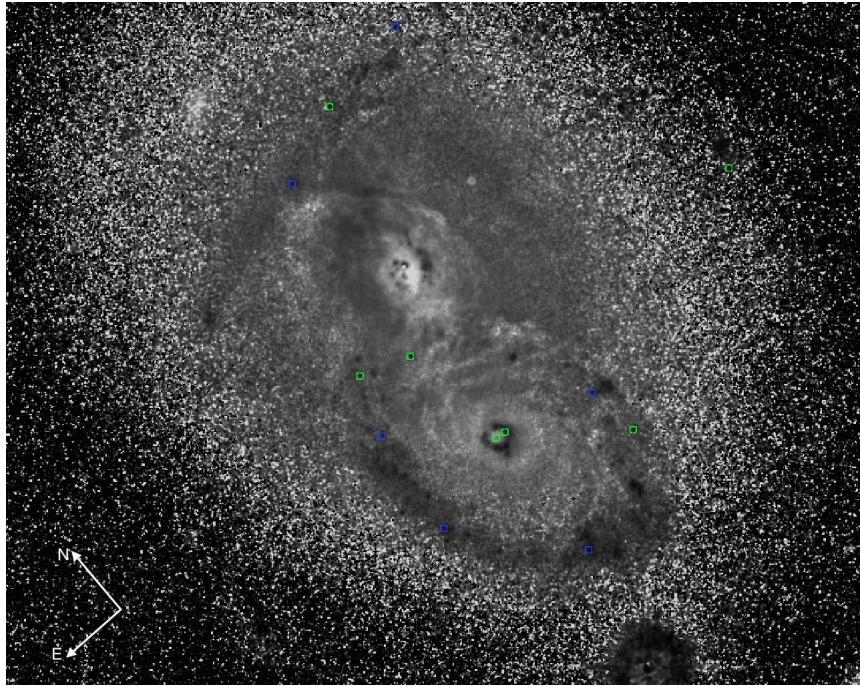


FIG. 19.— Inverted black and white B-I image of 2MASX J06094582-2140234 taken with HST ACS/WFC F814W and F435W. The bright emission corresponds to redder (i.e. dustier) regions of the galaxy. The blue centroids correspond to clusters found in relatively “dust-free” regions of these galaxies, whereas the green centroids correspond to clusters found in relatively dustier regions of the galaxy.

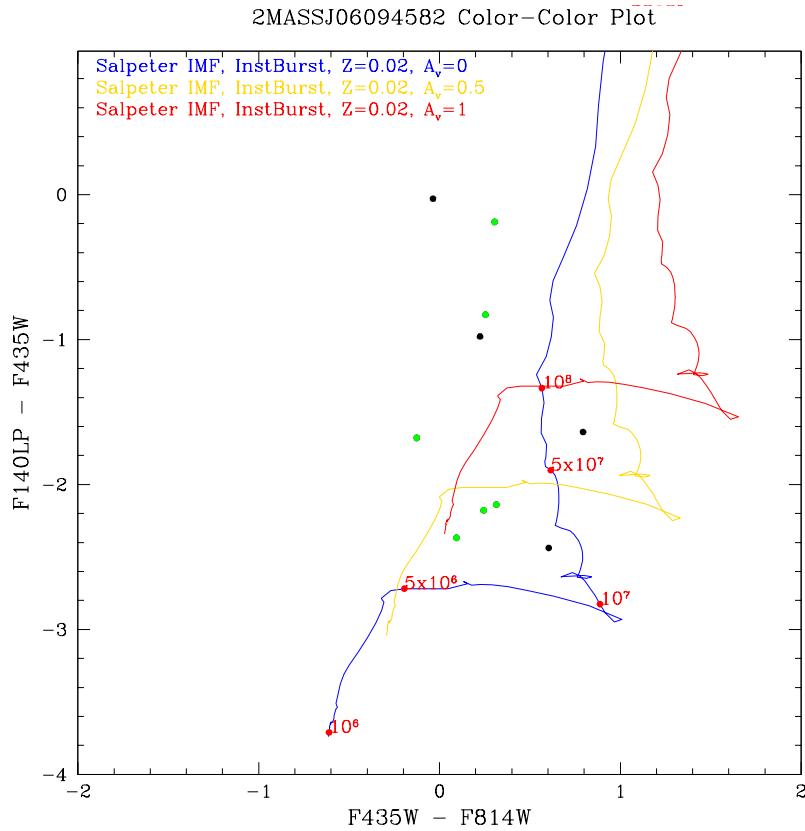


FIG. 20.— Color-Color plot of all star clusters identified in 2MASX J06094582-2140234 in F814W, F435W, and F140LP plotted against SSP models with various amount of visual extinction. The green points correspond to the clusters found in dustier regions of the galaxy in Figure 19

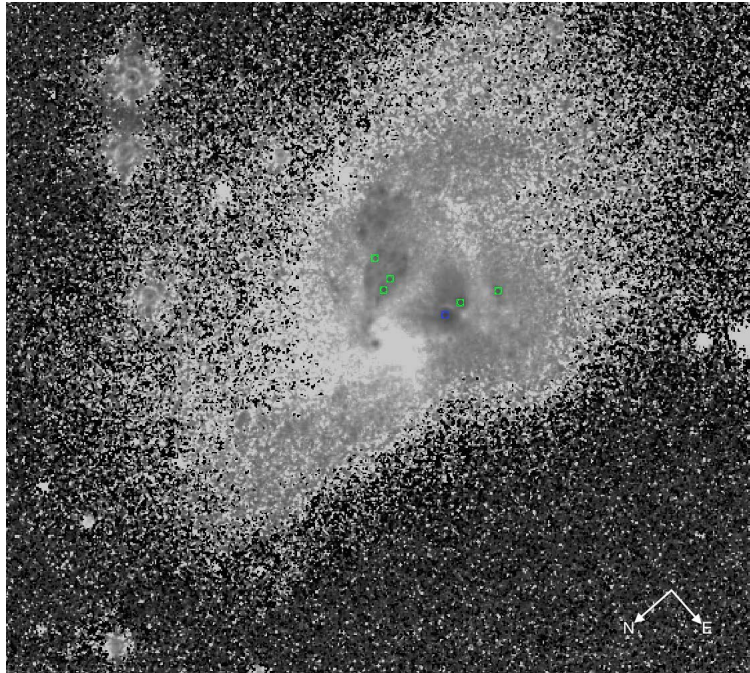


FIG. 21.— Inverted black and white B-I image of 2MASX J08370182-4954302 taken with HST ACS/WFC F814W and F435W. The bright emission corresponds to redder (i.e. dustier) regions of the galaxy. The blue centroids correspond to clusters found in relatively “dust-free” regions of these galaxies, whereas the green centroids correspond to clusters found in relatively dustier regions of the galaxy.

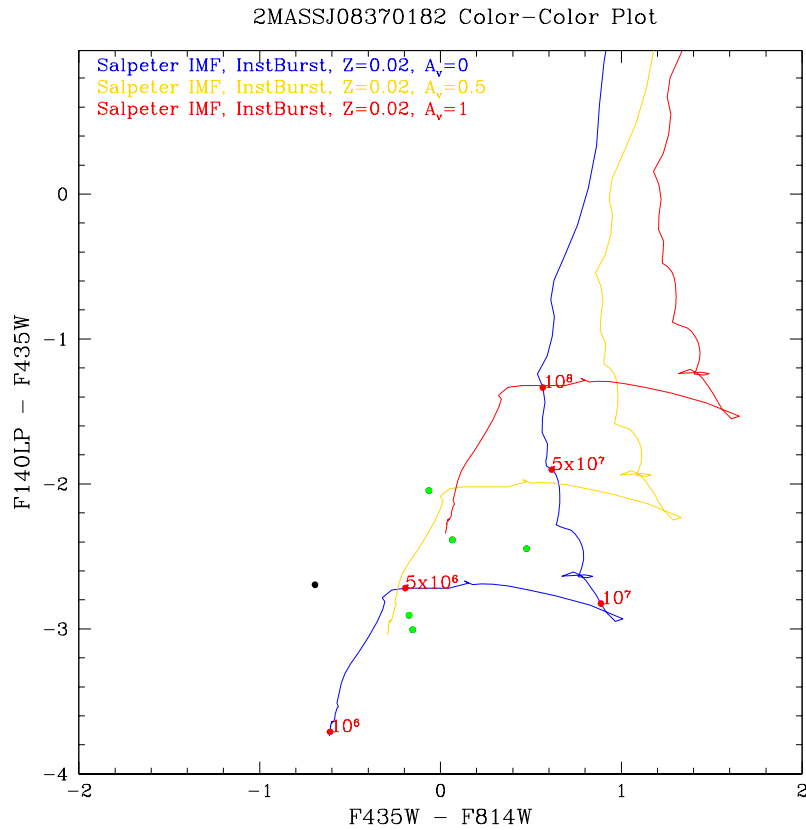


FIG. 22.— Color-Color plot of all star clusters identified in 2MASX J08370182-4954302 in F814W, F435W, and F140LP plotted against SSP models with various amount of visual extinction. The green points correspond to the clusters found in dustier regions of the galaxy in Figure 21

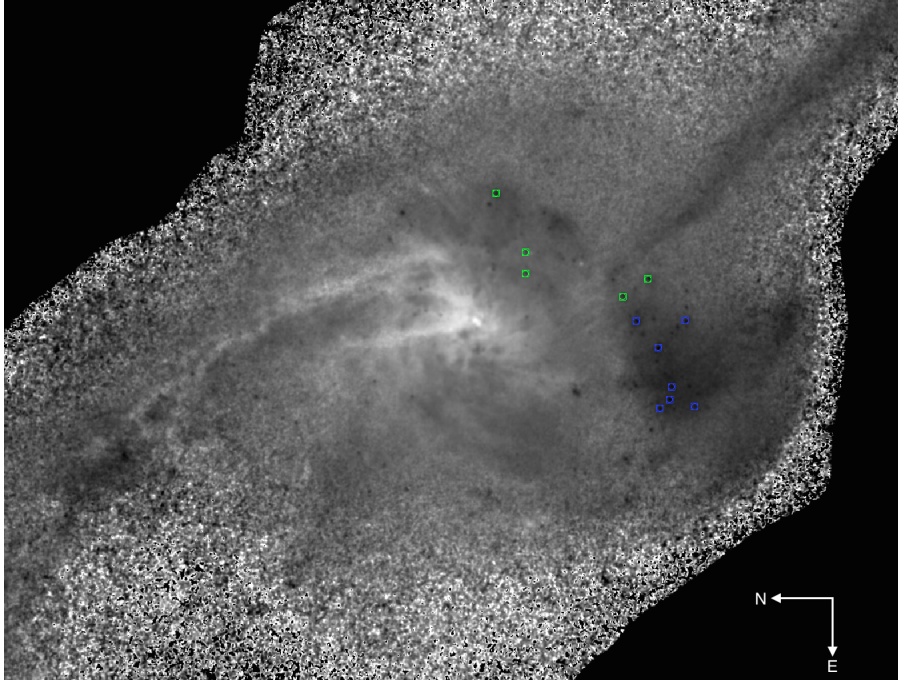


FIG. 23.— Inverted black and white B-I image taken of NGC 2623 with HST ACS/WFC F814W and F435W. The bright emission corresponds to redder (i.e. dustier) regions of the galaxy. The blue centroids correspond to clusters found in relatively “dust-free” regions of these galaxies, whereas the green centroids correspond to clusters found in relatively dustier regions of the galaxy.

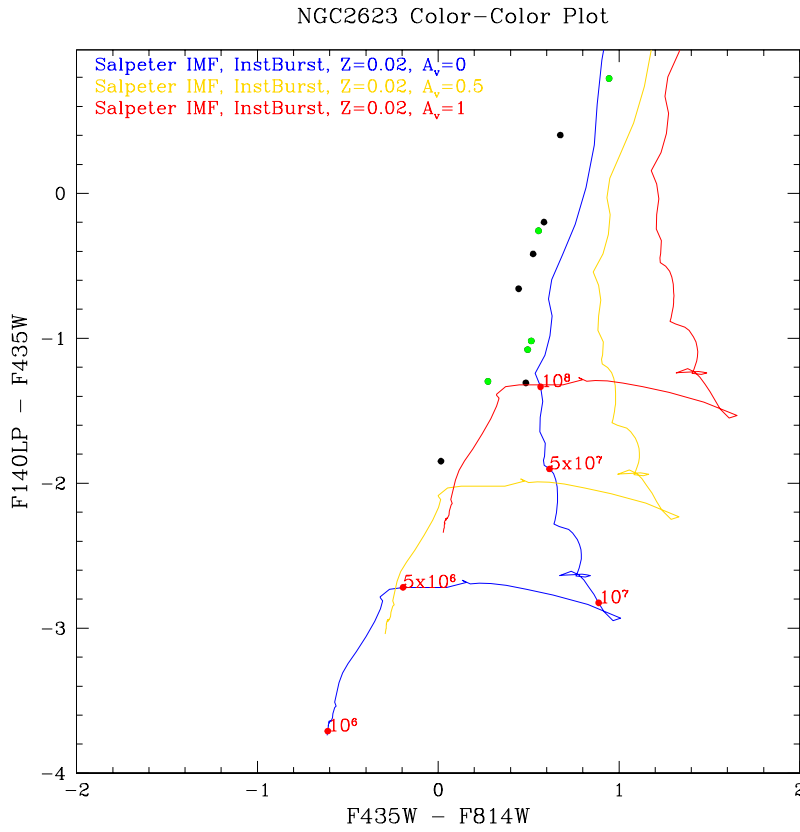


FIG. 24.— Color-Color plot of all star clusters identified in NGC 2623 in F814W, F435W, and F140LP plotted against SSP models with various amount of visual extinction. The green points correspond to the clusters found in dustier regions of the galaxy in Figure 23

TABLE 13
OBSERVED PROPERTIES OF STAR CLUSTERS IN NGC 1614

ID	RA	Dec	M_B	σ_B	M_I	σ_I	M_{FUV}	σ_{FUV}
1	68.49833746	-8.5836658	-11.21	0.01	-11.83	0.01	-12.24	0.01
2	68.49787214	-8.579994493	-11.99	0.01	-12.46	0.02	-13.06	0.04
3	68.49775125	-8.5795586	-12.48	0.02	-13.13	0.02	-13.52	0.02
4	68.49797702	-8.579081625	-13.73	0.01	-14.18	0.01	-15.09	0.02
5	68.49796061	-8.578745709	-12.92	0.01	-13.53	0.02	-14.03	0.03
6	68.49813488	-8.578589371	-11.62	0.05	-11.90	0.10	-12.76	0.09
7	68.49855752	-8.57973638	-11.62	0.02	-12.37	0.02	-12.41	0.06
8	68.49957784	-8.583032955	-10.67	0.02	-10.81	0.03	-12.98	0.04
9	68.49815445	-8.578312212	-13.05	0.02	-13.48	0.03	-14.05	0.03
10	68.49829417	-8.578581	-11.86	0.09	-11.86	0.17	-13.44	0.13
11	68.49823898	-8.578206022	-12.72	0.03	-12.49	0.06	-13.38	0.08
12	68.49868598	-8.578484509	-15.33	0.01	-16.06	0.01	-16.13	0.01
13	68.49872601	-8.578589212	-12.07	0.10	-11.77	0.11	-12.69	0.16
14	68.49882795	-8.578206944	-13.22	0.02	-13.47	0.03	-15.43	0.02
15	68.4986906	-8.577771465	-12.76	0.01	-13.38	0.01	-13.75	0.02
16	68.49912105	-8.578165885	-12.53	0.05	-12.37	0.08	-14.35	0.03
17	68.49965474	-8.579516099	-14.21	0.01	-15.25	0.01	-13.93	0.02
18	68.49930324	-8.57824455	-12.07	0.06	-13.76	0.03	-12.88	0.08
19	68.49929236	-8.578158424	-10.73	0.21	-12.65	0.10	-12.70	0.15
20	68.49973941	-8.579291182	-12.81	0.04	-13.80	0.03	-13.22	0.03
21	68.49982001	-8.579497527	-11.54	0.11	-12.38	0.07	-12.83	0.05
22	68.49952214	-8.578509292	-13.29	0.01	-14.60	0.02	-12.72	0.05
23	68.49939493	-8.578038288	-12.50	0.02	-13.18	0.02	-12.83	0.09
24	68.49998928	-8.579944805	-12.74	0.02	-13.82	0.03	-13.26	0.03
25	68.50060521	-8.578602704	-13.65	0.01	-14.40	0.02	-13.43	0.03

TABLE 14
DERIVED PROPERTIES OF STAR CLUSTERS IN NGC 1614

ID	Log(Age)	σ_{Age}	Log(M/M_\odot)	σ_M	A_V	σ_{A_V}
1	6.70	0.22	5.53	0.28	1.50	0.22
2	6.52	0.02	5.89	0.18	1.70	0.06
3	6.66	0.73	6.10	0.66	1.60	0.70
4	6.42	0.48	6.75	0.51	1.70	0.49
5	6.68	0.71	6.22	0.61	1.50	0.63
6	6.52	0.32	5.68	0.39	1.60	0.35
7	6.64	0.84	5.86	0.72	1.80	0.79
8	6.72	0.16	4.77	0.23	0.50	0.15
9	6.52	0.01	6.31	0.17	1.70	0.04
10	6.52	0.19	5.62	0.31	1.30	0.24
11	6.52	0.72	6.18	0.65	1.70	0.69
12	6.64	0.81	7.34	0.76	1.80	0.85
13	6.52	0.91	5.97	0.75	1.80	0.82
14	6.74	0.07	5.78	0.18	0.50	0.06
15	6.36	0.10	6.59	0.22	2.00	0.13
16	6.52	0.01	5.78	0.19	1.10	0.06
17	8.46	0.02	7.40	0.17	0.40	0.04
18	6.82	0.01	5.86	0.20	1.40	0.08
19	7.65	0.77	5.30	0.34	0.01	0.20
20	7.86	0.55	6.73	0.55	0.90	0.55
21	7.59	0.40	5.91	0.42	0.60	0.37
22	6.52	0.66	7.04	0.68	2.90	0.73
23	6.52	0.04	6.35	0.17	2.20	0.57
24	7.72	0.35	6.68	0.31	1.00	0.25
25	8.61	0.02	7.15	0.17	0.10	0.05

UGC 04881

UGC 04881 is an early-stage merger containing two nuclei separated by $\sim 11''$ (9 kpc). Spiral dust lanes and strings of star clusters surround the NE nucleus. In the SW nucleus a linear distribution of star clusters and a prominent dust lane are seen. The maximum A_V adopted for this galaxy is 1.9 mags of visual extinction (Gonzalez-Martin et al. 2009).

IC 2545

IC 2545 is a late-stage merger being viewed face-on. Dust lanes and strings of star clusters extend from two unresolved nuclei separated by $\sim 0.8''$ (0.54 kpc) in the center of the galaxy. Multiple star clusters are also visible throughout the tidal tails. The maximum A_V adopted for this galaxy is 4.0 mags of visual extinction (van den Broek et al. 1991).

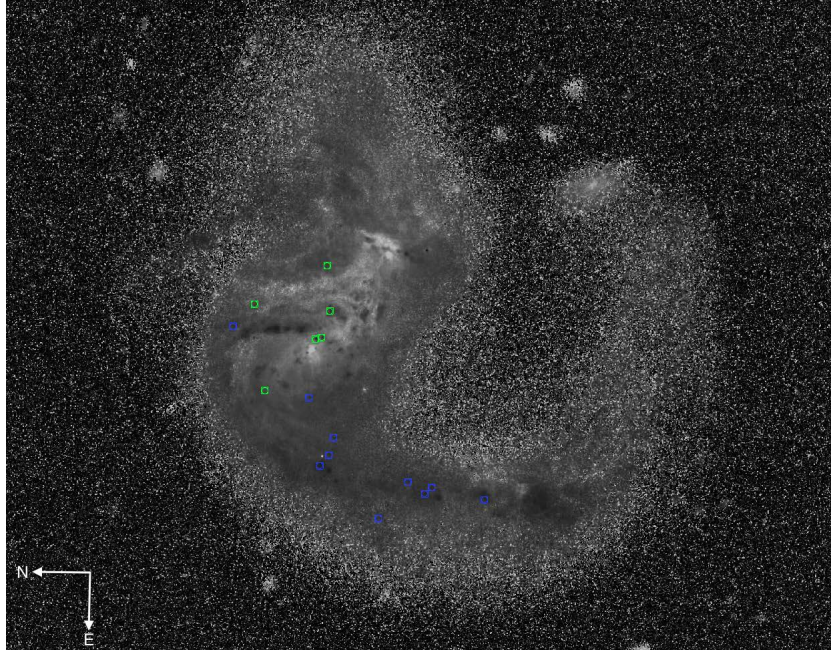


FIG. 25.— Inverted black and white B-I image of UGC 04881 taken with HST ACS/WFC F814W and F435W. The bright emission corresponds to redder (i.e. dustier) regions of the galaxy. The blue centroids correspond to clusters found in relatively “dust-free” regions of these galaxies, whereas the green centroids correspond to clusters found in relatively dustier regions of the galaxy.

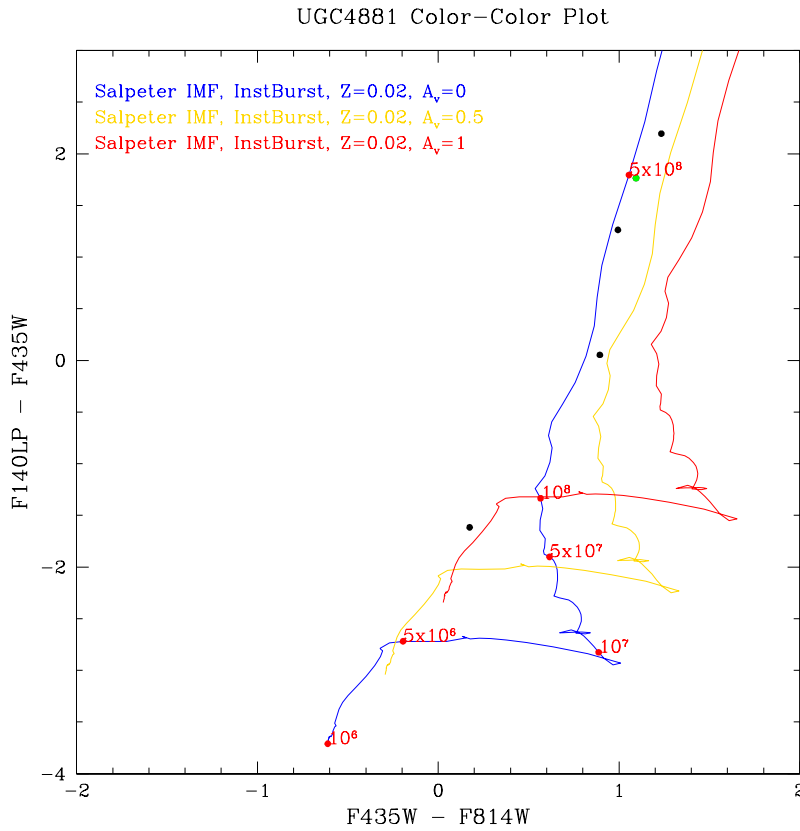


FIG. 26.— Color-Color plot of all star clusters identified in UGC 04881 in F814W, F435W, and F140LP plotted against SSP models with various amount of visual extinction. The green points correspond to the clusters found in dustier regions of the galaxy in Figure 25

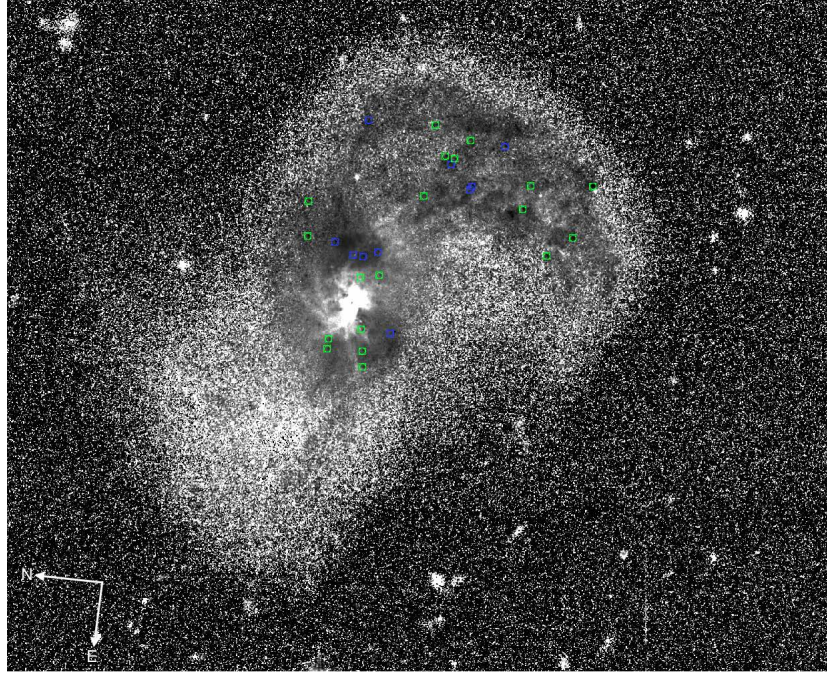


FIG. 27.— Inverted black and white B-I image of IC 2545 taken with HST ACS/WFC F814W and F435W. The bright emission corresponds to redder (i.e. dustier) regions of the galaxy. The blue centroids correspond to clusters found in relatively “dust-free” regions of these galaxies, whereas the green centroids correspond to clusters found in relatively dustier regions of the galaxy.

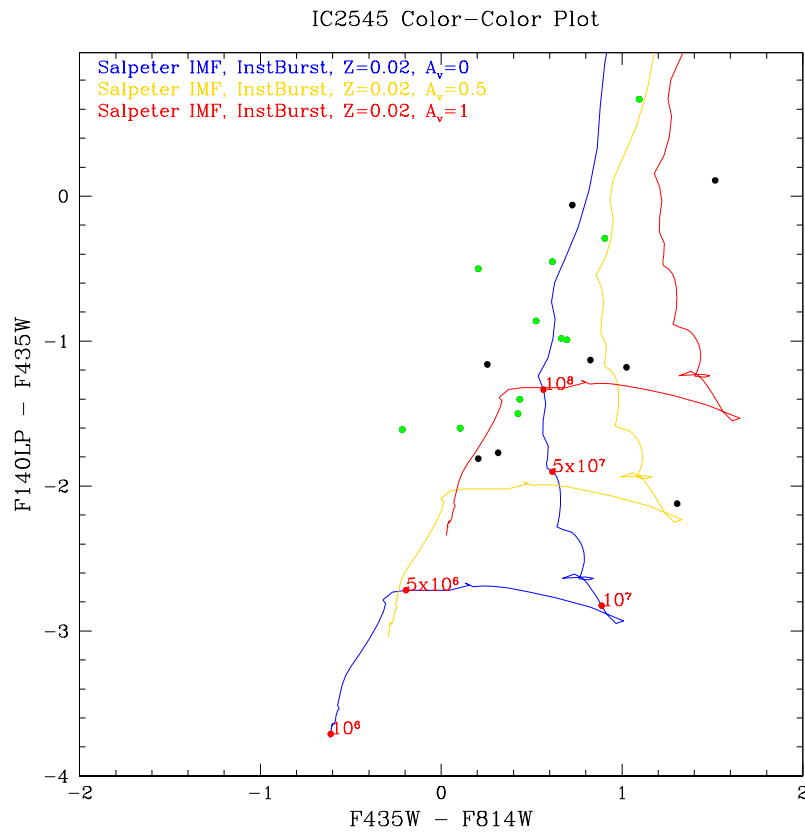


FIG. 28.— Color-Color plot of all star clusters identified in IC 2545 in F814W, F435W, and F140LP plotted against SSP models with various amount of visual extinction. The green points correspond to the clusters found in dustier regions of the galaxy in Figure 27

TABLE 15
OBSERVED PROPERTIES OF STAR CLUSTERS IN 2MASX J06094582-2140234

ID	RA	Dec	M_B	σ_B	M_I	σ_I	M_{FUV}	σ_{FUV}
1	92.438548	-21.67128502	-10.07	0.09	-10.29	0.14	-11.05	0.04
2	92.43987859	-21.67130163	-10.68	0.06	-10.77	0.10	-13.05	0.01
3	92.43715675	-21.67545341	-11.44	0.02	-11.68	0.04	-13.62	0.02
4	92.4409611	-21.6715528	-11.60	0.03	-12.20	0.05	-14.04	0.05
5	92.4416782	-21.67398257	-12.05	0.03	-11.92	0.12	-13.73	0.02
6	92.44229618	-21.67366993	-10.76	0.07	-11.07	0.15	-12.90	0.01
7	92.44270943	-21.67433539	-10.88	0.06	-10.84	0.18	-10.91	0.03
8	92.44164311	-21.67543932	-14.49	0.03	-14.79	0.09	-14.68	0.05
9	92.44054901	-21.67659996	-10.76	0.05	-11.01	0.10	-11.59	0.04
10	92.44310457	-21.67562528	-11.02	0.07	-11.81	0.07	-12.66	0.01

TABLE 16
DERIVED PROPERTIES OF STAR CLUSTERS IN 2MASX
J06094582-2140234

ID	Log(Age)	σ_{Age}	Log(M/M_\odot)	σ_M	A_V	σ_{A_V}
1	6.74	0.09	4.79	0.20	1.00	0.08
2	6.72	0.29	4.78	0.30	0.50	0.24
3	6.74	0.03	5.07	0.19	0.50	0.09
4	6.92	0.05	5.14	0.17	0.20	0.04
5	6.70	0.08	5.55	0.17	0.90	0.05
6	6.74	0.36	4.85	0.35	0.60	0.30
7	7.91	0.03	6.04	0.17	1.00	0.29
8	7.91	0.03	7.48	0.16	1.00	0.20
9	7.16	0.09	5.52	0.18	1.00	0.07
10	7.36	0.31	5.55	0.28	0.60	0.21

TABLE 17
OBSERVED PROPERTIES OF STAR CLUSTERS IN 2MASX J08370182-4954302

ID	RA	Dec	M_B	σ_B	M_I	σ_I	M_{FUV}	σ_{FUV}
1	129.2557186	-49.90846967	-14.83	0.04	-15.31	0.03	-17.28	0.01
2	129.2561197	-49.90840169	-15.24	0.05	-15.31	0.03	-17.63	0.16
3	129.2561534	-49.90828131	-15.85	0.02	-15.68	0.02	-18.76	0.02
4	129.2574869	-49.90904604	-15.42	0.01	-15.36	0.02	-17.47	0.01
5	129.2571648	-49.90869922	-18.38	0.01	-18.23	0.01	-21.39	0.01
6	129.2571314	-49.90851337	-19.79	0.01	-19.10	0.01	-22.49	0.01

TABLE 18
DERIVED PROPERTIES OF STAR CLUSTERS IN 2MASX
J08370182-4954302

ID	Log(Age)	σ_{Age}	Log(M/M_\odot)	σ_M	A_V	σ_{A_V}
1	6.86	0.02	6.38	0.18	0.20	0.05
2	5.10	0.64	7.12	0.43	1.00	0.40
3	5.10	0.46	7.15	0.17	0.60	0.02
4	6.66	0.03	6.59	0.16	0.50	0.04
5	5.10	0.41	8.17	0.17	0.60	0.04
6	6.66	0.61	8.07	0.16	0.01	0.24

NGC 3256

NGC 3256 is a late-stage merger containing a large number of star clusters along the inner ($\sim 20''$, or 4 kpc) spiral structure of the nuclear region. The spiral dust lanes extending from the nucleus give this galaxy pockets of high and low extinction. The maximum A_V adopted for this galaxy is 3.3 mags of visual extinction (Rich et al. 2012).

Arp 148

Arp 148 is an early-stage merger and the only example of a ring galaxy in the sample. This $\sim 23''$ (16 kpc) diameter galaxy is comprised of clumps of star clusters along its perimeter, and throughout much of its interior. The maximum A_V adopted for this galaxy is 2.1 mags of visual extinction (Joy & Harvey 1997).

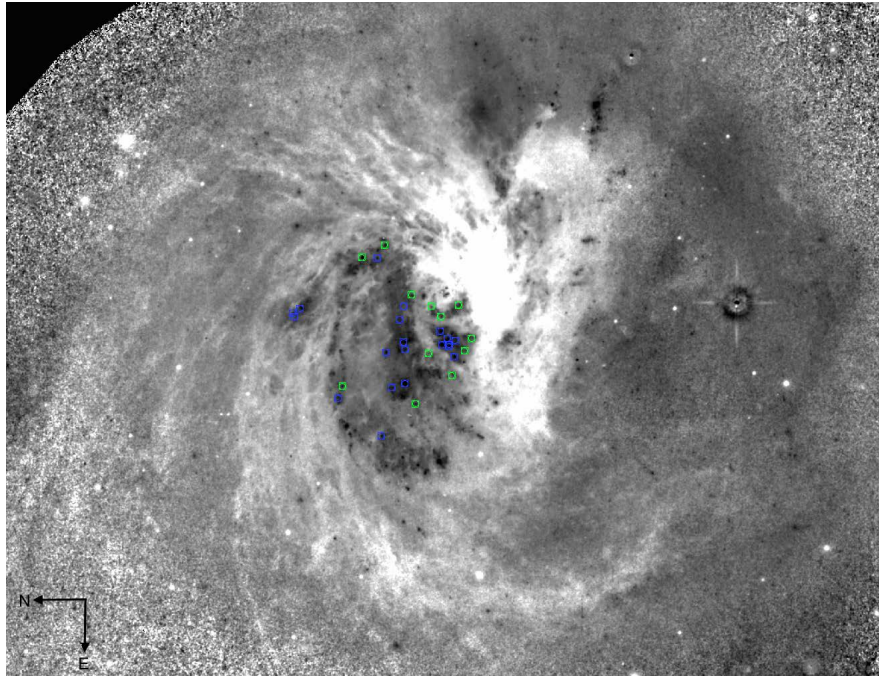


FIG. 29.— Inverted black and white B-I image of NGC 3256 taken with HST ACS/WFC F814W and F435W. The bright emission corresponds to redder (i.e. dustier) regions of the galaxy. The blue centroids correspond to clusters found in relatively “dust-free” regions of these galaxies, whereas the green centroids correspond to clusters found in relatively dustier regions of the galaxy.

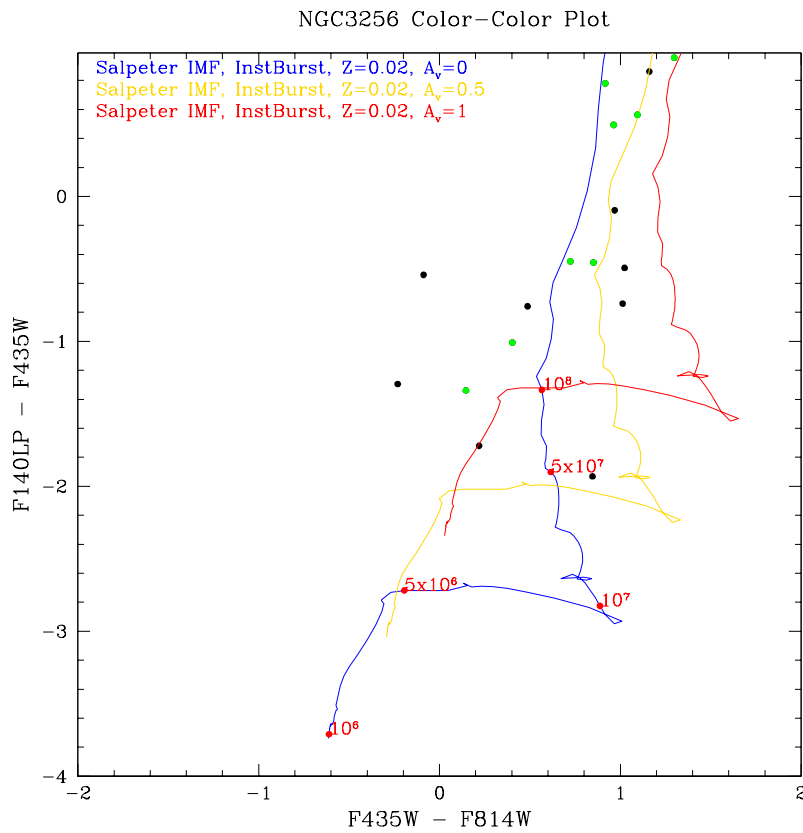


FIG. 30.— Color-Color plot of all star clusters identified in NGC 3256 in F814W, F435W, and F140LP plotted against SSP models with various amount of visual extinction. The green points correspond to the clusters found in dustier regions of the galaxy in Figure 29

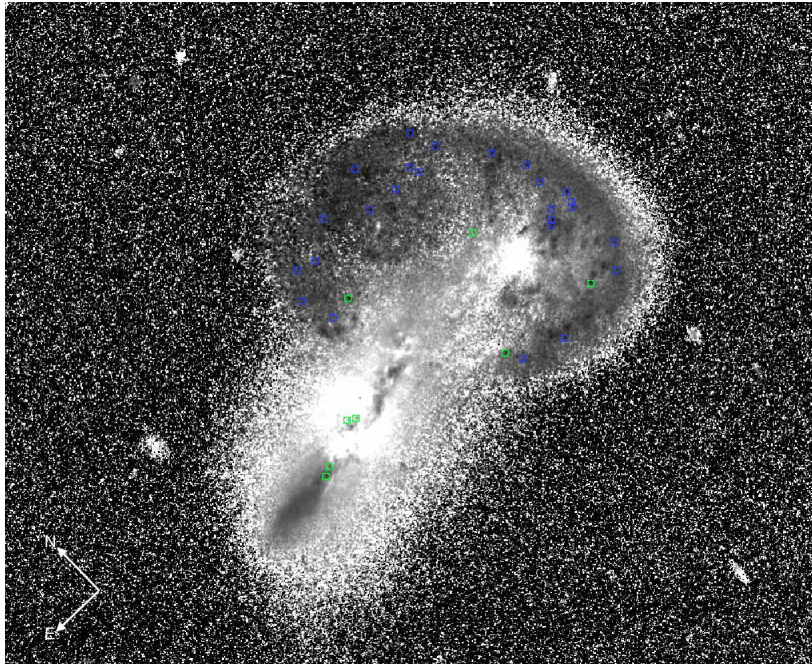


FIG. 31.— Inverted black and white B-I image of Arp 148 taken with HST ACS/WFC F814W and F435W. The bright emission corresponds to redder (i.e. dustier) regions of the galaxy. The blue centroids correspond to clusters found in relatively “dust-free” regions of these galaxies, whereas the green centroids correspond to clusters found in relatively dustier regions of the galaxy.

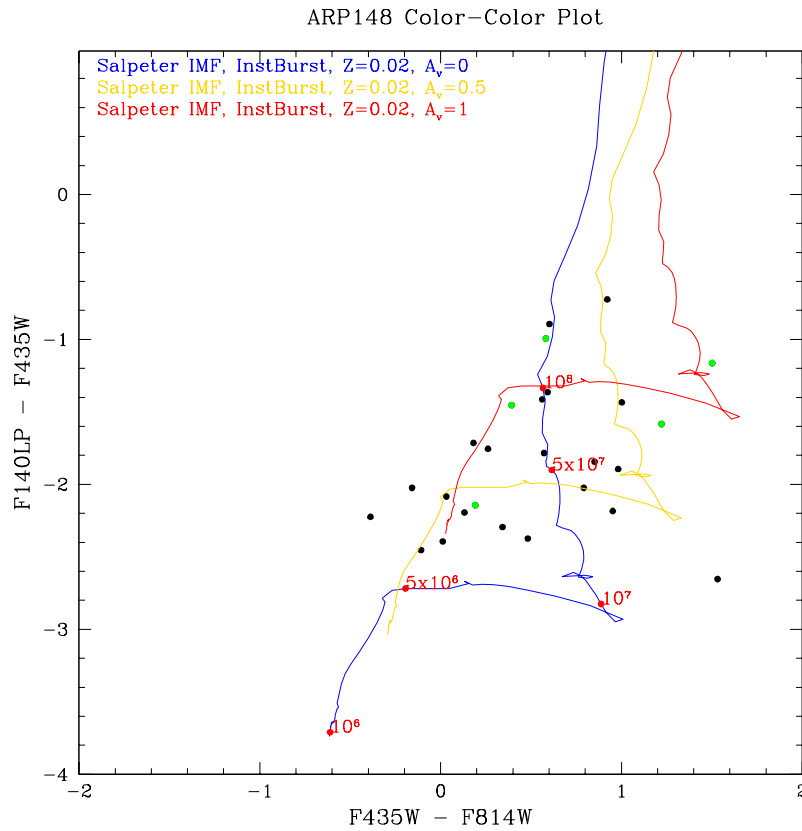


FIG. 32.— Color-Color plot of all star clusters identified in Arp 148 in F814W, F435W, and F140LP plotted against SSP models with various amount of visual extinction. The green points correspond to the clusters found in dustier regions of the galaxy in Figure 31

TABLE 19
OBSERVED PROPERTIES OF STAR CLUSTERS IN NGC 2623

ID	RA	Dec	M_B	σ_B	M_I	σ_I	M_{FUV}	σ_{FUV}
1	129.5980304	25.75459514	-14.04	0.01	-14.98	0.01	-13.25	0.02
2	129.5990031	25.7538954	-11.45	0.02	-11.94	0.05	-12.53	0.04
3	129.5994079	25.75382853	-11.39	0.02	-11.90	0.05	-12.41	0.05
4	129.5990874	25.751723	-11.53	0.01	-12.08	0.01	-11.79	0.05
5	129.5995056	25.75209619	-10.61	0.02	-10.88	0.03	-11.91	0.08
6	129.599766	25.75096143	-11.27	0.01	-11.85	0.01	-11.47	0.03
7	129.5999493	25.75179613	-13.15	0.01	-13.82	0.01	-12.75	0.04
8	129.6003718	25.75134324	-11.08	0.02	-11.09	0.05	-12.93	0.03
9	129.6010618	25.75100371	-11.58	0.01	-12.06	0.02	-12.89	0.03
10	129.6013548	25.75053983	-10.88	0.03	-11.40	0.03	-11.30	0.02
11	129.601522	25.75112441	-11.24	0.02	-11.68	0.02	-11.90	0.08

TABLE 20
DERIVED PROPERTIES OF STAR CLUSTERS IN NGC 2623

ID	Log(Age)	σ_{Age}	Log(M/M_\odot)	σ_M	A_V	σ_{A_V}
1	8.56	0.18	7.33	0.16	0.10	0.02
2	6.54	0.56	5.48	0.50	1.50	0.49
3	6.62	0.47	5.34	0.43	1.30	0.40
4	8.36	0.64	6.16	0.16	0.10	0.03
5	6.66	0.03	4.93	0.19	1.00	0.09
6	6.68	0.72	5.46	0.16	1.50	0.27
7	7.86	0.67	7.25	0.16	1.50	0.29
8	6.66	0.05	4.90	0.21	0.60	0.12
9	6.70	0.57	5.32	0.47	1.00	0.45
10	6.68	0.02	5.30	0.17	1.50	0.03
11	6.66	0.72	5.44	0.60	1.50	0.62

TABLE 21
OBSERVED PROPERTIES OF STAR CLUSTERS IN UGC 04881

ID	RA	Dec	M_B	σ_B	M_I	σ_I	M_{FUV}	σ_{FUV}
1	138.9806254	44.33224681	-13.41	0.02	-14.51	0.05	-11.65	0.13
2	138.9802968	44.33445408	-12.38	0.02	-13.38	0.01	-11.12	0.14
3	138.9841104	44.33189026	-13.48	0.01	-14.72	0.01	-11.29	0.01
4	138.9857806	44.32941604	-11.38	0.08	-12.28	0.11	-11.33	0.03
5	138.9861709	44.32809268	-10.97	0.13	-11.15	0.20	-12.59	0.16

TABLE 22
DERIVED PROPERTIES OF STAR CLUSTERS IN UGC 04881

ID	Log(Age)	σ_{Age}	Log(M/M_\odot)	σ_M	A_V	σ_{A_V}
1	8.71	0.03	7.17	0.23	0.01	0.16
2	8.06	0.02	7.27	0.19	1.90	0.09
3	8.71	0.10	7.36	0.16	0.30	5.62
4	6.68	0.44	5.71	0.53	1.90	0.52
5	6.66	0.36	4.97	0.42	0.80	0.37

NGC 3690E

NGC3690 is a mid-stage merger. NGC 3690E contains a multitude of star clusters and dust lanes from the southeast tip of the galaxy to the northwest. The maximum A_V adopted for this galaxy is 3.4 mags of visual extinction (Garcia-Marín et al. 2006).

NGC 3690W

NGC 3690W has the brightest cluster complexes in the merging system located $\sim 6.8''$ (1.6 kpc) from the resolved nucleus. Cluster-rich spiral arms extend north and westward from the nuclear region out to a maximum projected distance of $\sim 58''$ (14 kpc). The maximum A_V adopted for this galaxy is 3.9 mags of visual extinction (Garcia-Marín et al. 2006).

TABLE 23
OBSERVED PROPERTIES OF STAR CLUSTERS IN IC 2545

ID	RA	Dec	M_B	σ_B	M_I	σ_I	M_{FUV}	σ_{FUV}
1	151.5136356	-33.88528106	-10.23	0.08	-11.06	0.08	-11.36	0.11
2	151.5136616	-33.88695096	-10.55	0.07	-10.99	0.08	-11.95	0.11
3	151.5140689	-33.88785616	-10.73	0.07	-11.43	0.06	-11.72	0.13
4	151.5146406	-33.88747231	-9.72	0.13	-10.15	0.15	-11.22	0.26
5	151.5148205	-33.8873956	-10.48	0.09	-10.74	0.13	-11.64	0.17
6	151.515442	-33.88795458	-11.40	0.07	-11.61	0.08	-13.21	0.17
7	151.5153282	-33.88941777	-11.77	0.03	-12.68	0.03	-12.06	0.36
8	151.5152205	-33.89096417	-11.67	0.03	-11.46	0.05	-13.28	0.05
9	151.5155505	-33.88790446	-10.54	0.11	-10.86	0.19	-12.31	0.07
10	151.5161603	-33.88389939	-10.85	0.04	-11.52	0.04	-11.83	0.22
11	151.5172199	-33.88393251	-11.68	0.02	-12.21	0.03	-12.54	0.21
12	151.5168118	-33.8905397	-10.84	0.04	-10.95	0.07	-12.44	0.29
13	151.5177074	-33.88509063	-14.32	0.01	-15.84	0.01	-14.21	0.04
14	151.517576	-33.88570119	-10.70	0.20	-11.73	0.19	-11.88	0.36
15	151.5177403	-33.8853364	-14.65	0.02	-15.38	0.02	-14.71	0.03
16	151.5199867	-33.88613476	-9.91	0.19	-11.22	0.07	-12.03	0.01
17	151.5202629	-33.88460375	-12.84	0.03	-13.94	0.02	-12.17	0.06
18	151.5205798	-33.88546044	-11.59	0.04	-12.21	0.08	-12.04	0.27
19	151.5210485	-33.88549176	-11.29	0.04	-11.50	0.08	-11.79	0.24

TABLE 24
DERIVED PROPERTIES OF STAR CLUSTERS IN IC 2545

ID	Log(Age)	σ_{Age}	Log(M/M_\odot)	σ_M	A_V	σ_{A_V}
1	6.78	0.03	4.88	0.18	1.10	0.29
2	6.34	0.40	5.47	0.18	1.60	0.46
3	8.06	0.54	5.71	0.18	0.20	0.19
4	5.10	0.35	5.23	0.21	1.60	0.26
5	6.66	0.21	4.93	0.19	1.10	0.10
6	6.46	0.33	5.58	0.18	1.20	0.35
7	6.46	0.17	6.31	0.17	2.30	0.51
8	6.66	0.10	5.19	0.17	0.70	0.07
9	6.00	0.31	5.35	0.20	1.40	0.56
10	8.11	0.31	5.73	0.17	0.10	0.55
11	6.64	0.57	5.54	0.17	1.40	0.41
12	6.66	0.11	4.91	0.17	0.80	0.58
13	7.74	0.13	7.60	0.17	1.40	0.41
14	7.63	0.07	5.66	0.27	0.60	0.08
15	6.66	0.59	7.02	0.17	1.90	0.10
16	5.10	0.36	6.58	0.26	4.00	0.06
17	8.41	0.38	6.99	0.17	0.60	0.28
18	8.31	0.26	6.16	0.17	0.10	0.54
19	6.66	0.50	5.46	0.17	1.50	0.22

TABLE 25
OBSERVED PROPERTIES OF STAR CLUSTERS IN NGC 3256

ID	RA	Dec	M_B	σ_B	M_I	σ_I	M_{FUV}	σ_{FUV}
1	156.9608449	-43.9024964	-12.20	0.02	-12.93	0.03	-12.65	0.01
2	156.9612737	-43.90178128	-12.75	0.01	-12.90	0.01	-14.09	0.01
3	156.9630369	-43.90314637	-12.96	0.01	-13.87	0.01	-12.18	0.02
4	156.9636042	-43.9045422	-14.02	0.01	-14.82	0.01	-12.97	0.02
5	156.9634535	-43.90288363	-12.88	0.02	-14.04	0.02	-12.02	0.05
6	156.9635947	-43.90369683	-13.70	0.02	-15.00	0.01	-12.74	0.01
7	156.9633212	-43.89955977	-12.29	0.02	-13.32	0.02	-12.79	0.02
8	156.9634618	-43.89962047	-11.36	0.01	-12.37	0.02	-12.10	0.04
9	156.9640714	-43.90271444	-13.34	0.02	-14.31	0.01	-13.43	0.04
10	156.9646123	-43.90392525	-13.49	0.03	-13.98	0.03	-14.25	0.01
11	156.9652121	-43.90415987	-13.56	0.02	-13.33	0.03	-14.86	0.01
12	156.9653068	-43.90414225	-13.36	0.02	-13.27	0.04	-13.90	0.02
13	156.9655228	-43.9046008	-12.70	0.01	-13.66	0.01	-12.20	0.02
14	156.9654982	-43.90351402	-13.21	0.01	-14.42	0.01	-11.32	0.05
15	156.966498	-43.90415946	-13.52	0.01	-14.61	0.01	-12.95	0.01
16	156.9666609	-43.90272713	-13.74	0.01	-13.96	0.01	-15.46	0.01
17	156.9665347	-43.90083852	-10.75	0.01	-11.16	0.01	-11.76	0.03
18	156.9667894	-43.90232476	-10.09	0.05	-10.93	0.05	-12.02	0.02
19	156.9675522	-43.9029773	-12.70	0.01	-13.55	0.01	-13.15	0.01

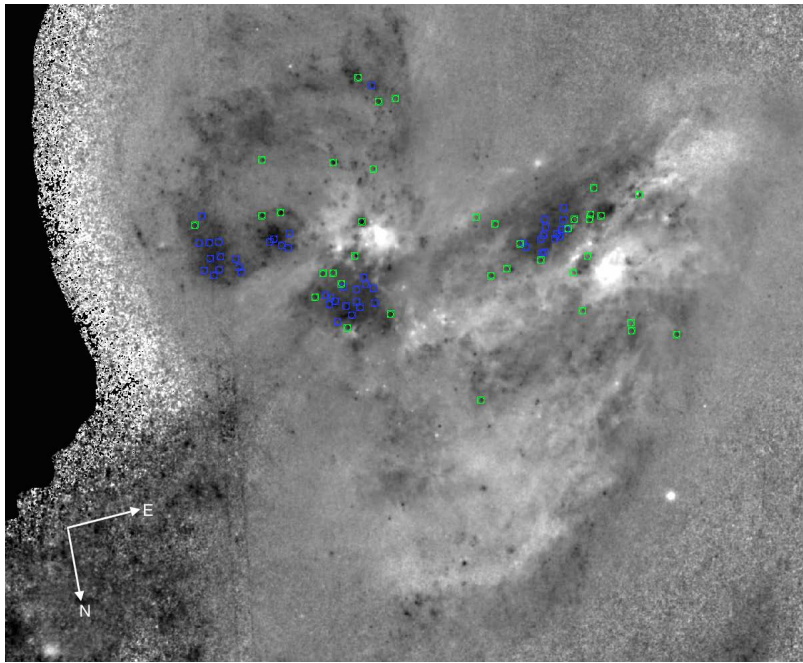


FIG. 33.— Inverted black and white B-I image of NGC 3690E taken with HST ACS/WFC F814W and F435W. The bright emission corresponds to redder (i.e. dustier) regions of the galaxy. The blue centroids correspond to clusters found in relatively “dust-free” regions of these galaxies, whereas the green centroids correspond to clusters found in relatively dustier regions of the galaxy.

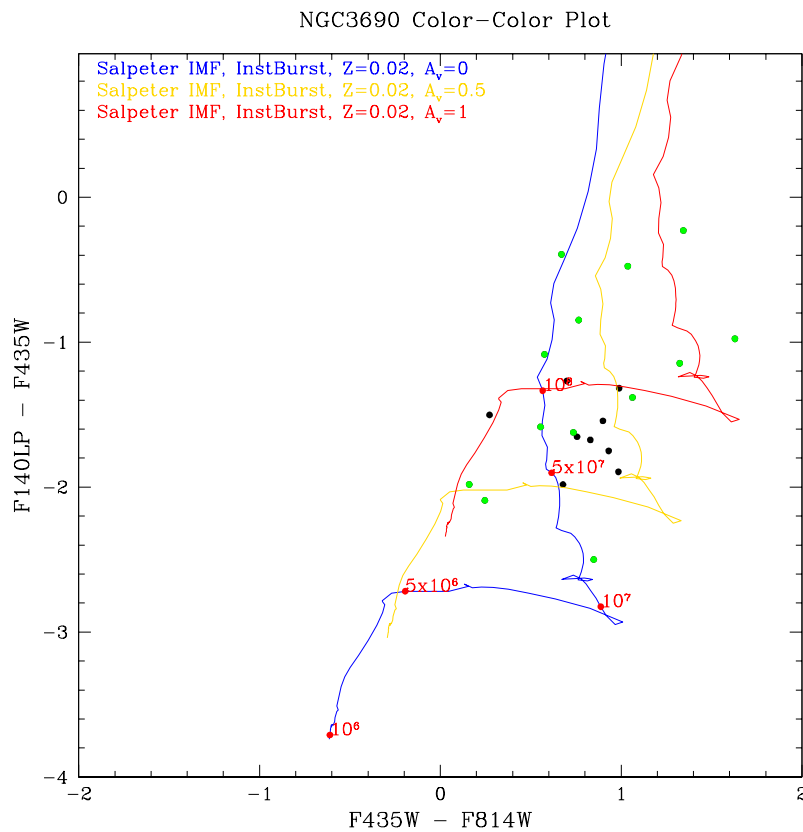


FIG. 34.— Color-Color plot of all star clusters identified in NGC 3690E in F814W, F435W, and F140LP plotted against SSP models with various amount of visual extinction. The green points correspond to the clusters found in dustier regions of the galaxy in Figure 33

TABLE 26
DERIVED PROPERTIES OF STAR CLUSTERS IN NGC 3256

ID	Log(Age)	σ_{Age}	Log(M/M_{\odot})	σ_M	A_V	σ_{A_V}
1	6.68	0.03	5.88	0.18	1.60	0.06
2	6.66	0.12	5.78	0.17	1.00	0.27
3	8.36	0.19	7.10	0.17	0.80	0.07
4	8.41	0.10	7.56	0.17	0.80	0.30
5	8.36	0.03	7.13	0.18	0.90	0.06
6	8.36	0.03	7.51	0.20	1.00	0.11
7	7.86	0.54	6.54	0.42	0.80	0.38
8	7.74	0.02	6.10	0.18	0.80	0.06
9	6.54	0.13	6.61	0.27	2.20	0.20
10	6.66	0.01	6.29	0.17	1.40	0.03
11	6.66	0.47	6.06	0.17	0.90	0.02
12	6.66	0.22	6.24	0.17	1.40	0.03
13	8.31	0.02	6.97	0.17	0.80	0.03
14	8.56	0.03	7.37	0.17	0.80	0.02
15	8.31	0.10	7.30	0.17	0.80	0.08
16	6.52	0.07	6.19	0.26	1.10	0.19
17	6.68	0.01	5.09	0.18	1.20	0.05
18	6.86	0.03	4.80	0.17	0.80	0.37
19	6.44	0.14	6.52	0.25	2.20	0.17

TABLE 27
OBSERVED PROPERTIES OF STAR CLUSTERS IN ARP 148

ID	RA	Dec	M_B	σ_B	M_I	σ_I	M_{FUV}	σ_{FUV}
1	165.968436	40.8519488	-12.21	0.01	-12.34	0.02	-14.41	0.02
2	165.9678663	40.8505602	-11.09	0.05	-11.12	0.10	-13.18	0.07
3	165.9683844	40.85145549	-11.10	0.03	-11.36	0.05	-12.86	0.09
4	165.9691046	40.85164919	-11.30	0.03	-11.90	0.04	-12.20	0.10
5	165.9690976	40.85147869	-11.19	0.03	-12.17	0.03	-13.09	0.09
6	165.967872	40.84958083	-10.44	0.07	-10.45	0.13	-12.84	0.09
7	165.9678992	40.84893317	-9.78	0.14	-11.31	0.08	-12.44	0.14
8	165.9680004	40.84887677	-11.27	0.05	-11.84	0.07	-13.06	0.08
9	165.9682628	40.84916472	-10.83	0.07	-11.39	0.08	-12.25	0.16
10	165.9677623	40.84910158	-11.64	0.03	-11.53	0.07	-14.10	0.03
11	165.9704139	40.85187208	-10.71	0.07	-10.55	0.18	-12.74	0.10
12	165.968608	40.84903015	-11.16	0.06	-11.64	0.09	-13.54	0.05
13	165.967709	40.84993148	-11.37	0.03	-11.55	0.05	-13.09	0.08
14	165.9682107	40.84793431	-10.78	0.11	-11.78	0.09	-12.22	0.16
15	165.9684927	40.8490672	-11.59	0.05	-11.93	0.08	-13.89	0.04
16	165.9687209	40.84766184	-12.23	0.03	-12.82	0.07	-13.60	0.05
17	165.9720438	40.85223589	-10.78	0.04	-11.57	0.04	-12.81	0.10
18	165.969655	40.85013869	-9.45	0.12	-10.67	0.10	-11.04	0.13
19	165.9692811	40.84792405	-13.17	0.02	-13.56	0.04	-14.63	0.02
20	165.9724453	40.852421	-9.47	0.14	-10.32	0.14	-11.32	0.01
21	165.9724057	40.85141491	-11.51	0.02	-11.70	0.04	-13.66	0.07
22	165.9716475	40.84859071	-11.98	0.02	-12.56	0.03	-12.98	0.09
23	165.9715595	40.84827508	-11.99	0.03	-12.91	0.04	-12.72	0.11
24	165.9706662	40.84783769	-10.84	0.04	-10.45	0.16	-13.07	0.08
25	165.9729915	40.85207186	-10.18	0.12	-11.13	0.11	-12.37	0.14
26	165.9748241	40.85035121	-12.83	0.04	-14.33	0.09	-14.00	0.03

NGC 5257E

NGC5257/8 is an early-stage merger system with the E and W nuclei separated by $\sim 80''$ (40 kpc). Star clusters and dust lanes make up the prominent spiral arms seen in the eastern galaxy. The maximum A_V adopted for this galaxy is 2.6 mags of visual extinction (Smith et al. 2014).

NGC 5257W

NGC 5257W contains a prominent group of bright clusters located $\sim 10''$ (5 kpc) south from the nucleus in a $\sim 17''$ (4.2 kpc) long spiral arm. The maximum A_V adopted for this galaxy is 1.8 mags of visual extinction (Smith et al. 2014).

TABLE 28
DERIVED PROPERTIES OF STAR CLUSTERS IN ARP 148

ID	Log(Age)	σ_{Age}	Log(M/M_{\odot})	σ_M	A_V	σ_{A_V}
1	5.10	0.67	5.96	0.39	1.10	0.35
2	6.56	0.42	4.91	0.36	0.70	0.32
3	6.70	0.51	4.97	0.34	0.70	0.29
4	6.60	0.56	5.35	0.40	1.40	0.36
5	7.12	0.18	5.44	0.19	0.50	0.10
6	6.36	0.36	5.03	0.34	0.90	0.29
7	5.10	0.01	5.52	0.27	2.10	0.15
8	6.76	0.49	5.02	0.35	0.60	0.30
9	6.74	0.79	4.99	0.55	0.90	0.55
10	6.60	0.57	4.90	0.36	0.30	0.32
11	6.66	0.11	4.70	0.28	0.50	0.20
12	6.86	0.23	4.91	0.20	0.20	0.10
13	6.52	0.18	5.25	0.31	1.10	0.26
14	7.63	0.31	5.58	0.33	0.40	0.26
15	6.76	0.05	4.98	0.18	0.30	0.07
16	6.72	0.70	5.59	0.58	1.00	0.60
17	7.49	0.20	5.42	0.21	0.20	0.13
18	7.34	0.24	5.07	0.27	0.70	0.18
19	6.42	0.22	6.39	0.33	1.50	0.28
20	7.52	0.34	4.97	0.31	0.30	0.22
21	6.72	0.32	4.99	0.35	0.40	0.30
22	6.46	0.46	6.13	0.50	1.80	0.49
23	6.74	0.45	5.72	0.38	1.40	0.34
24	6.66	0.03	4.65	0.21	0.30	0.12
25	7.30	0.23	5.13	0.27	0.30	0.17
26	7.06	0.17	6.35	0.20	1.10	0.11

TABLE 29
OBSERVED PROPERTIES OF STAR CLUSTERS IN NGC 3690E

ID	RA	Dec	M_B	σ_B	M_I	σ_I	M_{FUV}	σ_{FUV}
1	172.1336515	58.56572969	-11.56	0.01	-12.23	0.01	-11.95	0.02
2	172.1424578	58.56116578	-11.76	0.01	-12.83	0.02	-13.14	0.01
3	172.1388005	58.56124188	-10.20	0.05	-11.19	0.04	-11.52	0.05
4	172.1400284	58.56149757	-10.81	0.04	-10.97	0.14	-12.79	0.02
5	172.1345803	58.56118873	-8.96	0.04	-9.81	0.05	-11.46	0.03
6	172.1392395	58.56156972	-12.52	0.02	-14.15	0.01	-13.50	0.02
7	172.1399479	58.56161791	-11.73	0.02	-12.28	0.02	-13.31	0.02
8	172.1386985	58.56153798	-10.07	0.08	-10.97	0.10	-11.61	0.10
9	172.1378106	58.56146996	-10.01	0.04	-11.00	0.04	-11.91	0.04
10	172.1387899	58.56177443	-12.85	0.02	-13.61	0.03	-14.51	0.02
11	172.1385677	58.56177224	-12.15	0.03	-12.98	0.03	-13.82	0.02
12	172.1376673	58.5618607	-11.11	0.03	-11.81	0.03	-12.38	0.04
13	172.138187	58.56197966	-11.39	0.05	-12.33	0.07	-13.14	0.05
14	172.1366287	58.56197706	-10.22	0.18	-12.26	0.06	-11.91	0.06
15	172.1365065	58.56198534	-10.79	0.10	-12.11	0.05	-11.93	0.05
16	172.1367658	58.56209285	-10.89	0.04	-11.16	0.06	-12.39	0.04
17	172.1376122	58.56226713	-10.54	0.10	-11.22	0.08	-12.52	0.05
18	172.1357033	58.56256555	-9.68	0.08	-9.93	0.10	-11.77	0.02
19	172.1349188	58.56268913	-11.06	0.01	-11.80	0.02	-12.68	0.01
20	172.1390305	58.56385382	-11.61	0.02	-12.65	0.02	-12.09	0.02
21	172.1412556	58.56431432	-11.46	0.04	-12.81	0.02	-11.69	0.04
22	172.1412392	58.56451117	-11.52	0.02	-12.28	0.03	-12.36	0.01
23	172.1433592	58.56475551	-11.38	0.01	-11.95	0.01	-12.46	0.01

TABLE 30
 DERIVED PROPERTIES OF STAR CLUSTERS IN NGC 3690E

ID	Log(Age)	σ_{Age}	Log(M/M_{\odot})	σ_M	A_V	σ_{A_V}
1	8.46	0.01	6.13	0.17	0.01	0.15
2	6.94	0.05	5.66	0.17	1.00	0.35
3	7.00	0.23	5.22	0.24	1.10	0.15
4	6.56	0.43	5.06	0.42	1.00	0.38
5	6.82	0.01	3.99	0.19	0.20	0.06
6	6.82	0.83	5.99	0.18	1.30	0.04
7	7.76	0.31	5.88	0.31	0.20	0.25
8	6.98	0.30	4.99	0.27	0.90	0.19
9	6.84	0.04	4.64	0.19	0.60	0.06
10	7.24	0.15	6.25	0.22	0.70	0.13
11	6.98	0.20	5.77	0.20	0.80	0.10
12	6.74	0.46	5.31	0.41	1.20	0.37
13	6.92	0.12	5.32	0.19	0.70	0.06
14	7.65	0.24	5.21	0.30	0.20	0.15
15	6.84	0.11	5.26	0.22	1.20	0.09
16	6.52	0.30	5.29	0.37	1.40	0.32
17	7.42	0.30	5.23	0.30	0.30	0.21
18	6.72	0.45	4.49	0.42	0.70	0.38
19	7.12	0.20	5.49	0.25	0.80	0.17
20	7.76	0.27	6.26	0.29	1.00	0.22
21	7.57	0.27	6.30	0.29	1.40	0.22
22	8.16	0.84	6.01	0.69	0.20	0.74
23	6.42	0.42	5.91	0.47	1.90	0.44

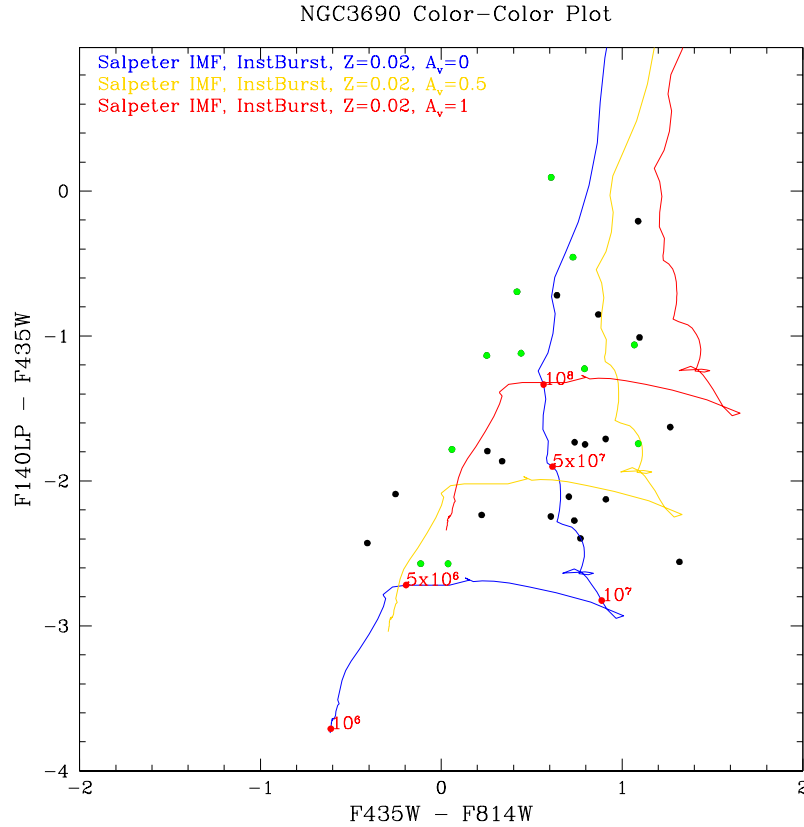


FIG. 35.— Color-Color plot of all star clusters identified in NGC 3690W in F814W, F435W, and F140LP plotted against SSP models with various amount of visual extinction. The green points correspond to the clusters found in dustier regions of the galaxy in Figure 33

TABLE 31
OBSERVED PROPERTIES OF STAR CLUSTERS IN NGC 3690W

ID	RA	Dec	M_B	σ_B	M_I	σ_I	M_{FUV}	σ_{FUV}
1	172.1298769	58.55733473	-11.32	0.01	-12.11	0.01	-12.55	0.02
2	172.128158	58.55936534	-10.84	0.01	-10.73	0.02	-13.41	0.01
3	172.1300076	58.5596496	-11.44	0.01	-12.51	0.01	-12.50	0.01
4	172.1253481	58.56042622	-11.36	0.01	-11.42	0.01	-13.14	0.02
5	172.1244337	58.56044047	-10.15	0.03	-10.19	0.04	-12.73	0.02
6	172.1291326	58.56092032	-14.92	0.01	-15.17	0.02	-16.05	0.02
7	172.1248588	58.5610534	-14.22	0.01	-14.83	0.01	-16.47	0.01
8	172.1246296	58.56111739	-11.76	0.03	-12.53	0.01	-14.16	0.02
9	172.1222293	58.56095288	-10.70	0.02	-11.44	0.03	-12.43	0.03
10	172.1251824	58.56124124	-10.38	0.14	-11.70	0.06	-12.94	0.04
11	172.1254777	58.56133083	-10.78	0.04	-11.00	0.06	-13.01	0.03
12	172.1222096	58.56131918	-11.41	0.03	-12.32	0.03	-13.12	0.03
13	172.1230124	58.56163962	-12.19	0.01	-12.99	0.01	-13.94	0.01
14	172.122073	58.5616329	-10.06	0.04	-9.65	0.14	-12.49	0.02
15	172.1231006	58.56176699	-10.62	0.02	-11.36	0.02	-12.90	0.02
16	172.1274401	58.56209845	-11.04	0.07	-12.13	0.05	-12.79	0.03
17	172.126965	58.5620665	-13.05	0.01	-13.66	0.02	-12.96	0.04
18	172.1217838	58.56176205	-11.84	0.01	-12.55	0.01	-13.95	0.01
19	172.128929	58.56247605	-10.89	0.09	-12.16	0.07	-12.52	0.07
20	172.1292452	58.56260576	-12.98	0.01	-14.07	0.01	-13.19	0.02
21	172.1284475	58.56257873	-10.60	0.06	-11.51	0.07	-12.73	0.03
22	172.1269226	58.56262585	-12.87	0.02	-13.74	0.02	-13.72	0.02
23	172.1264357	58.56263441	-13.24	0.02	-13.66	0.03	-13.93	0.02
24	172.1271745	58.56269741	-14.01	0.01	-15.11	0.01	-15.02	0.01
25	172.1292261	58.56297394	-12.57	0.01	-13.21	0.01	-13.29	0.02
26	172.1278642	58.56295651	-12.73	0.03	-12.98	0.04	-14.52	0.02
27	172.1285202	58.56303529	-11.18	0.04	-10.93	0.13	-13.27	0.03
28	172.1299061	58.56329793	-12.44	0.01	-12.88	0.02	-13.56	0.01
29	172.1280723	58.56319834	-12.29	0.05	-12.62	0.05	-14.15	0.02
30	172.1277823	58.56349895	-14.73	0.01	-15.46	0.02	-15.18	0.02

TABLE 32
DERIVED PROPERTIES OF STAR CLUSTERS IN NGC 3690W

ID	Log(Age)	σ_{Age}	Log(M/M_\odot)	σ_M	A_V	σ_{A_V}
1	6.78	0.02	5.27	0.18	1.00	0.05
2	6.42	0.16	5.03	0.19	0.70	0.06
3	7.63	0.34	6.00	0.30	0.70	0.23
4	6.66	0.10	5.07	0.17	0.70	1.12
5	5.10	0.40	5.03	0.18	0.90	0.04
6	6.66	8.74	6.70	0.18	1.10	0.03
7	6.84	0.01	6.26	0.17	0.50	0.30
8	6.88	0.01	5.35	0.17	0.50	0.17
9	6.84	0.01	4.95	0.18	0.70	0.04
10	5.10	0.01	6.71	0.23	3.90	0.02
11	5.10	0.67	5.39	0.29	1.10	0.22
12	6.88	0.04	5.32	0.18	0.70	0.05
13	6.86	0.10	5.59	0.17	0.70	1.12
14	6.52	0.02	4.40	0.19	0.50	0.06
15	6.88	0.01	4.90	0.17	0.50	0.20
16	7.42	0.20	5.65	0.21	0.50	0.09
17	8.31	0.35	6.95	0.35	0.50	0.30
18	6.86	0.01	5.34	0.17	0.50	0.99
19	5.10	0.19	6.92	0.24	3.90	0.12
20	8.01	0.48	6.89	0.41	0.80	0.37
21	6.90	0.10	4.94	0.19	0.50	0.42
22	6.74	0.58	6.02	0.44	1.30	0.41
23	6.66	6.61	6.19	0.18	1.40	0.04
24	7.65	0.29	7.05	0.25	0.70	0.18
25	6.62	0.06	5.92	0.23	1.50	0.14
26	6.38	0.49	6.18	0.36	1.30	0.30
27	6.66	0.08	4.89	0.22	0.50	0.12
28	6.64	0.06	5.73	0.23	1.20	0.15
29	6.72	0.43	5.40	0.35	0.60	0.30
30	6.68	0.03	6.89	0.18	1.60	0.05

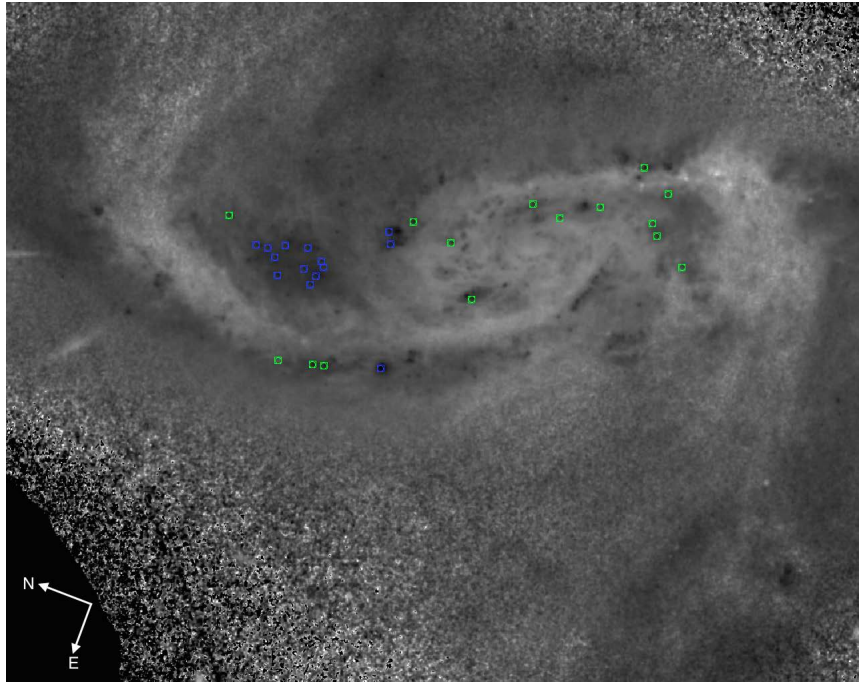


FIG. 36.— Inverted black and white B-I image of NGC 5257E taken with HST ACS/WFC F814W and F435W. The bright emission corresponds to redder (i.e. dustier) regions of the galaxy. The blue centroids correspond to clusters found in relatively “dust-free” regions of these galaxies, whereas the green centroids correspond to clusters found in relatively dustier regions of the galaxy.

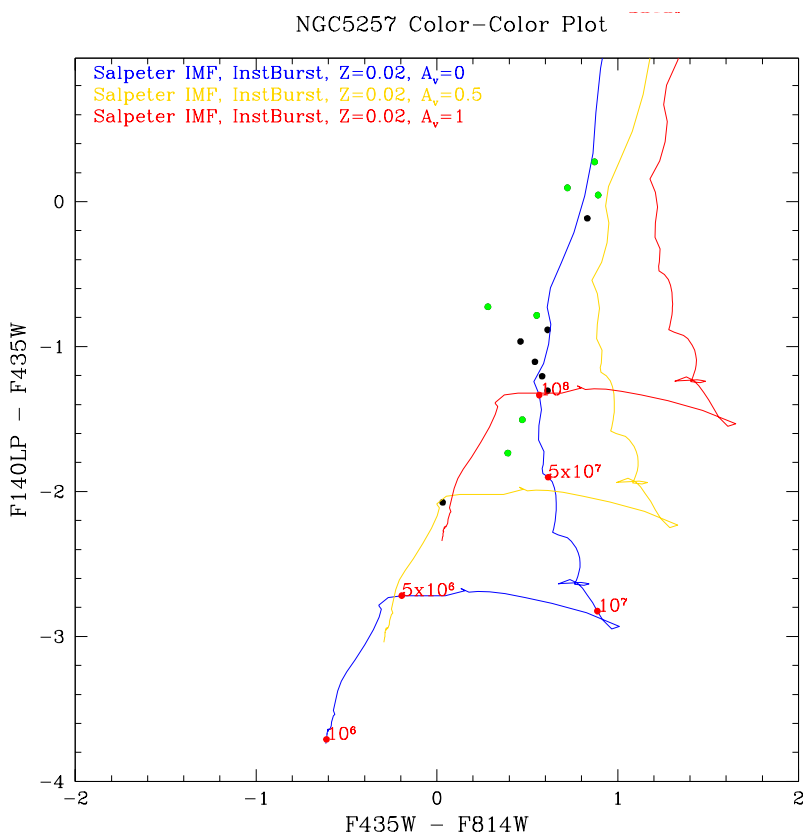


FIG. 37.— Color-Color plot of all star clusters identified in NGC 5257E F814W, F435W, and F140LP plotted against SSP models with various amount of visual extinction. The green points correspond to the clusters found in dustier regions of the galaxy in Figure 36

TABLE 33
OBSERVED PROPERTIES OF STAR CLUSTERS IN NGC 5257E

ID	RA	Dec	M_B	σ_B	M_I	σ_I	M_{FUV}	σ_{FUV}
1	204.988389	0.82941763	-15.90	0.01	-16.62	0.02	-15.81	0.01
2	204.9886135	0.828844213	-13.70	0.01	-14.98	0.01	-12.25	0.07
3	204.9893355	0.829802618	-12.13	0.01	-12.41	0.04	-12.86	0.04
4	204.99099	0.832602833	-12.33	0.01	-12.80	0.02	-13.84	0.02
5	204.9913336	0.832908072	-12.27	0.05	-12.88	0.03	-13.58	0.04
6	204.9893535	0.828699614	-12.67	0.02	-13.22	0.03	-13.46	0.02
7	204.9910317	0.83185232	-13.36	0.01	-14.25	0.02	-13.32	0.03
8	204.9915112	0.832786319	-12.80	0.06	-13.26	0.05	-13.77	0.05
9	204.992339	0.834417957	-11.11	0.10	-11.94	0.07	-11.23	0.18
10	204.9921984	0.834047212	-11.78	0.04	-12.36	0.05	-12.99	0.04
11	204.9928594	0.834311205	-13.27	0.01	-13.81	0.01	-14.38	0.01
12	204.9927539	0.833729231	-12.57	0.02	-13.18	0.02	-13.46	0.02
13	204.9917487	0.831103146	-14.21	0.02	-15.08	0.02	-13.94	0.01
14	204.9941781	0.833654938	-13.58	0.01	-15.28	0.01	-12.41	0.06
15	204.9935202	0.831994291	-15.04	0.01	-15.07	0.01	-17.12	0.01
16	204.993914	0.832897563	-12.26	0.04	-12.65	0.05	-14.00	0.01

TABLE 34
DERIVED PROPERTIES OF STAR CLUSTERS IN NGC 5257E

ID	Log(Age)	σ_{Age}	Log(M/M_\odot)	σ_M	A_V	σ_{A_V}
1	8.31	0.01	8.04	0.17	0.40	0.23
2	8.56	0.03	7.46	0.18	0.60	0.07
3	6.66	0.39	5.75	0.17	1.40	0.04
4	6.72	0.67	5.58	0.39	0.90	0.34
5	6.72	0.58	5.61	0.36	1.00	0.30
6	6.66	0.03	5.96	0.19	1.40	0.07
7	8.31	0.49	7.02	0.48	0.40	0.46
8	6.66	0.40	5.96	0.29	1.30	0.22
9	6.66	0.81	5.60	0.66	1.90	0.70
10	6.00	0.44	6.06	0.37	1.80	0.32
11	6.30	0.09	6.68	0.22	1.80	0.13
12	6.52	0.39	6.04	0.31	1.70	0.24
13	8.36	0.02	7.45	0.18	0.50	0.06
14	8.01	0.05	7.66	0.18	1.80	0.04
15	6.56	0.05	6.49	0.21	0.70	0.11
16	6.72	0.43	5.45	0.36	0.70	0.31

TABLE 35
OBSERVED PROPERTIES OF STAR CLUSTERS IN NGC 5257W

ID	RA	Dec	M_B	σ_B	M_I	σ_I	M_{FUV}	σ_{FUV}
1	204.9677325	0.839888315	-12.60	0.04	-13.26	0.04	-13.43	0.07
2	204.9676008	0.839405141	-14.32	0.02	-14.40	0.02	-16.43	0.01
3	204.9676117	0.839232784	-13.47	0.04	-13.90	0.05	-14.56	0.02
4	204.9679115	0.838666338	-12.25	0.06	-13.29	0.02	-14.24	0.06
5	204.9680284	0.838781875	-13.85	0.02	-14.10	0.03	-15.44	0.01
6	204.9679985	0.838669059	-13.07	0.06	-13.32	0.06	-15.08	0.04
7	204.969473	0.840889786	-13.17	0.01	-13.46	0.01	-14.21	0.01
8	204.9690871	0.839750205	-12.72	0.05	-13.41	0.07	-13.63	0.02
9	204.96912	0.837489752	-13.63	0.05	-14.12	0.08	-14.60	0.06
10	204.9692242	0.837503427	-15.05	0.02	-15.74	0.02	-16.38	0.01
11	204.970253	0.837864699	-12.01	0.02	-12.17	0.04	-14.13	0.01
12	204.9727531	0.841813782	-11.72	0.06	-11.67	0.09	-13.63	0.04
13	204.9703117	0.836690288	-13.97	0.02	-14.12	0.03	-15.22	0.03
14	204.9728795	0.841450503	-13.65	0.02	-13.86	0.03	-16.06	0.01
15	204.9730222	0.841315721	-12.87	0.04	-13.54	0.03	-14.71	0.02
16	204.9731456	0.841116419	-14.47	0.01	-14.61	0.02	-16.80	0.01
17	204.9735238	0.840747	-12.24	0.06	-12.70	0.07	-13.80	0.08
18	204.9737106	0.840991159	-12.21	0.04	-12.65	0.07	-14.41	0.02
19	204.9738917	0.840626292	-12.65	0.04	-13.15	0.03	-14.44	0.02
20	204.9736297	0.838529841	-13.22	0.03	-14.02	0.02	-14.44	0.02
21	204.974667	0.839754239	-12.11	0.03	-11.73	0.09	-14.16	0.02
22	204.9746698	0.838945129	-12.42	0.02	-12.28	0.05	-14.85	0.01

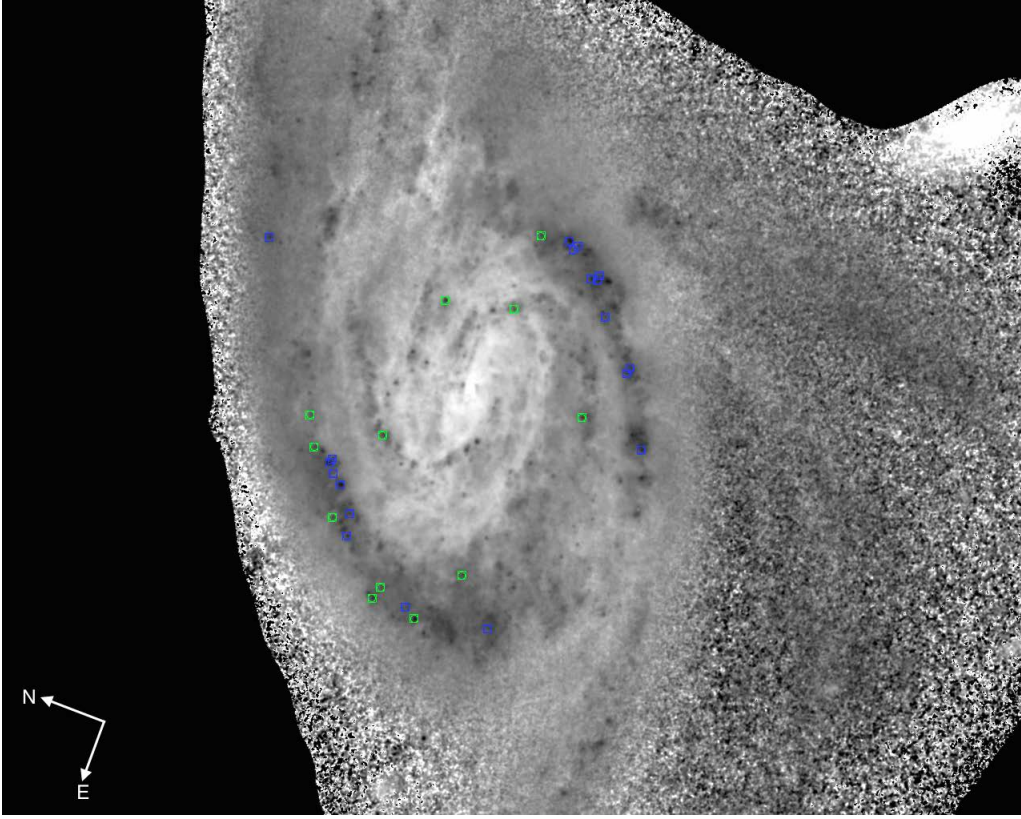


FIG. 38.— Inverted black and white B-I image of NGC 5257W taken with HST ACS/WFC F814W and F435W. The bright emission corresponds to redder (i.e. dustier) regions of the galaxy. The blue centroids correspond to clusters found in relatively “dust-free” regions of these galaxies, whereas the green centroids correspond to clusters found in relatively dustier regions of the galaxy.

TABLE 36
DERIVED PROPERTIES OF STAR CLUSTERS IN NGC 5257W

ID	Log(Age)	σ_{Age}	Log(M/M_{\odot})	σ_M	A_V	σ_{A_V}
1	6.56	0.64	6.19	0.59	1.80	0.60
2	6.48	0.09	6.57	0.22	1.10	0.13
3	6.48	0.04	6.60	0.20	1.80	0.09
4	6.24	0.02	6.35	0.20	1.80	0.07
5	6.54	0.03	6.42	0.19	1.30	0.07
6	6.72	0.34	5.84	0.32	0.70	0.26
7	6.54	0.01	6.30	0.18	1.60	0.05
8	6.64	0.59	6.25	0.54	1.70	0.53
9	6.54	0.29	6.54	0.35	1.70	0.29
10	6.74	0.32	6.83	0.29	1.10	0.23
11	6.58	0.30	5.50	0.29	0.90	0.22
12	6.54	0.03	5.40	0.21	1.00	0.09
13	6.52	0.01	6.57	0.18	1.50	0.03
14	6.74	0.01	5.90	0.17	0.40	0.02
15	7.30	0.19	6.19	0.21	0.50	0.10
16	6.72	0.01	6.29	0.18	0.50	0.05
17	6.58	0.24	5.81	0.31	1.30	0.24
18	6.76	0.16	5.37	0.19	0.50	0.07
19	6.74	0.17	5.71	0.19	0.80	0.07
20	7.63	0.27	6.60	0.26	0.60	0.19
21	6.52	0.01	5.51	0.18	0.90	0.05
22	6.52	0.05	5.53	0.20	0.70	0.10

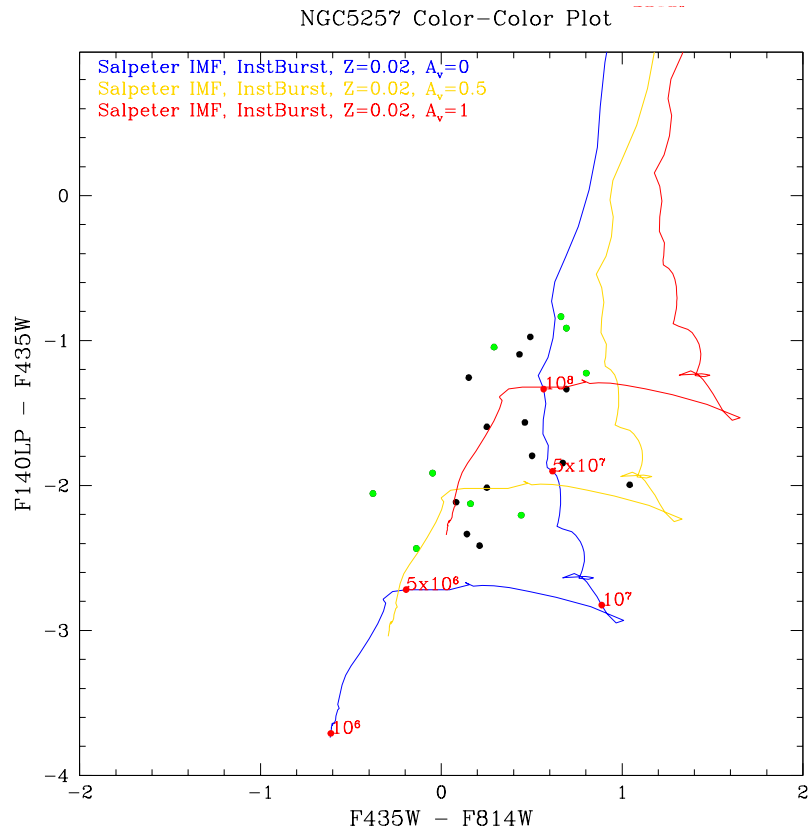


FIG. 39.— Color-Color plot of all star clusters identified in NGC 5257W in F814W, F435W, and F140LP plotted against SSP models with various amount of visual extinction. The green points correspond to the clusters found in dustier regions of the galaxy in Figure 38

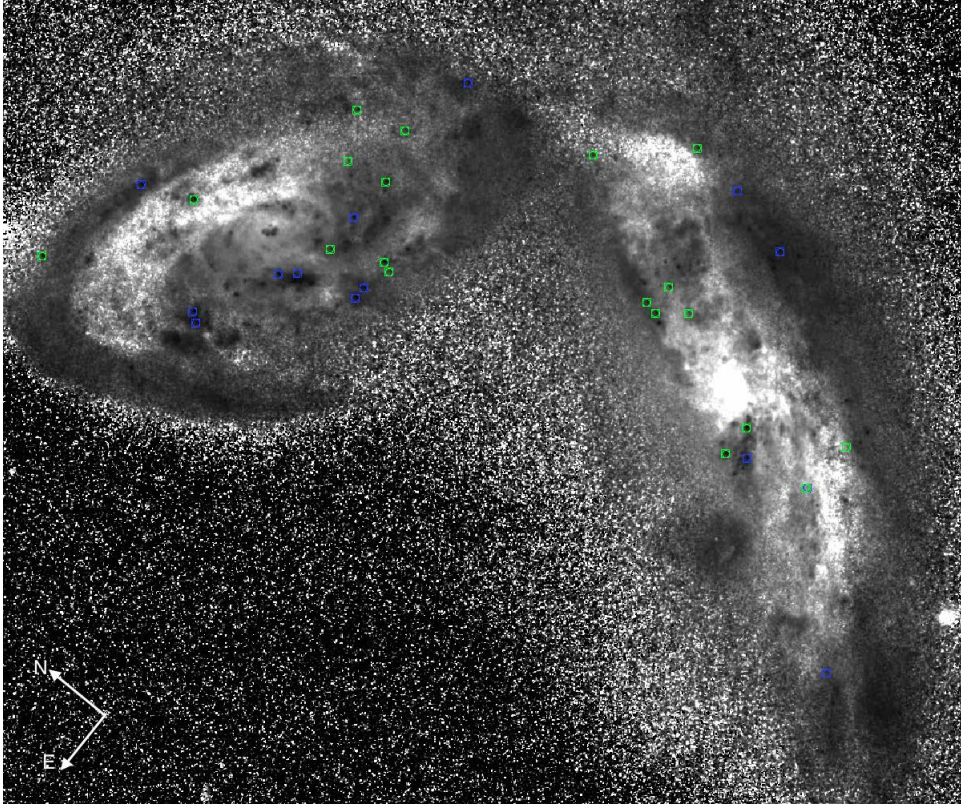


FIG. 40.— Inverted black and white B-I image of NGC 5331S taken with HST ACS/WFC F814W and F435W. The bright emission corresponds to redder (i.e. dustier) regions of the galaxy. The blue centroids correspond to clusters found in relatively “dust-free” regions of these galaxies, whereas the green centroids correspond to clusters found in relatively dustier regions of the galaxy.

TABLE 37
OBSERVED PROPERTIES OF STAR CLUSTERS IN NGC 5331S

ID	RA	Dec	M_B	σ_B	M_I	σ_I	M_{FUV}	σ_{FUV}
1	208.0703109	2.098268967	-9.51	0.10	-10.42	0.10	-9.83	0.11
2	208.0667504	2.102795958	-12.63	0.03	-13.47	0.03	-8.96	0.07
3	208.0676478	2.100879121	-15.03	0.01	-15.70	0.01	-10.76	0.27
4	208.0681184	2.100981506	-12.59	0.02	-13.40	0.03	-9.66	0.19
5	208.0672543	2.099466214	-9.90	0.07	-12.06	0.03	-9.13	0.18
6	208.0680338	2.099718103	-9.64	0.10	-11.49	0.10	-9.78	0.26
7	208.068045	2.100690283	-13.34	0.03	-14.10	0.02	-9.69	0.14

TABLE 38
DERIVED PROPERTIES OF STAR CLUSTERS IN NGC 5331S

ID	Log(Age)	σ_{Age}	Log(M/M_\odot)	σ_M	A_V	σ_{A_V}
1	6.50	0.38	5.53	0.20	2.30	0.37
2	8.76	0.58	8.08	0.17	1.80	0.55
3	8.86	0.44	9.13	0.17	1.80	0.31
4	8.61	0.43	7.93	0.17	1.80	0.28
5	6.80	0.35	5.85	0.19	2.50	0.92
6	6.82	0.51	5.46	0.20	1.90	0.70
7	7.91	0.13	8.70	0.18	3.60	0.05

NGC 5331S

NGC 5331 is a mid-stage merging system. NGC 5331S and N have a projected nuclear separation of $\sim 27''$ (19 kpc). Large dust lanes are visible along the near edge of the galaxy, and only a small number of star clusters are visible. The maximum A_V adopted for this galaxy is 3.6 mags of visual extinction (Lutz 1992).

NGC5331 Color-Color Plot

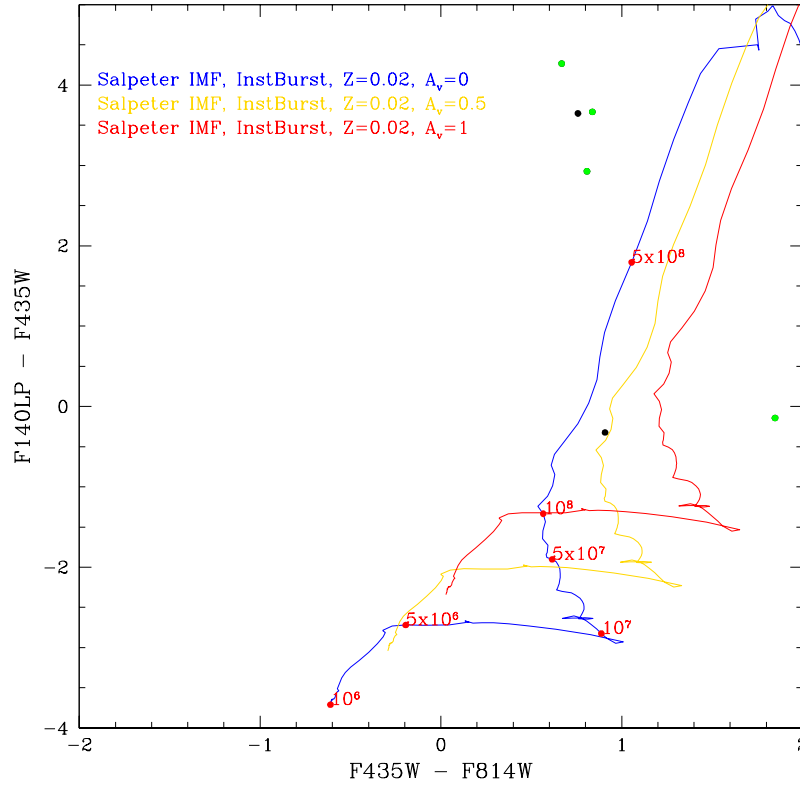


FIG. 41.— Color-Color plot of all star clusters identified in NGC 5331S in F814W, F435W, and F140LP plotted against SSP models with various amount of visual extinction. The green points correspond to the clusters found in dustier regions of the galaxy in Figure 40

TABLE 39
OBSERVED PROPERTIES OF STAR CLUSTERS IN NGC 5331N

ID	RA	Dec	M_B	σ_B	M_I	σ_I	M_{FUV}	σ_{FUV}
1	208.0660418	2.10796331	-9.62618	0.07	-10.20	0.10	-11.87	0.10
2	208.0660027	2.107205416	-9.75618	0.07	-10.89	0.07	-10.83	0.07
3	208.0667669	2.107753228	-9.37618	0.09	-10.89	0.08	-10.12	0.11
4	208.068404	2.11027354	-12.4562	0.02	-13.02	0.02	-13.13	0.03
5	208.0682536	2.109496656	-11.5962	0.02	-11.98	0.05	-12.80	0.04
6	208.0667871	2.107126587	-11.0962	0.03	-11.62	0.05	-11.60	0.14
7	208.0674622	2.107317376	-12.2362	0.03	-13.18	0.04	-13.14	0.03
8	208.0684892	2.106770333	-12.9062	0.01	-13.48	0.01	-13.11	0.03
9	208.0678413	2.106630757	-11.5662	0.03	-11.87	0.05	-12.68	0.05
10	208.0683038	2.10672568	-11.4162	0.03	-11.50	0.08	-12.26	0.07
11	208.0686796	2.107921587	-13.8362	0.01	-14.44	0.01	-13.80	0.02
12	208.0666683	2.102976709	-12.5562	0.02	-13.41	0.02	-11.52	0.01
13	208.0698361	2.108671969	-10.3762	0.09	-10.51	0.14	-11.62	0.12
14	208.0685396	2.107683102	-11.6562	0.07	-13.34	0.02	-11.38	0.16
15	208.0699658	2.111094004	-10.4662	0.03	-11.17	0.03	-9.81	0.13
16	208.0697116	2.108783852	-11.8962	0.02	-12.40	0.02	-12.89	0.04

NGC 5331N

NGC 5331N has a nucleus and two distinct spiral arms, with a small number of star clusters visible throughout the galaxy. The maximum A_V adopted for this galaxy is 1.8 mags of visual extinction (Lutz 1992).

UGC 09618NED02

Armus et al. (2009) discusses the detailed morphology of this galaxy at length. UGC 09618NED02 is an early-stage merger with the two nuclei separated by $\sim 40''$ (30 kpc). Multiple star clusters are visible along the spiral arms in the face-on galaxy (VV430A). The maximum A_V adopted for this galaxy is 2.4 mags of visual extinction (Leech et al. 1989).

TABLE 40
DERIVED PROPERTIES OF STAR CLUSTERS IN NGC 5331N

ID	Log(Age)	σ_{Age}	Log(M/M_{\odot})	σ_M	A_V	σ_{A_V}
1	6.86	0.33	4.64	0.25	0.30	0.15
2	7.54	0.34	5.65	0.30	0.80	0.23
3	7.42	0.24	5.65	0.27	1.20	0.17
4	6.66	0.35	6.23	0.37	1.50	0.32
5	6.66	0.11	5.67	0.27	1.10	0.20
6	8.31	0.01	6.20	0.18	0.01	0.04
7	6.78	0.44	6.09	0.36	1.30	0.30
8	6.66	0.02	6.56	0.18	1.80	0.05
9	6.66	0.04	5.71	0.21	1.20	0.10
10	6.66	0.04	5.70	0.19	1.30	0.07
11	6.68	0.30	6.94	0.17	1.80	0.08
12	8.61	0.15	7.08	0.18	0.10	0.05
13	6.66	0.35	5.13	0.28	1.00	0.19
14	7.65	0.11	6.88	0.22	1.60	0.11
15	8.56	0.02	6.14	0.17	0.01	0.13
16	6.64	0.08	5.86	0.26	1.30	0.18

TABLE 41
OBSERVED PROPERTIES OF STAR CLUSTERS IN UGC 09618NED02

ID	RA	Dec	M_B	σ_B	M_I	σ_I	M_{FUV}	σ_{FUV}
1	224.2502774	24.60907674	-10.22	0.19	-10.97	0.15	-12.23	0.18
2	224.2495249	24.60924743	-11.10	0.03	-11.63	0.04	-13.86	0.18
3	224.2494326	24.60905594	-11.83	0.03	-11.84	0.04	-13.88	0.04
4	224.247693	24.60664702	-11.07	0.08	-12.15	0.05	-12.51	0.14
5	224.2474984	24.6053126	-11.00	0.04	-11.08	0.08	-12.97	0.08
6	224.2477925	24.60476143	-11.71	0.03	-11.78	0.05	-13.48	0.06
7	224.2513684	24.6094958	-12.99	0.02	-13.71	0.02	-13.24	0.07
8	224.2481156	24.6045755	-11.08	0.05	-11.84	0.05	-12.47	0.18
9	224.2516575	24.60893269	-13.11	0.01	-13.66	0.01	-13.57	0.02
10	224.2516642	24.60837604	-11.69	0.07	-12.07	0.08	-13.22	0.07
11	224.2504346	24.60641579	-12.52	0.05	-12.88	0.06	-13.34	0.06
12	224.2504328	24.60598905	-12.40	0.02	-12.52	0.06	-13.33	0.17
13	224.25063	24.60618376	-11.50	0.07	-11.92	0.11	-12.17	0.05
14	224.2519383	24.60779872	-14.50	0.01	-14.62	0.01	-15.57	0.01
15	224.2510431	24.60655958	-13.33	0.04	-13.35	0.13	-14.03	0.03
16	224.2514028	24.6069871	-13.30	0.07	-13.37	0.14	-13.88	0.04
17	224.2510282	24.6063554	-13.65	0.02	-13.90	0.03	-14.54	0.02
18	224.2506515	24.60573423	-11.61	0.05	-11.63	0.08	-12.52	0.14
19	224.2513638	24.60674976	-15.35	0.01	-17.06	0.01	-14.45	0.02
20	224.2518985	24.60745116	-13.16	0.02	-13.71	0.02	-13.61	0.05
21	224.2520755	24.60771662	-11.17	0.14	-11.78	0.13	-12.63	0.12
22	224.2523005	24.60793133	-12.08	0.06	-12.72	0.06	-13.20	0.07
23	224.2504648	24.6053105	-12.88	0.01	-13.37	0.02	-13.53	0.01
24	224.2495097	24.60387414	-11.68	0.03	-12.32	0.05	-13.31	0.14
25	224.2508571	24.60526342	-11.73	0.04	-12.17	0.06	-12.80	0.11
26	224.2510791	24.60533372	-12.61	0.02	-12.80	0.04	-13.65	0.05
27	224.2526081	24.60727308	-12.41	0.04	-12.81	0.04	-13.05	0.08
28	224.2496684	24.60197058	-11.11	0.04	-11.31	0.06	-13.09	0.08
29	224.2516261	24.6044602	-11.22	0.04	-11.31	0.07	-12.98	0.03
30	224.2525706	24.60577791	-11.27	0.03	-11.56	0.06	-12.27	0.17
31	224.2521417	24.60475683	-11.61	0.04	-12.03	0.03	-13.21	0.03
32	224.2525986	24.60531766	-11.85	0.02	-12.32	0.03	-12.76	0.18
33	224.2528334	24.60566186	-11.89	0.03	-12.38	0.03	-12.54	0.15
34	224.2521531	24.60254189	-12.79	0.01	-12.85	0.02	-14.60	0.02
35	224.2524271	24.6028813	-10.56	0.07	-10.95	0.07	-12.19	0.11
36	224.2531559	24.60341951	-11.72	0.03	-11.91	0.04	-13.39	0.06
37	224.2527859	24.60292948	-11.65	0.02	-11.59	0.04	-13.43	0.02
38	224.2541651	24.60499864	-11.06	0.03	-11.21	0.06	-12.65	0.02
39	224.2528804	24.6024864	-12.38	0.02	-12.51	0.03	-13.78	0.04
40	224.2530173	24.60254644	-11.29	0.06	-11.34	0.07	-12.27	0.18
41	224.2536233	24.60299199	-13.79	0.01	-13.59	0.01	-16.10	0.01
42	224.2548158	24.60471647	-11.68	0.02	-12.06	0.03	-13.32	0.12
43	224.2506179	24.60923582	-12.07	0.03	-12.81	0.04	-13.33	0.06

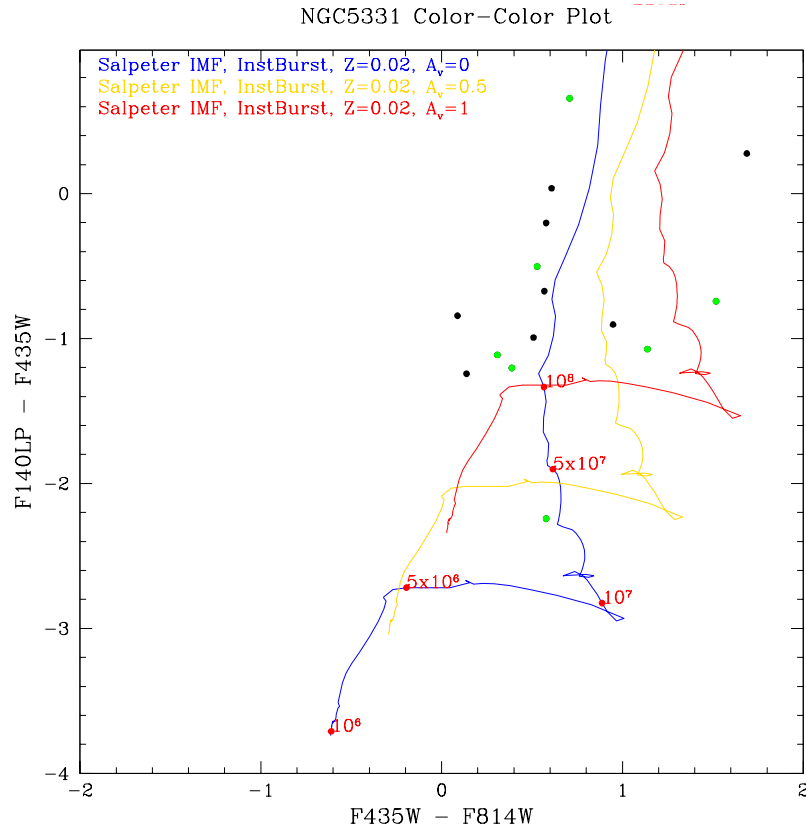


FIG. 42.— Color-Color plot of all star clusters identified in NGC 5331N in F814W, F435W, and F140LP plotted against SSP models with various amount of visual extinction. The green points correspond to the clusters found in dustier regions of the galaxy in Figure 40

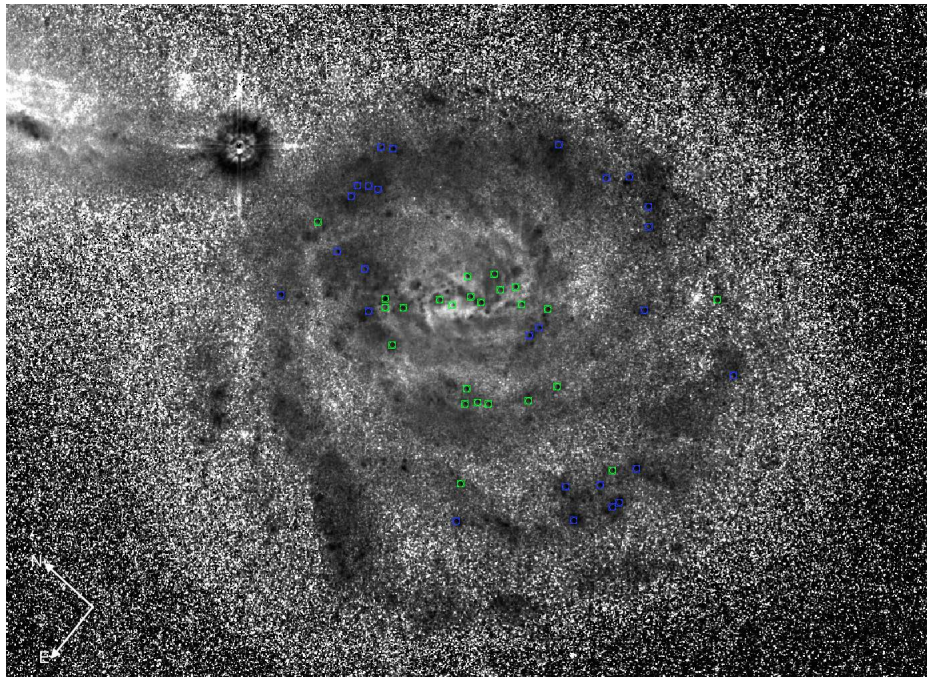


FIG. 43.— Inverted black and white B-I image of UGC 09618NED02 taken with HST ACS/WFC F814W and F435W. The bright emission corresponds to redder (i.e. dustier) regions of the galaxy. The blue centroids correspond to clusters found in relatively “dust-free” regions of these galaxies, whereas the green centroids correspond to clusters found in relatively dustier regions of the galaxy.

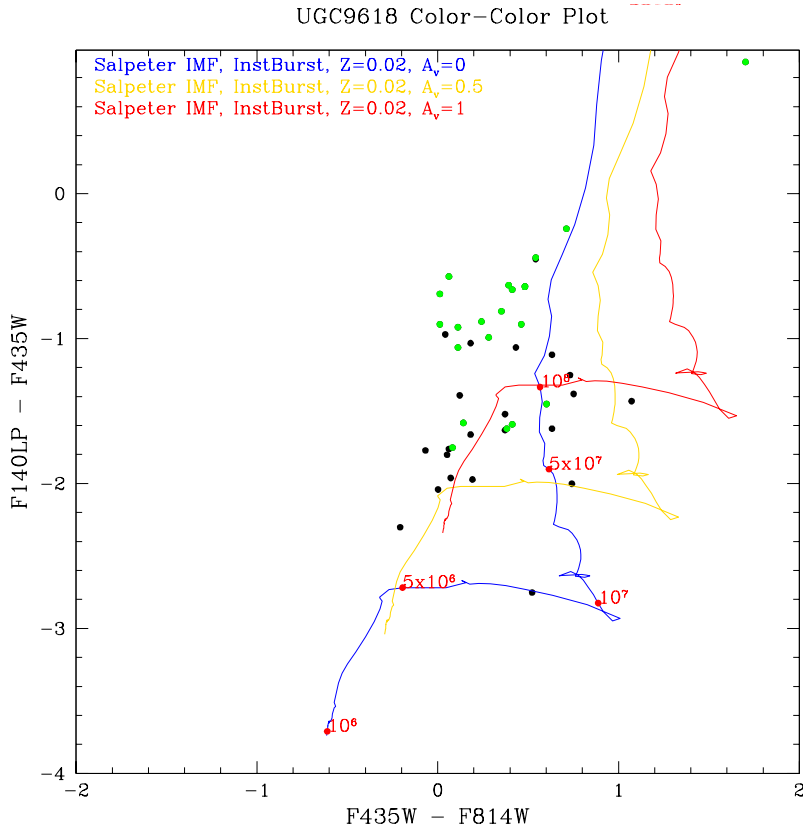


FIG. 44.— Color-Color plot of all star clusters identified in UGC 09618NED02 in F814W, F435W, and F140LP plotted against SSP models with various amount of visual extinction. The green points correspond to the clusters found in dustier regions of the galaxy in Figure 43

IC 4687N

IC 4687 is an early-stage merging system. The two primary galaxies (IC 4686 and IC 4687) have a nuclear separation of $\sim 84''$ (31 kpc). The northern galaxy contains several bright clusters in a nuclear arm stretching north and westward. The maximum A_V adopted for this galaxy is 2.8 mags of visual extinction (Rich et al. 2012).

IC 4687S

The southern galaxy contains several bright clusters in the nuclear region as well as a series of dust lanes. There is little evidence of extended tidal structures which contain star clusters. The maximum A_V adopted for this galaxy is 3.7 mags of visual extinction (Rich et al. 2012).

NGC 6786

NGC 6786 is an early-stage merger consisting of a pair of face-on galaxies with a nuclear separation of $\sim 72''$ (37 kpc). Faint star clusters are seen along the inner spiral structure. The brightest clusters sit at roughly $5''$ (3 kpc) from the southwest nucleus in the large arm/tail extending between the two galaxies. The maximum A_V adopted for this galaxy is 2.0 mags of visual extinction (Martin et al. 1991).

IRAS 20351+2521

IRAS 20351+2521 is an early-stage merger containing multiple star clusters in the northern region where the spiral arms diffuse into multiple components beyond the inner $\sim 5''$ (4 kpc). The maximum A_V adopted for this galaxy is 4.7 mags of visual extinction, which is lower than the cited value of 9.4 mags, but prevents our model from predicting masses unrealistically high for even the most massive YSCs found in the sample. (Stierwalt et al. 2013).

II ZW 096

Inami et al. (2010) discusses the detailed morphology of this galaxy at length. II Zw 096 is a mid-stage merging system. The western component is a roughly face-on spiral galaxy with star clusters along the spiral arms. The southeast end of the spiral, approximately $11.6''$ (8.4 kpc) from the nucleus, contains a distinct cluster-rich region. The maximum A_V adopted for this galaxy is 3.0 mags of visual extinction (Inami et al. 2010).

ESO 148-IG002

ESO 148-IG002 is a late-stage merger with a projected nuclear separation of $\sim 4.7''$ (4.2 kpc). The galaxy has a series of bright clusters which lie along a north-south ridge to the east of the bulge. The maximum A_V adopted for

TABLE 42
DERIVED PROPERTIES OF STAR CLUSTERS IN UGC
09618NED02

ID	Log(Age)	σ_{Age}	Log(M/M_{\odot})	σ_M	A_V	σ_{A_V}
1	7.57	0.39	5.17	0.41	0.10	0.32
2	6.88	0.05	4.82	0.16	0.01	0.45
3	6.66	0.09	5.15	0.25	0.50	0.18
4	7.63	0.28	5.70	0.28	0.40	0.21
5	6.64	0.20	4.84	0.34	0.60	0.29
6	6.66	0.03	5.21	0.19	0.70	0.09
7	8.41	0.03	6.73	0.17	0.01	0.05
8	6.76	0.52	5.10	0.38	0.90	0.34
9	6.66	0.02	6.25	0.16	1.60	0.04
10	6.38	0.65	5.87	0.53	1.50	0.52
11	6.66	0.57	5.85	0.49	1.30	0.47
12	6.66	0.53	5.75	0.16	1.20	0.03
13	6.66	0.75	5.55	0.63	1.50	0.66
14	6.66	0.95	6.54	0.16	1.10	0.03
15	6.66	0.57	6.18	0.48	1.30	0.46
16	6.66	0.77	6.22	0.61	1.40	0.63
17	6.66	0.67	6.30	0.16	1.30	0.04
18	6.66	0.16	5.43	0.18	1.20	0.05
19	7.86	0.04	8.29	0.17	1.80	0.05
20	8.36	0.03	6.76	0.16	0.01	0.03
21	6.74	0.75	5.13	0.53	0.90	0.51
22	5.10	0.97	6.34	0.66	1.90	0.70
23	6.66	0.03	6.10	0.16	1.50	0.02
24	6.76	0.47	5.29	0.37	0.80	0.33
25	6.66	0.26	5.48	0.35	1.20	0.31
26	6.66	0.51	5.83	0.17	1.20	0.05
27	6.66	0.75	5.91	0.61	1.50	0.63
28	6.36	0.46	5.45	0.36	1.20	0.31
29	6.66	0.09	5.01	0.24	0.70	0.17
30	6.66	0.43	5.30	0.17	1.20	0.04
31	6.72	0.64	5.24	0.47	0.80	0.45
32	6.66	0.01	5.58	0.16	1.30	0.02
33	6.66	0.03	5.71	0.16	1.50	0.04
34	6.66	0.01	5.64	0.16	0.70	0.03
35	6.00	0.65	5.42	0.50	1.50	0.48
36	6.66	0.25	5.27	0.25	0.80	0.18
37	6.66	0.86	5.19	0.16	0.70	0.04
38	6.66	0.04	5.00	0.20	0.80	0.11
39	6.66	0.07	5.58	0.17	0.90	0.05
40	6.66	0.35	5.31	0.34	1.20	0.28
41	6.66	0.36	5.83	0.16	0.30	0.06
42	5.10	0.67	5.96	0.38	1.50	0.34
43	6.78	0.55	5.57	0.43	1.00	0.40

TABLE 43
OBSERVED PROPERTIES OF STAR CLUSTERS IN IC 4687N

ID	RA	Dec	M_B	σ_B	M_I	σ_I	M_{FUV}	σ_{FUV}
1	273.4245591	-57.72132281	-8.50	0.12	-9.60	0.08	-11.68	0.07
2	273.4139193	-57.72470603	-12.61	0.02	-14.37	0.02	-11.88	0.10
3	273.4144883	-57.72459737	-14.21	0.03	-14.55	0.03	-15.57	0.02
4	273.4149949	-57.72446495	-13.59	0.03	-14.94	0.03	-14.02	0.07
5	273.4167849	-57.72402211	-11.55	0.05	-12.45	0.04	-12.21	0.07
6	273.4229748	-57.72139585	-10.56	0.03	-10.94	0.04	-12.11	0.08
7	273.4230317	-57.72231699	-9.93	0.04	-10.18	0.08	-12.00	0.02
8	273.4240561	-57.72152951	-8.93	0.09	-10.29	0.05	-12.24	0.09
9	273.4126981	-57.72621106	-12.88	0.05	-13.10	0.03	-13.35	0.03
10	273.4127251	-57.72525032	-11.08	0.09	-11.83	0.12	-11.87	0.10
11	273.4124913	-57.72636619	-11.88	0.02	-12.08	0.04	-12.71	0.05
12	273.4126885	-57.72499269	-12.73	0.05	-13.52	0.03	-13.37	0.02
13	273.4126222	-57.72421981	-10.61	0.05	-11.47	0.03	-11.90	0.10
14	273.4126044	-57.72447105	-10.59	0.06	-12.28	0.02	-12.28	0.07
15	273.4122004	-57.72543793	-11.09	0.13	-11.61	0.11	-11.99	0.09
16	273.4120619	-57.72591473	-12.36	0.02	-13.28	0.02	-12.76	0.04
17	273.4118376	-57.72547113	-11.04	0.15	-11.88	0.09	-12.41	0.06
18	273.4107751	-57.72651001	-11.29	0.05	-11.13	0.09	-13.45	0.05

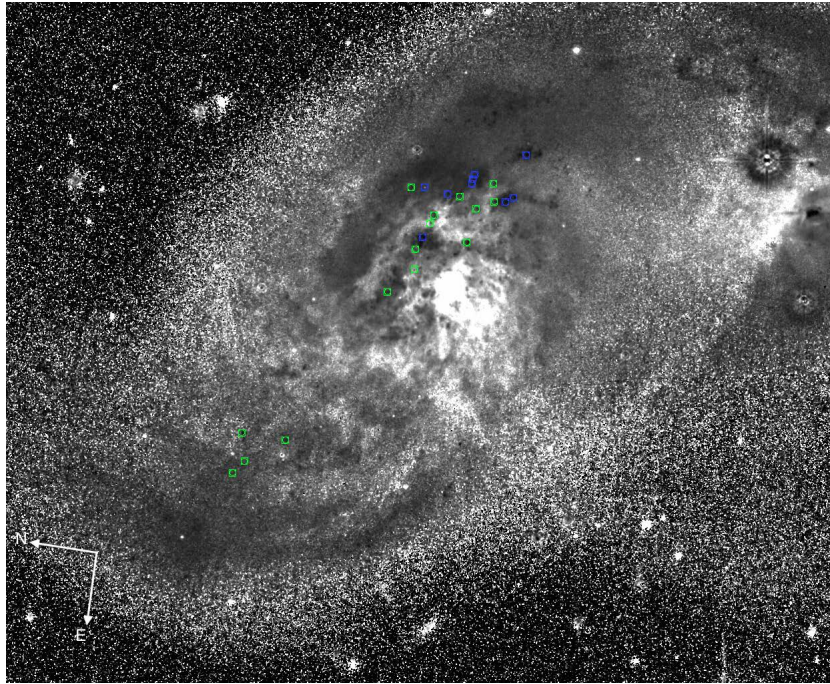


FIG. 45.— Inverted black and white B-I image of IC 4687N taken with HST ACS/WFC F814W and F435W. The bright emission corresponds to redder (i.e. dustier) regions of the galaxy. The blue centroids correspond to clusters found in relatively “dust-free” regions of these galaxies, whereas the green centroids correspond to clusters found in relatively dustier regions of the galaxy.

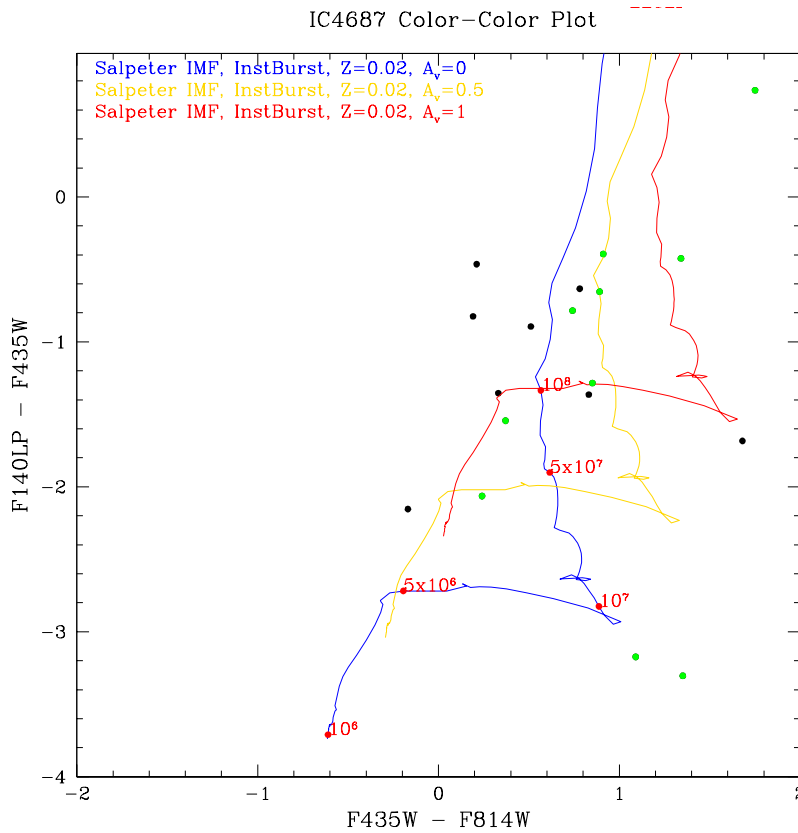


FIG. 46.— Color-Color plot of all star clusters identified in IC 4687N in F814W, F435W, and F140LP plotted against SSP models with various amount of visual extinction. The green points correspond to the clusters found in dustier regions of the galaxy in Figure 45

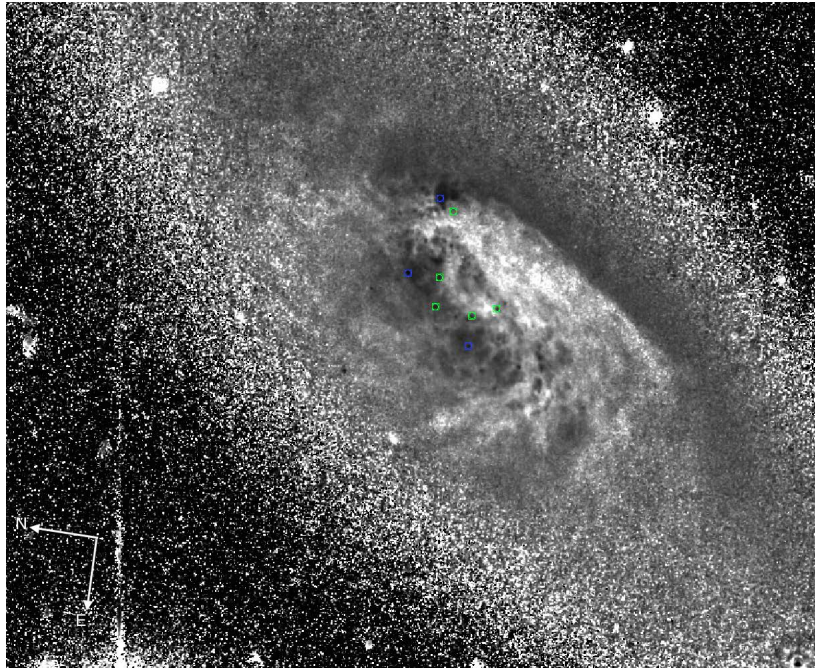


FIG. 47.— Inverted black and white B-I image of IC 4687S taken with HST ACS/WFC F814W and F435W. The bright emission corresponds to redder (i.e. dustier) regions of the galaxy. The blue centroids correspond to clusters found in relatively “dust-free” regions of these galaxies, whereas the green centroids correspond to clusters found in relatively dustier regions of the galaxy.

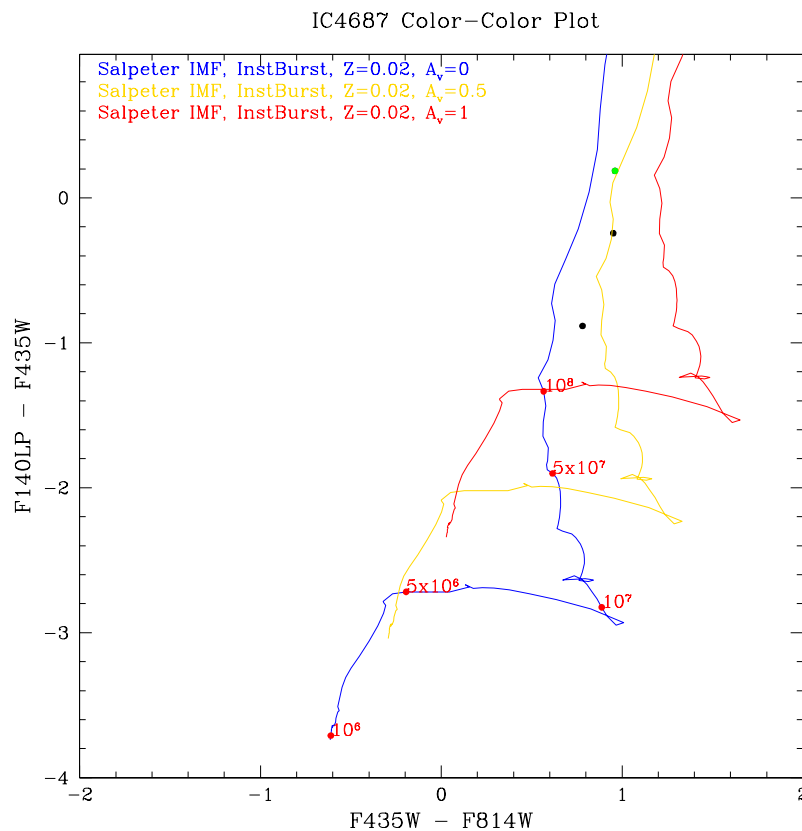


FIG. 48.— Color-Color plot of all star clusters identified in IC 4687S in F814W, F435W, and F140LP plotted against SSP models with various amount of visual extinction. The green points correspond to the clusters found in dustier regions of the galaxy in Figure 47

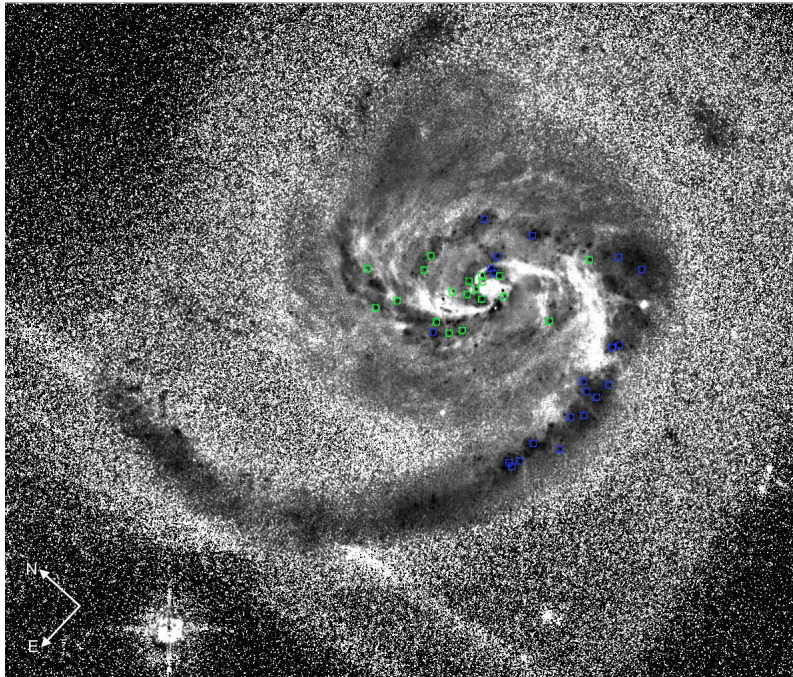


FIG. 49.— Inverted black and white B-I image of NGC 6786 taken with HST ACS/WFC F814W and F435W. The bright emission corresponds to redder (i.e. dustier) regions of the galaxy. The blue centroids correspond to clusters found in relatively “dust-free” regions of these galaxies, whereas the green centroids correspond to clusters found in relatively dustier regions of the galaxy.

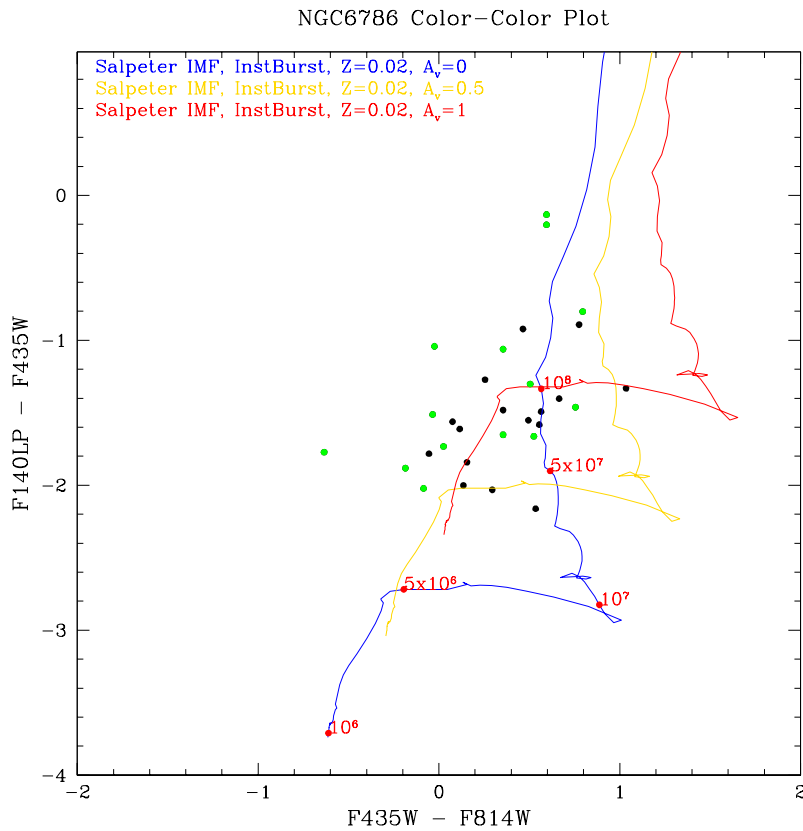


FIG. 50.— Color-Color plot of all star clusters identified in NGC 6786 in F814W, F435W, and F140LP plotted against SSP models with various amount of visual extinction. The green points correspond to the clusters found in dustier regions of the galaxy in Figure 49

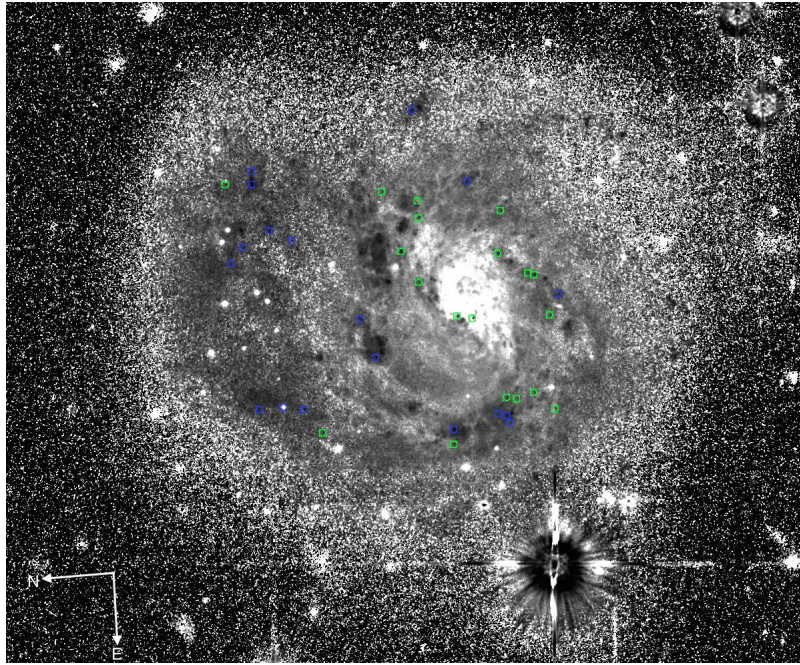


FIG. 51.— Inverted black and white B-I image of IRAS 20351+2521 taken with HST ACS/WFC F814W and F435W. The bright emission corresponds to redder (i.e. dustier) regions of the galaxy. The blue centroids correspond to clusters found in relatively “dust-free” regions of these galaxies, whereas the green centroids correspond to clusters found in relatively dustier regions of the galaxy.

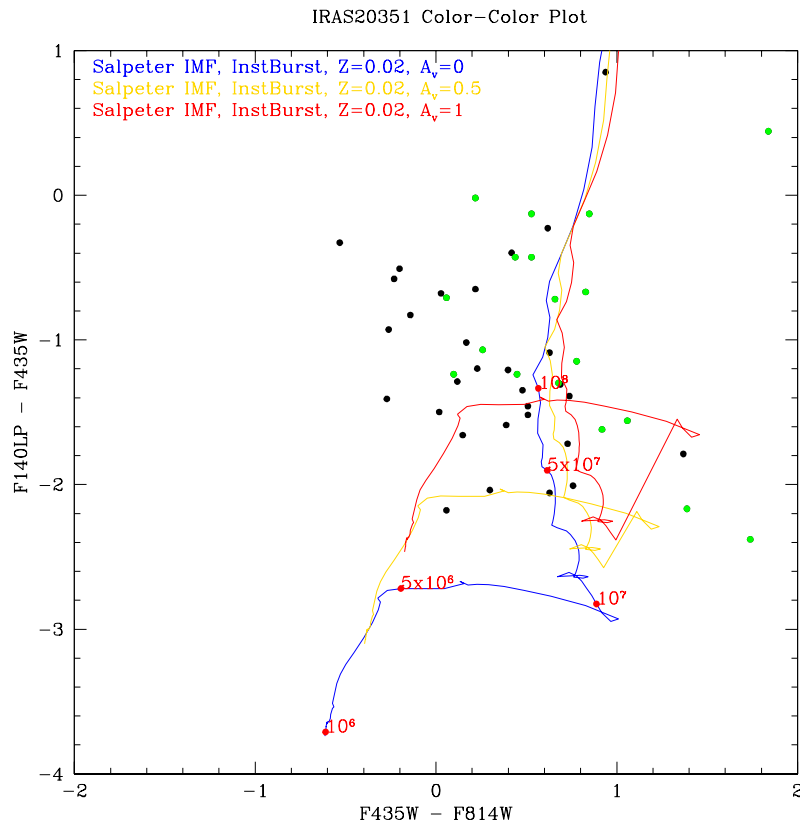


FIG. 52.— Color-Color plot of all star clusters identified in IRAS 20351+2521 in F814W, F435W, and F140LP plotted against SSP models with various amount of visual extinction. The green points correspond to the clusters found in dustier regions of the galaxy in Figure 51

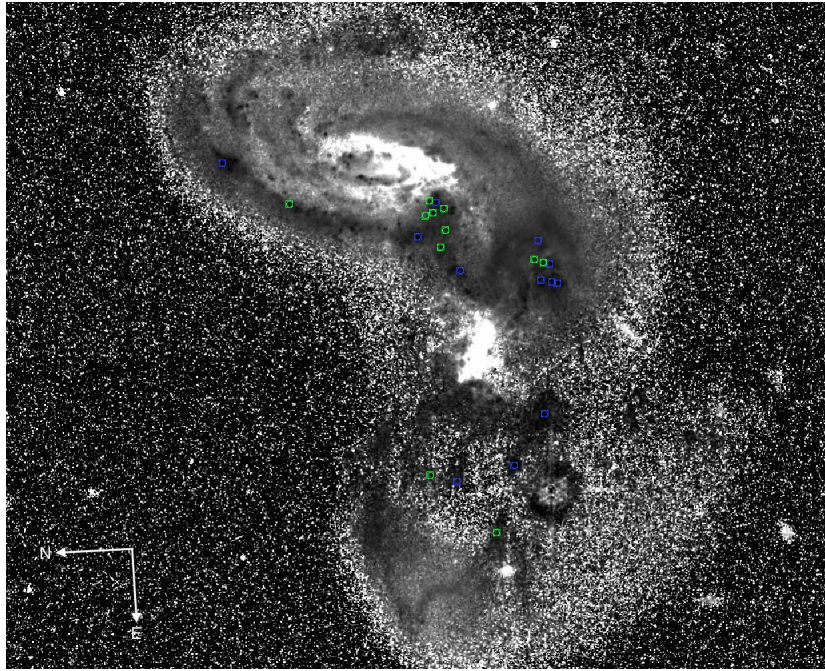


FIG. 53.— Inverted black and white B-I image of II Zw 096 taken with HST ACS/WFC F814W and F435W. The bright emission corresponds to redder (i.e. dustier) regions of the galaxy. The blue centroids correspond to clusters found in relatively “dust-free” regions of these galaxies, whereas the green centroids correspond to clusters found in relatively dustier regions of the galaxy.

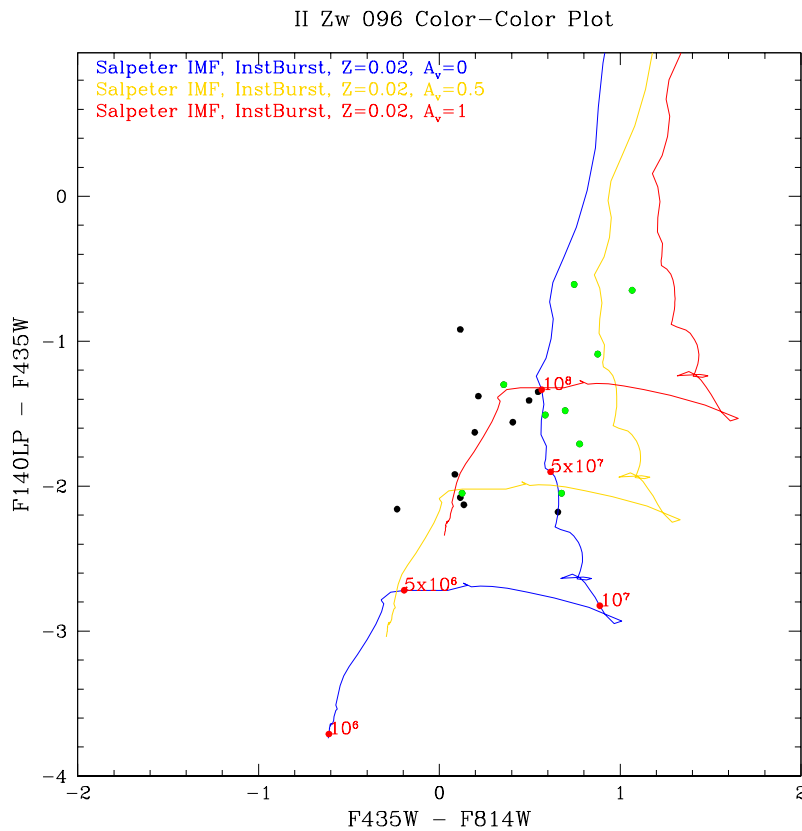


FIG. 54.— Color-Color plot of all star clusters identified in II Zw 096 in F814W, F435W, and F140LP plotted against SSP models with various amount of visual extinction. The green points correspond to the clusters found in dustier regions of the galaxy in Figure 53

TABLE 44
DERIVED PROPERTIES OF STAR CLUSTERS IN IC 4687N

ID	Log(Age)	σ_{Age}	Log(M/M_{\odot})	σ_M	A_V	σ_{A_V}
1	6.94	0.01	3.98	0.22	0.01	0.03
2	7.76	0.43	7.13	0.35	1.80	0.30
3	6.66	0.09	6.37	0.27	1.00	0.19
4	7.65	0.37	7.09	0.31	1.10	0.25
5	8.01	0.75	6.16	0.58	0.50	0.59
6	6.36	0.35	5.39	0.37	1.50	0.32
7	6.72	0.45	4.41	0.37	0.50	0.32
8	6.94	0.01	4.15	0.20	0.01	0.01
9	6.66	0.01	6.10	0.18	1.50	0.53
10	6.00	0.85	5.94	0.66	2.10	0.69
11	6.66	0.31	5.60	0.18	1.30	0.05
12	6.70	0.97	6.05	0.70	1.50	0.75
13	7.74	0.38	5.58	0.33	0.40	0.27
14	7.65	0.01	5.36	0.20	0.10	0.08
15	6.68	0.66	5.28	0.62	1.30	0.63
16	8.06	0.86	6.57	0.70	0.60	0.76
17	6.80	0.48	5.20	0.45	1.00	0.39
18	6.66	0.09	4.88	0.24	0.40	0.15

TABLE 45
OBSERVED PROPERTIES OF STAR CLUSTERS IN IC 4687S

ID	RA	Dec	M_B	σ_B	M_I	σ_I	M_{FUV}	σ_{FUV}
1	273.4156651	-57.7476378	-9.47	0.16	-11.63	0.09	-10.47	0.36
2	273.4174919	-57.74709814	-12.71	0.02	-13.50	0.01	-13.60	0.02
3	273.4181417	-57.74844252	-13.11	0.02	-14.08	0.04	-12.93	0.04
4	273.4184439	-57.74809628	-12.50	0.05	-13.27	0.07	-11.14	0.18
5	273.4192425	-57.74811065	-11.58	0.05	-12.54	0.03	-11.83	0.10

TABLE 46
DERIVED PROPERTIES OF STAR CLUSTERS IN IC 4687S

ID	Log(Age)	σ_{Age}	Log(M/M_{\odot})	σ_M	A_V	σ_{A_V}
1	6.94	0.11	5.16	0.37	1.50	0.28
2	6.72	0.34	5.94	0.32	1.30	0.26
3	8.41	0.66	6.94	0.66	0.30	0.70
4	8.66	0.03	6.75	0.19	0.01	0.05
5	6.40	0.76	6.19	0.73	2.40	0.79

this galaxy is 2.5 mags of visual extinction (Johansson & Bergvall 1988).

TABLE 47
OBSERVED PROPERTIES OF STAR CLUSTERS IN NGC 6786

ID	RA	Dec	M_B	σ_B	M_I	σ_I	M_{FUV}	σ_{FUV}
1	287.7197193	73.41100197	-10.99	0.02	-11.66	0.03	-12.39	0.05
2	287.719232	73.40994657	-12.43	0.02	-12.93	0.04	-13.98	0.03
3	287.7238745	73.41165138	-10.79	0.04	-11.30	0.04	-12.09	0.07
4	287.7178111	73.40815357	-9.46	0.06	-10.03	0.06	-10.95	0.22
5	287.7238495	73.41044623	-11.77	0.07	-12.37	0.14	-11.97	0.08
6	287.7234966	73.41051976	-13.43	0.02	-13.41	0.06	-14.47	0.02
7	287.7229265	73.41018561	-15.39	0.01	-15.31	0.01	-17.41	0.01
8	287.7227232	73.41040649	-15.05	0.01	-15.31	0.01	-16.32	0.01
9	287.7229402	73.41032417	-14.37	0.02	-14.51	0.03	-16.37	0.01
10	287.7267694	73.41270096	-9.77	0.18	-11.79	0.04	-10.19	0.11
11	287.7250088	73.41164334	-10.13	0.06	-10.10	0.11	-11.64	0.11
12	287.7242707	73.4107057	-12.76	0.03	-13.56	0.04	-13.56	0.02
13	287.7250077	73.41029358	-14.21	0.03	-13.58	0.10	-15.98	0.01
14	287.7251949	73.41061029	-12.67	0.06	-13.27	0.10	-12.80	0.04
15	287.7254972	73.41090859	-10.45	0.06	-10.27	0.20	-12.33	0.02
16	287.7241289	73.40990629	-12.92	0.02	-14.11	0.05	-11.81	0.09
17	287.7290544	73.4121962	-11.94	0.03	-12.30	0.03	-13.00	0.03
18	287.7242387	73.40883366	-10.24	0.04	-10.27	0.08	-11.97	0.08
19	287.7279844	73.41092482	-11.98	0.02	-12.74	0.03	-13.44	0.02
20	287.7277016	73.41036998	-12.38	0.02	-12.91	0.02	-14.04	0.01
21	287.7287715	73.41090241	-13.47	0.01	-13.63	0.01	-15.31	0.01
22	287.7283128	73.41059111	-11.42	0.03	-11.78	0.04	-13.07	0.03
23	287.7235043	73.40730799	-11.63	0.05	-12.67	0.04	-12.96	0.03
24	287.7270499	73.40763824	-11.77	0.01	-12.55	0.02	-12.66	0.04
25	287.7264275	73.40713593	-10.01	0.07	-10.54	0.10	-12.16	0.07
26	287.7276317	73.40724684	-11.46	0.04	-11.93	0.03	-12.38	0.06
27	287.727598	73.40748488	-12.61	0.01	-12.56	0.02	-14.39	0.01
28	287.7297973	73.40754253	-10.67	0.03	-11.23	0.03	-12.25	0.06
29	287.7327209	73.40798896	-13.58	0.01	-13.70	0.01	-15.19	0.01
30	287.7322458	73.40744712	-9.67	0.04	-9.97	0.07	-11.70	0.20
31	287.7343067	73.40807688	-11.58	0.02	-11.66	0.04	-13.14	0.03
32	287.7349114	73.40817718	-11.63	0.04	-11.99	0.05	-13.11	0.06

TABLE 48
DERIVED PROPERTIES OF STAR CLUSTERS IN NGC 6786

ID	Log(Age)	σ_{Age}	Log(M/M_\odot)	σ_M	A_V	σ_{A_V}
1	6.78	0.49	5.48	0.39	0.90	0.35
2	6.74	0.56	5.97	0.43	0.80	0.40
3	6.22	0.67	5.41	0.50	1.70	0.48
4	6.74	0.55	4.84	0.38	0.90	0.33
5	8.41	0.07	6.64	0.23	0.01	0.13
6	6.66	0.01	6.45	0.17	1.10	0.46
7	6.66	0.34	6.97	0.17	0.50	0.01
8	6.66	0.01	7.10	0.17	1.00	0.11
9	6.44	0.06	6.57	0.21	1.10	0.11
10	7.00	0.17	5.91	0.26	1.70	0.16
11	6.66	0.01	5.03	0.20	0.80	0.07
12	8.01	0.08	6.99	0.22	0.40	0.13
13	6.66	0.04	6.50	0.18	0.50	0.05
14	8.41	0.04	7.00	0.20	0.01	0.07
15	6.66	0.04	5.05	0.23	0.60	0.13
16	8.51	0.05	7.44	0.23	0.50	0.15
17	6.66	0.57	5.86	0.43	1.20	0.40
18	6.66	0.03	5.02	0.21	0.70	0.10
19	7.72	0.44	6.47	0.35	0.30	0.30
20	7.86	0.55	6.55	0.40	0.01	0.36
21	6.48	0.04	6.43	0.22	1.10	0.12
22	5.10	0.04	5.55	0.19	1.50	0.07
23	7.63	0.24	6.37	0.25	0.50	0.16
24	6.72	0.05	5.84	0.18	1.30	0.06
25	6.84	0.35	4.91	0.27	0.40	0.19
26	6.66	0.05	5.67	0.18	1.30	0.02
27	6.66	0.35	5.97	0.18	0.70	0.03
28	6.74	0.57	5.27	0.43	0.80	0.40
29	6.66	0.29	6.41	0.17	0.80	0.04
30	6.72	0.05	4.70	0.20	0.50	0.09
31	6.66	0.58	5.61	0.18	0.80	0.04
32	6.40	0.05	5.67	0.20	1.50	0.08

TABLE 49
OBSERVED PROPERTIES OF STAR CLUSTERS IN IRAS 20351+2521

ID	RA	Dec	M_B	σ_B	M_I	σ_I	M_{FUV}	σ_{FUV}
1	309.3189111	25.52810092	-11.77	0.04	-11.99	0.06	-12.96	0.25
2	309.3201669	25.53148902	-12.10	0.03	-12.78	0.03	-13.40	0.14
3	309.3204655	25.53148786	-14.20	0.01	-14.34	0.02	-15.85	0.04
4	309.3207482	25.52879944	-11.57	0.05	-12.24	0.05	-12.86	0.05
5	309.3205846	25.52701311	-12.18	0.08	-11.64	0.16	-12.50	0.26
6	309.3209895	25.52805392	-12.80	0.04	-14.63	0.01	-12.35	0.24
7	309.3213802	25.52804452	-12.92	0.03	-13.44	0.03	-13.04	0.17
8	309.3212834	25.52633971	-11.39	0.06	-12.12	0.06	-12.77	0.22
9	309.3215513	25.53117662	-11.92	0.07	-11.68	0.12	-12.49	0.16
10	309.3227499	25.52581676	-12.05	0.06	-12.70	0.07	-12.76	0.16
11	309.3227896	25.52569385	-12.91	0.02	-12.96	0.05	-13.61	0.07
12	309.3232605	25.52520015	-12.72	0.05	-13.34	0.06	-13.80	0.12
13	309.3237357	25.52539922	-11.60	0.05	-12.42	0.03	-12.26	0.22
14	309.3236793	25.52933194	-11.99	0.06	-12.00	0.07	-13.48	0.12
15	309.3256351	25.52614986	-11.60	0.08	-12.04	0.10	-12.83	0.04
16	309.3255973	25.526354	-12.15	0.05	-12.24	0.08	-13.38	0.06
17	309.3256314	25.53101137	-11.60	0.05	-14.92	0.01	-12.71	0.01
18	309.3256579	25.53150391	-11.02	0.08	-11.77	0.06	-13.02	0.21
19	309.3259664	25.52654554	-11.17	0.15	-12.53	0.06	-12.95	0.27
20	309.3261938	25.52631453	-13.23	0.02	-13.84	0.02	-13.45	0.16
21	309.3262881	25.52747562	-13.98	0.02	-14.03	0.02	-16.15	0.01
22	309.3262506	25.53020748	-11.03	0.05	-11.65	0.05	-13.08	0.03

TABLE 50
DERIVED PROPERTIES OF STAR CLUSTERS IN IRAS
20351+2521

ID	Log(Age)	σ_{Age}	Log(M/M_\odot)	σ_M	A_V	σ_{A_V}
1	6.54	0.33	5.69	0.16	1.50	0.02
2	6.74	0.19	5.65	0.16	1.10	0.31
3	6.54	0.32	6.50	0.15	1.20	0.23
4	7.76	0.42	5.92	0.16	0.40	0.20
5	6.52	0.40	6.07	0.18	1.90	0.45
6	6.78	0.05	6.57	0.16	2.30	0.59
7	8.51	0.11	6.72	0.16	0.01	0.53
8	7.70	0.12	5.81	0.17	0.40	0.16
9	6.52	0.23	5.91	0.17	1.80	0.46
10	8.36	0.53	6.26	0.17	0.01	0.19
11	6.52	0.08	6.31	0.16	1.80	0.05
12	6.64	0.37	6.19	0.16	1.60	0.54
13	7.96	0.12	6.13	0.16	0.60	0.08
14	6.52	0.18	5.67	0.17	1.30	0.12
15	6.52	0.29	5.68	0.18	1.60	0.24
16	6.52	0.32	5.84	0.16	1.50	0.24
17	8.11	0.39	6.22	0.16	0.60	0.23
18	6.94	0.52	5.09	0.18	0.50	0.59
19	7.65	0.53	5.53	0.22	0.10	0.36
20	6.52	0.07	6.65	0.16	2.20	0.41
21	6.44	0.19	6.49	0.16	1.10	0.19
22	7.36	0.24	5.39	0.16	0.30	0.58

TABLE 51
OBSERVED PROPERTIES OF STAR CLUSTERS IN II ZW 096

ID	RA	Dec	M_B	σ_B	M_I	σ_I	M_{FUV}	σ_{FUV}
1	314.347937	17.13209914	-14.40	0.02	-14.52	0.01	-16.48	0.01
2	314.3488605	17.12855532	-13.82	0.03	-14.60	0.03	-15.53	0.05
3	314.3490196	17.12831079	-13.91	0.02	-14.50	0.05	-15.42	0.02
4	314.3489006	17.12844657	-14.02	0.05	-14.14	0.07	-14.94	0.12
5	314.3487591	17.13097999	-13.81	0.02	-13.94	0.02	-15.86	0.01
6	314.3491325	17.12863715	-13.77	0.02	-14.84	0.01	-14.42	0.03
7	314.349413	17.12830611	-13.18	0.02	-14.06	0.02	-14.27	0.04
8	314.3494999	17.12879568	-14.29	0.01	-14.38	0.02	-16.21	0.01
9	314.3497151	17.12841414	-16.14	0.01	-16.84	0.01	-17.62	0.01
10	314.3501466	17.12654531	-17.92	0.01	-18.33	0.01	-19.48	0.01
11	314.3501115	17.12664894	-15.51	0.05	-16.26	0.05	-16.12	0.03
12	314.3500502	17.12680274	-13.52	0.11	-13.88	0.19	-14.82	0.07
13	314.3501617	17.12810109	-14.29	0.02	-14.84	0.02	-15.64	0.02
14	314.3504248	17.12671799	-14.41	0.10	-14.91	0.09	-15.82	0.05
15	314.3504765	17.12652561	-16.42	0.01	-16.64	0.02	-17.80	0.02
16	314.350505	17.12642631	-16.31	0.01	-16.51	0.02	-17.94	0.01
17	314.352852	17.12679784	-14.29	0.01	-14.06	0.03	-16.45	0.01
18	314.353755	17.1273767	-13.74	0.01	-13.88	0.02	-15.87	0.01
19	314.3538332	17.12884574	-13.71	0.01	-14.39	0.01	-15.76	0.01
20	314.3539789	17.12839369	-12.26	0.02	-12.92	0.02	-14.44	0.03

TABLE 52
DERIVED PROPERTIES OF STAR CLUSTERS IN II ZW 096

ID	Log(Age)	σ_{Age}	Log(M/M_\odot)	σ_M	A_V	σ_{A_V}
1	6.40	0.08	6.76	0.22	1.20	0.12
2	7.40	0.25	6.64	0.24	0.50	0.16
3	6.74	0.45	6.32	0.39	1.00	0.35
4	6.52	0.53	6.70	0.52	1.70	0.50
5	6.42	0.12	6.52	0.24	1.20	0.16
6	7.63	0.27	7.04	0.26	1.00	0.19
7	7.63	0.26	6.64	0.26	0.70	0.18
8	6.52	0.02	6.49	0.18	1.10	0.06
9	7.65	0.01	7.68	0.17	0.40	0.13
10	5.70	0.62	8.60	0.44	1.60	0.41
11	6.54	0.85	7.45	0.81	2.00	0.93
12	6.54	0.55	6.39	0.53	1.50	0.52
13	6.72	0.61	6.60	0.54	1.20	0.54
14	6.58	0.62	6.73	0.55	1.40	0.55
15	6.54	0.01	7.50	0.17	1.40	0.03
16	6.52	0.01	7.40	0.18	1.30	0.04
17	6.54	0.01	6.33	0.18	0.80	0.05
18	5.70	0.41	6.71	0.27	1.20	0.20
19	6.78	0.07	5.98	0.17	0.50	0.02
20	6.96	0.15	5.57	0.18	0.40	0.06

TABLE 53
OBSERVED PROPERTIES OF STAR CLUSTERS IN ESO 148-IG002

ID	RA	Dec	M_B	σ_B	M_I	σ_I	M_{FUV}	σ_{FUV}
1	348.9465405	-59.05411541	-14.15	0.01	-14.90	0.01	-14.43	0.03
2	348.9468576	-59.0539657	-13.60	0.02	-14.73	0.02	-13.26	0.10
3	348.9462256	-59.05361789	-12.73	0.03	-13.39	0.04	-12.63	0.18
4	348.9469037	-59.05365887	-11.95	0.09	-13.24	0.08	-12.87	0.14
5	348.9454074	-59.05331294	-13.54	0.15	-14.19	0.09	-14.48	0.06
6	348.9468404	-59.05307144	-14.27	0.02	-15.05	0.01	-14.84	0.02
7	348.9456965	-59.05497655	-14.45	0.04	-15.22	0.03	-14.50	0.06

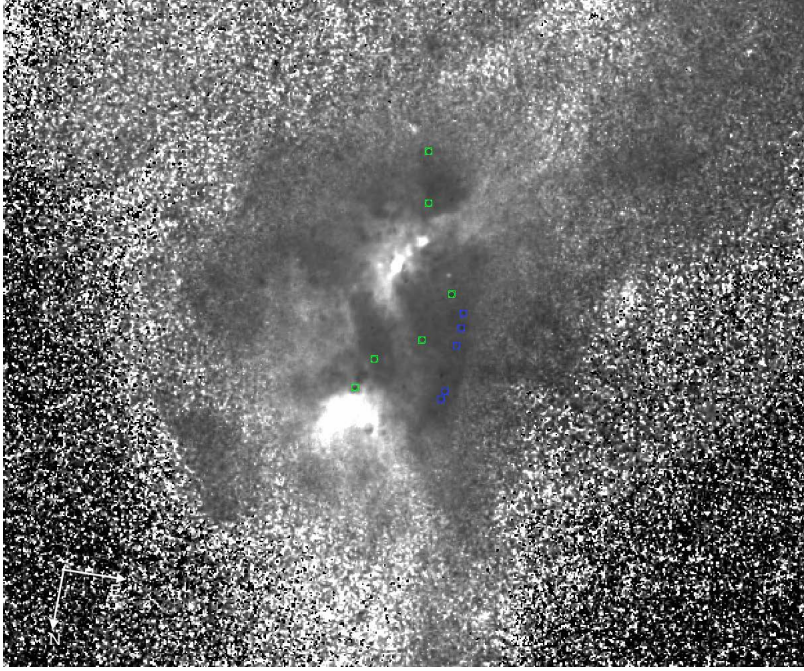


FIG. 55.— Inverted black and white B-I image of ESO 148-IG002 taken with HST ACS/WFC F814W and F435W. The bright emission corresponds to redder (i.e. dustier) regions of the galaxy. The blue centroids correspond to clusters found in relatively “dust-free” regions of these galaxies, whereas the green centroids correspond to clusters found in relatively dustier regions of the galaxy.

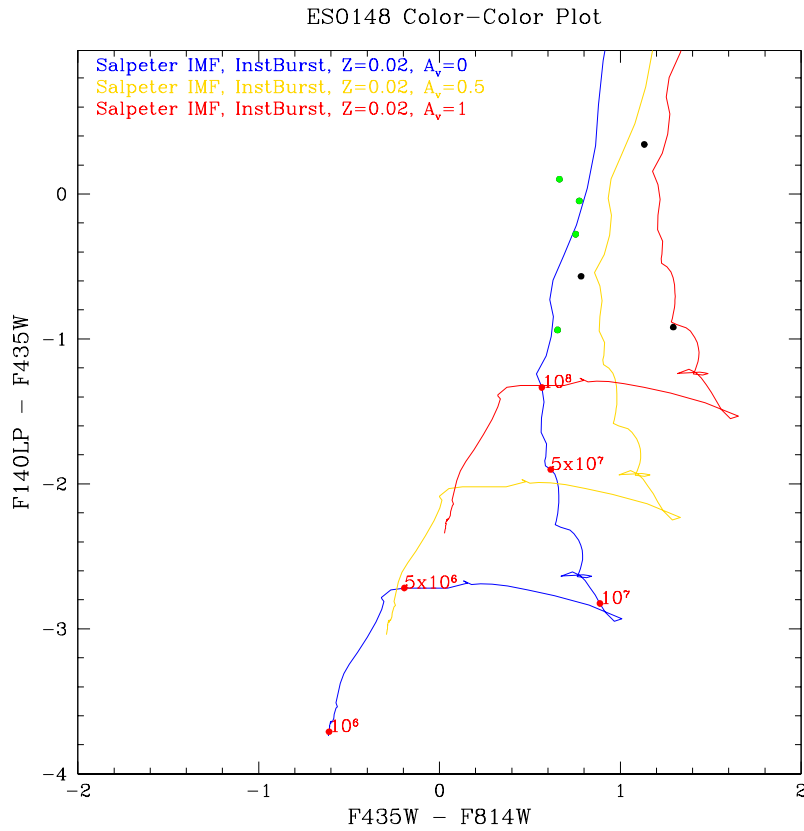


FIG. 56.— Color-Color plot of all star clusters identified in ESO 148-IG002 in F814W, F435W, and F140LP plotted against SSP models with various amount of visual extinction. The green points correspond to the clusters found in dustier regions of the galaxy in Figure 55

TABLE 54
DERIVED PROPERTIES OF STAR CLUSTERS IN ESO 148-IG002

ID	Log(Age)	σ_{Age}	Log(M/M_{\odot})	σ_M	A_V	σ_{A_V}
1	8.46	0.03	7.17	0.16	0.01	0.78
2	8.41	0.40	7.23	0.45	0.60	0.43
3	8.61	0.06	6.73	0.17	0.01	0.02
4	7.65	0.25	6.21	0.24	0.80	0.14
5	8.26	0.79	6.80	0.69	0.01	0.73
6	6.48	0.90	7.13	0.84	2.20	0.97
7	8.56	0.04	7.38	0.17	0.01	0.04

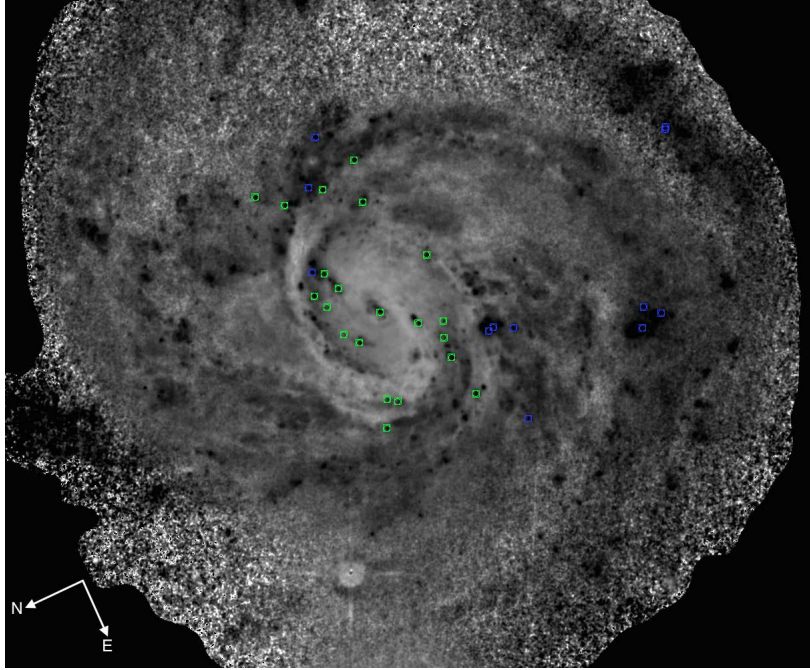


FIG. 57.— Inverted black and white B-I image of NGC 7674 taken with HST ACS/WFC F814W and F435W. The bright emission corresponds to redder (i.e. dustier) regions of the galaxy. The blue centroids correspond to clusters found in relatively “dust-free” regions of these galaxies, whereas the green centroids correspond to clusters found in relatively dustier regions of the galaxy.

TABLE 55
OBSERVED PROPERTIES OF STAR CLUSTERS IN NGC 7674

ID	RA	Dec	M_B	σ_B	M_I	σ_I	M_{FUV}	σ_{FUV}
1	351.9831239	8.778349264	-12.20	0.02	-12.57	0.03	-14.06	0.02
2	351.9849596	8.772096618	-11.55	0.02	-11.73	0.04	-13.17	0.05
3	351.9850026	8.772116709	-11.44	0.02	-11.76	0.03	-12.79	0.08
4	351.9832985	8.779441129	-10.77	0.11	-11.11	0.13	-13.04	0.06
5	351.9830552	8.780545473	-10.91	0.03	-11.08	0.05	-12.85	0.04
6	351.9840117	8.778513551	-12.29	0.04	-12.74	0.03	-13.63	0.04
7	351.9849762	8.780046055	-12.87	0.02	-12.92	0.03	-15.07	0.02
8	351.9855017	8.779670342	-12.42	0.04	-12.61	0.09	-13.89	0.06
9	351.9862949	8.779049017	-17.60	0.01	-18.76	0.01	-19.06	0.01
10	351.9882912	8.773938539	-12.62	0.01	-13.32	0.01	-14.50	0.02
11	351.9885463	8.773640234	-11.47	0.03	-12.12	0.05	-13.84	0.03
12	351.9857724	8.780029971	-11.03	0.05	-10.37	0.20	-12.96	0.07
13	351.9869669	8.777906039	-11.45	0.04	-11.50	0.06	-12.83	0.05
14	351.9868119	8.778402264	-13.02	0.01	-13.05	0.03	-14.91	0.01
15	351.9875291	8.777102907	-13.70	0.03	-13.66	0.03	-15.37	0.02
16	351.9886887	8.774122684	-11.76	0.03	-11.76	0.06	-14.04	0.05
17	351.9874886	8.7769875	-11.39	0.19	-12.26	0.16	-14.14	0.04
18	351.9864376	8.77992672	-11.09	0.04	-11.46	0.07	-13.01	0.06
19	351.9873013	8.778022066	-10.96	0.06	-11.33	0.13	-12.90	0.07
20	351.9867238	8.779687958	-12.50	0.03	-12.67	0.04	-14.62	0.01
21	351.9877438	8.778029429	-12.90	0.02	-13.24	0.04	-14.16	0.02
22	351.988047	8.779603842	-10.36	0.13	-11.65	0.09	-13.07	0.03
23	351.9895457	8.777038636	-10.67	0.05	-10.77	0.09	-12.88	0.07
24	351.9886045	8.779833873	-12.05	0.03	-12.33	0.05	-13.70	0.03
25	351.9823723	8.778916581	-11.27	0.03	-11.67	0.04	-12.86	0.07

NGC 7674

NGC 7674 an early-stage merger with a face-on spiral galaxy and companions to the northeast and southeast. Star clusters are visible along the prominent spiral arms throughout the galaxy. The maximum A_V adopted for this galaxy is 2.0 mags of visual extinction (Momjian et al. 2003).

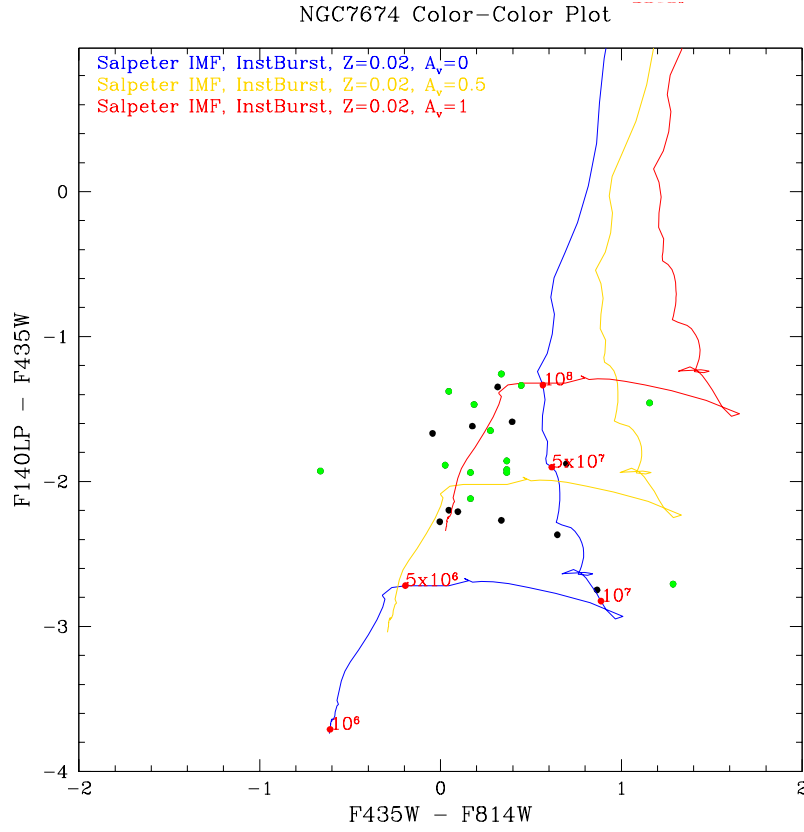


FIG. 58.— Color-Color plot of all star clusters identified in NGC 7674 in F814W, F435W, and F140LP plotted against SSP models with various amount of visual extinction. The green points correspond to the clusters found in dustier regions of the galaxy in Figure 57

TABLE 56
DERIVED PROPERTIES OF STAR CLUSTERS IN NGC 7674

ID	Log(Age)	σ_{Age}	Log(M/M_{\odot})	σ_M	A_V	σ_{A_V}
1	6.74	0.03	5.48	0.21	0.70	0.11
2	6.52	0.02	5.50	0.19	1.30	0.07
3	6.52	0.03	5.56	0.19	1.50	0.08
4	6.72	0.28	4.87	0.27	0.60	0.17
5	6.52	0.08	5.14	0.22	1.10	0.13
6	6.44	0.10	6.14	0.24	1.70	0.16
7	6.42	0.10	6.09	0.22	1.10	0.14
8	6.52	0.05	5.90	0.20	1.40	0.09
9	6.80	0.03	7.78	0.17	0.90	0.03
10	7.00	0.07	5.97	0.17	0.70	0.04
11	7.00	0.10	5.46	0.17	0.60	1.12
12	6.52	0.01	5.08	0.20	0.90	0.09
13	6.52	0.01	5.51	0.18	1.40	0.04
14	6.52	0.01	5.98	0.17	1.10	0.03
15	6.52	0.01	6.31	0.17	1.20	0.03
16	6.50	0.08	5.39	0.22	0.90	0.13
17	7.00	0.43	5.43	0.27	0.60	0.06
18	6.74	0.18	5.04	0.27	0.70	0.20
19	6.74	0.19	4.98	0.29	0.70	0.22
20	6.58	0.27	5.70	0.27	0.90	0.20
21	6.54	0.01	6.14	0.18	1.50	0.05
22	6.82	0.10	4.76	0.22	0.60	1.12
23	6.68	0.11	4.90	0.24	0.70	0.16
24	6.52	0.28	5.70	0.24	1.30	0.16
25	6.66	0.30	5.41	0.30	1.20	0.23